

RICE UNIVERSITY

**Compact Support Wavelet Representations for  
Solution of Quantum and Electromagnetic Equations:  
Eigenvalues and Dynamics**

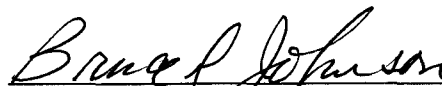
by

**Ramiro Acevedo Jr.**

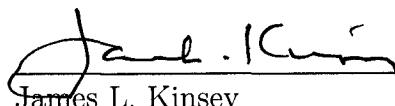
A THESIS SUBMITTED  
IN PARTIAL FULFILLMENT OF THE  
REQUIREMENTS FOR THE DEGREE

**Doctor of Philosophy**

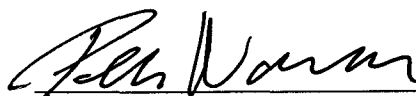
APPROVED, THESIS COMMITTEE:



Bruce R. Johnson, Chair  
Distinguished Faculty Fellow  
in Chemistry



James L. Kinsey  
D. R. Bullard-Welch Foundation  
Professor Emeritus of Science



Peter Nordlander  
Professor of Physics and Astronomy

HOUSTON, TEXAS  
MAY 2010

UMI Number: 3421326

All rights reserved

INFORMATION TO ALL USERS

The quality of this reproduction is dependent upon the quality of the copy submitted.

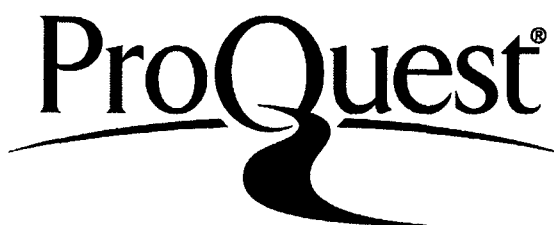
In the unlikely event that the author did not send a complete manuscript and there are missing pages, these will be noted. Also, if material had to be removed, a note will indicate the deletion.



UMI 3421326

Copyright 2010 by ProQuest LLC.

All rights reserved. This edition of the work is protected against unauthorized copying under Title 17, United States Code.



ProQuest LLC  
789 East Eisenhower Parkway  
P.O. Box 1346  
Ann Arbor, MI 48106-1346

## **Abstract**

Compact Support Wavelet Representations for Solution of Quantum and  
Electromagnetic Equations: Eigenvalues and Dynamics

by

Ramiro Acevedo Jr.

Wavelet-based algorithms are developed for solution of quantum and electromagnetic differential equations. Wavelets offer orthonormal localized bases with built-in multiscale properties for the representation of functions, differential operators, and multiplicative operators. The work described here is part of a series of tools for use in the ultimate goal of general, efficient, accurate and automated wavelet-based algorithms for solution of differential equations.

The most recent work, and the focus here, is the elimination of operator matrices in wavelet bases. For molecular quantum eigenvalue and dynamics calculations in multiple dimensions, it is the coupled potential energy matrices that generally dominate storage requirements. A Coefficient Product Approximation (CPA) for the potential operator and wave function wavelet expansions dispenses with the matrix, reducing storage and coding complexity. New developments are required, however. It is determined that the CPA is most accurate for specific choices of wavelet families, and these are given here. They have relatively low approximation order (number of vanishing wavelet function moments), which would ordinarily be thought to compromise both wavelet reconstruction and differentiation accuracy. Higher-order convolutional coefficient filters are determined that overcome both apparent problems. The result

is a practical wavelet method where the effect of applying the Hamiltonian matrix to a coefficient vector can be calculated accurately without constructing the matrix.

The long-familiar Lanczos propagation algorithm, wherein one constructs and diagonalizes a symmetric tridiagonal matrix, uses both eigenvalues and eigenvectors. We show here that time-reversal-invariance for Hermitian Hamiltonians allows a new algorithm that avoids the usual need to keep a number Lanczos vectors around. The resulting Conjugate Symmetric Lanczos (CSL) method, which will apply for wavelets or other choices of basis or grid discretization, is simultaneously low-operation-count and low-storage. A modified CSL algorithm is used for solution of Maxwell's time-domain equations in Hamiltonian form for non-lossy media. The matrix-free algorithm is expected to complement previous work and to decrease both storage and computational overhead. It is expected that near-field electromagnetic solutions around nanoparticles will benefit from these wavelet-based tools. Such systems are of importance in plasmon-enhanced spectroscopies.

## Acknowledgments

This work could not have been completed without the guidance and support of my advisor Dr. Bruce R. Johnson. I am grateful for his assistance. He is not only a great scientist but also a genuinely caring person. I sincerely thank the rest of my committee Dr. James L. Kinsey and Dr. Peter Nordlander. They are scientists I admire and respect.

My academic growth was influenced by a number of other people. My path was significantly altered through interactions with Dr. Gail E. Marlow and Susan Allen. My scientific interests were further influenced by Dr. Eric R. Bittner and Dr. Haixiang Wang. It was a pleasure to work with Dr. Richard Lombardini. He is a good teacher and scientist. I will never forget Yvonne Kambourelis. She took special care of me and all of her students in the Applied Physics Program.

I also thank my extended family and friends. They were always on my mind during the completion of this thesis. I could always rely on them to make the ride enjoyable and to be there if I needed them. My parents, Ramiro Sr. and Mary, gave selfless love, caring and guidance. They always pushed me to reach my goals. This is for the two of you. To my brother Richard, treat people well and remember that anything is possible. I want to especially thank my wife Azita. She is my sunshine.

# Contents

Abstract . . . . .	ii
Acknowledgments . . . . .	iv
List of Figures . . . . .	vii
List of Tables . . . . .	viii
<b>1 Introduction</b>	<b>1</b>
<b>I Wavelet Representations in QM and Electromagnetics</b>	<b>9</b>
<b>2 Compact Support Wavelets</b>	<b>10</b>
2.1 Scaling and Wavelet Representation . . . . .	10
2.2 Multiresolution Analysis and the Two-Scale Equations . . . . .	18
2.2.1 Wavelet Transform and Pyramid Algorithm . . . . .	23
2.2.2 Scaling Function Expansion Coefficient Refinement . . . . .	24
2.3 Daubechies Scaling Function Coefficients . . . . .	25
2.4 Scaling Function Moments . . . . .	30
2.5 Generalized Coiflet Scaling Function Coefficients . . . . .	31
2.6 Evaluation of Scaling Function Expansion Coefficients . . . . .	35
2.6.1 Single-Point Projection Integral Evaluation . . . . .	35
2.6.2 Multi-Point Projection Integral Evaluation . . . . .	37
2.7 Scaling Function Matrix Elements . . . . .	39
2.8 Difficulties with the Matrix Representation . . . . .	40
<b>3 Matrix-Free Application of Hamiltonian Operators in Wavelet Bases</b>	<b>43</b>
3.1 Coefficient Product Approximation for Potential Operators . . . . .	47
3.2 Optimized Max- $N$ Generalized Coiflets . . . . .	50
3.2.1 Coefficient Product Approximation Test . . . . .	54
3.3 Finite-Difference Derivatives for Kinetic Operators . . . . .	57
3.4 Regular and Higher-Order Filter Reconstruction . . . . .	61
3.5 Summary . . . . .	65
<b>4 TISE: Eigenvalues of a Matrix-Free Hamiltonian</b>	<b>66</b>
4.1 Eigenvalues with the Lanczos Algorithm . . . . .	67
4.2 Displaced Harmonic Oscillator . . . . .	69
4.3 Anharmonic Morse Potential . . . . .	70
4.3.1 Implicit Restarting with the Lanczos Algorithm . . . . .	72
4.3.2 Implicit Restarting Comparisons . . . . .	73
4.4 2D Proton Transfer Model Potential . . . . .	75

<b>5</b>	<b>TDSE: Evolution Equations</b>	<b>80</b>
5.1	Formal Solution for Time-Independent Hamiltonian . . . . .	81
5.2	Quantum Propagation: Evolution by CSL . . . . .	81
5.2.1	CSL from the Lanczos Basis . . . . .	84
5.3	Quantum Propagation: Evolution by CSL, Chebyshev, and SIL Methods	89
5.3.1	Displaced Harmonic Oscillator . . . . .	91
5.3.2	Morse Oscillator . . . . .	95
5.4	Electrodynamics . . . . .	96
5.4.1	Vacuum Propagation . . . . .	97
5.4.2	Propagation in Drude Materials . . . . .	100
5.5	Summary . . . . .	108
 <b>II</b>		
	<b>SEROA: Surface-Enhanced Raman Optical Activity</b>	<b>110</b>
<b>6</b>	<b>SEROA</b>	<b>112</b>
6.1	Introduction . . . . .	112
6.2	Ordinary and Surface-Enhanced Raman Optical Activity . . . . .	114
6.2.1	Ordinary ROA . . . . .	114
6.2.2	Surface-Enhanced ROA . . . . .	118
6.3	Mie Theory for EM Scattering Problems: Plane Wave Scattering . . .	121
6.4	Multipole Field Scattering . . . . .	125
6.4.1	Field Expansions from the Dyadic Green Tensor . . . . .	125
6.4.2	Sum Reduction by Analytic Evaluation of $\sigma$ and $m$ Sums . . .	129
6.5	Polarizations in SEROA . . . . .	132
6.5.1	Polarization-Specific Intensity Formulas . . . . .	132
6.5.2	Selectivity in ICP and SCP . . . . .	136
6.5.3	Selectivity in DCP . . . . .	138
6.6	Application to a Chiral Molecule Model . . . . .	141
6.7	Summary . . . . .	152
 <b>A</b>		
	<b>OMGC Scaling Wavelet Coefficients</b>	<b>156</b>
 <b>Bibliography</b>		<b>161</b>

## List of Figures

2.1	Scaled and translated wavelets $\psi_{jk}$ . . . . .	11
2.2	Scaled and translated scaling functions $\phi_{jk}$ . . . . .	13
2.3	Wavelet representation of an example function . . . . .	17
2.4	Pyramid algorithm . . . . .	23
2.5	Daubechies scaling and wavelet functions . . . . .	26
2.6	Daubechies coiflet scaling and wavelet functions . . . . .	33
2.7	Representative storage requirements for 3D direct product bases . . .	41
3.1	OMGC scaling and wavelet functions for lengths $L = 6-12$ . . . . .	54
3.2	OMGC scaling and wavelet functions for lengths $L = 14-16$ . . . . .	55
3.3	OMGC scaling and wavelet functions for lengths $L = 18-20$ . . . . .	56
3.4	Morse potential applied to Gaussian function. . . . .	56
3.5	CPA projection errors for Gaussian function/Morse potential product	57
3.6	Second derivative filter errors for Gaussian function . . . . .	60
3.7	Traditional and filter reconstruction errors for Morse-Gaussian function	64
4.1	Analytical Lanczos functions/vectors for Morse potential . . . . .	71
4.2	Sato and Iwata $H^+$ transfer PES contours and basis selection . . . . .	78
5.1	Projection coefficient errors for displaced HO propagated one time step	93
5.2	Projection coefficient errors for multiple-time-step displaced HO . . .	94
5.3	Projection coefficient errors for multiple-time-step Morse oscillator . .	96
5.4	Logarithm of coefficient magnitudes, $\log_{10}  a_n $ , for a single time step .	100
5.5	Coefficient errors for free propagation of an electromagnetic pulse . .	101
5.6	Gold-vacuum interface plot of $\text{Re}(E_x(z, t))$ . . . . .	106
5.7	Maximum errors in vacuum-gold pulse propagation with modified-CSL	107
6.1	Depiction of incident/outgoing circularly polarized SEROA . . . . .	113
6.2	ROA/SEROA polarization schemes . . . . .	116
6.3	Schematic of our SEROA model . . . . .	119
6.4	Enhancement factors for incident fields absorbed by nanoshell . . . .	124
6.5	Enantiomers of $H_2S_2$ . . . . .	142
6.6	DCP $\alpha\alpha$ total scattering intensity factors for Ag nanoshell . . . . .	146
6.7	DCP $\alpha G$ scattering intensity components for Ag nanoshell . . . . .	147
6.8	DCP CIDs for Ag nanoshell . . . . .	148
6.9	DCP $\alpha\alpha$ total scattering intensity factors for Au nanoshell . . . . .	149
6.10	DCP $\alpha G$ scattering intensity components for Au nanoshell . . . . .	150
6.11	DCP CIDs for Au nanoshell . . . . .	151



# List of Tables

2.1	Daubechies scaling function characteristics . . . . .	29
2.2	Coiflet scaling function characteristics . . . . .	34
3.1	Support length, $M$ , and $N$ relations for several compact support families	51
3.2	OMGC scaling function characteristics . . . . .	53
4.1	Lowest eigenvalue for harmonic oscillator with the Lanczos algorithm	69
4.2	Morse potential eigenvalues with the implicitly restarted Lanczos method	74
4.3	Eigenvalues of the H-atom transfer model of Sato and Iwata . . . . .	76
6.1	Components of the $\hat{\mathbf{R}}_t^{(E1)}$ tensor operator in spherical coordinates . .	131
6.2	Components of the $\hat{\mathbf{R}}_t^{(M1)}$ tensor operator in spherical coordinates . .	131
6.3	Intensity factors for DCP backscattering with model $\text{H}_2\text{S}_2$ . . . . .	145
A.1	OMGC scaling function coefficients for $L = 6, 8$ , and $10$ . . . . .	156
A.2	OMGC scaling function coefficients for $L = 12$ and $14$ . . . . .	157
A.3	OMGC scaling function coefficients for $L = 16$ . . . . .	158
A.4	OMGC scaling function coefficients for $L = 18$ . . . . .	159
A.5	OMGC scaling function coefficients for $L = 20$ . . . . .	160

# Chapter 1

## Introduction

In molecular physics, exact quantum calculation of nuclear motion is still a pursuit of specialists. Much more research effort has been devoted to the field of electronic structure, for which a variety of computer programs have been developed for productive use even by interested non-specialists. This is far less true for calculations of nuclear motion, whether for very anharmonic bound state vibrations, chemical reactions, isomerizations, photodissociation or other processes. While the basic molecular Hamiltonian for electrons and nuclei is a sum of two-body terms, the use of the Born-Oppenheimer separation results in an effective potential for the nuclear-motion problem, in which many nuclear degrees of freedom are coupled. Cutting-edge calculations must make choices of coordinates, discretizations, and computational algorithms that are far from being standardized. It is in this context that efforts are being made to develop general solvers such as those using the finite element method (FEM) that can be applied no matter what specific coordinates are chosen. Another approach is offered by compact-support wavelet bases such as those derived by Daubechies [1, 2], which simultaneously allow orthogonal bases and multiscale representations. Wavelet methods are still relatively young and technical barriers are still being addressed, but the prospects are good for long-range development of adaptive wavelet methods that

can enable construction of versatile computer programs accessible to an enlarged base of researchers.

There are any number of other fields (fluid mechanics, acoustics, radiative transport, etc.) apart from quantum mechanics that can also benefit from development of efficient wavelet technology. Of specific interest to us is in nanophotonics, the interaction with and manipulation of light by subwavelength particles, and its use in modern molecular spectroscopies. The intense local electromagnetic (EM) fields near noble metal nanoparticles are principal factors in surface-enhanced Raman scattering (SERS) and emerging variations such as surface-enhanced Raman optical activity (SEROA). Near-field calculations can be accomplished for spherical particles using Mie theory and vector spherical harmonics, but more general geometries require use of finite-difference time-domain (FDTD), FEM, the boundary element method, or other numerical methods. Wavelet bases can also be used for time-domain or frequency-domain near-field EM solvers, and the built-in customizable resolution appears especially promising in this regard. A variety of exploratory wavelet calculations have been performed already, including in our own work. SERS and SEROA applications in our group have so far used spherical metal nanoshell substrates for which Mie theory has been adequate, but it is of direct interest to determine if wavelet methods can be at least as computationally efficient as FDTD, FEM, and other EM methods for different geometries, different surface roughnesses, and for adjoined nanoparticles.

Wavelet bases sparked a revolution in signal and image processing during the eighties and nineties. In this context wavelets are used to represent 2D functions (images) with an accuracy governed by what the human eye can discern, e.g., 1 part in

$10^3$  or  $10^4$ . More general functions (such as solutions of multidimensional differential equations) are also expandable in wavelet bases, but some wavelet tools from the signal processing community are not accurate enough for use in the differential equation context. Solution of differential equations generally demands far greater accuracy. This is the reason wavelets are not routinely used for solution of differential equations. It is hoped that tools introduced by our lab will change this.

Basis functions or expansion functions are familiar to scientists. Commonly, thoughts of orthogonal polynomials or Fourier functions come to mind. These are easily written down in a closed analytic form. Orthonormal compact-support wavelets do not have closed analytic forms and are not solutions to differential equations. Instead they satisfy *scaling* relations called two-scale equations (this is where built-in scaling properties of wavelet bases arise). The lack of a closed form is not a problem as wavelet function values are found through iterative use of the two-scale equations. The resulting recursive algorithm begins with exact evaluation of wavelet function values at the integers then subsequently at the half-integers, then at the quarter-integers, and so on. For many purposes the numerically exact evaluation at these dyadic rationals is sufficient, but interpolation can be used if more general positions are required. Methods are available for the calculation wavelet basis function values.

The next challenge was in the determination of wavelet expansion coefficients. Many researchers approximated expansion coefficients of a function by simple samples of that function. For use in representing solutions of differential equations more accuracy is generally demanded. This was partially addressed by the introduction of coiflets (discussed in depth below), special wavelet families for which the expansion

coefficients were much closer to the function samples. More general wavelet quadrature methods were subsequently developed for accurate, systematically improvable calculation of expansion coefficients without requiring use of excessively fine-scaled wavelets or large numbers of function samples. Methods are thus also available for the calculation of wavelet basis expansion coefficients of a function.

The next hurdle for wavelet-based implementations involved the representation of operators, such as differential operators from EM equations or multiplicative (potential) operators from quantum equations. Casting the Schrödinger equation into a finite localized basis form is generally accomplished by evaluating the matrix elements of the Hamiltonian operator between the included basis functions (bilinear integrals). If only a single scale wavelet basis is used, the Hamiltonian matrix takes a particularly simple banded form due to the exact localization of the basis. If multiple scales are used, the overlap matrix is still diagonal, but the Hamiltonian matrix now becomes more complicated and less sparse, leading to the need for special methods to maintain efficiency. The kinetic energy operator matrix elements in Daubechies-like bases are straightforward to evaluate and only a modest number of integrals, calculated as the solutions to linear algebraic equations, are unique. The potential matrix is more difficult for general potential energy surfaces (PESs) but this problem was addressed in the late 1990s by adapting the wavelet quadrature to integrals that were bilinear in basis functions. For a PES with an analytic form, it was also shown possible to use the wavelet two scale relations (for both bra and ket basis functions this time) to evaluate the target matrix elements to any desired accuracy. With a wavelet matrix representation of the Hamiltonian in hand eigenvalues and eigenfunc-

tions are extracted through standard methods. These methods apply equally well to frequency-domain EM equations that are arranged as an eigenvalue equation.

Just as important as eigenpair solutions of the time-independent Schrödinger equation (TISE) is solution of the time-dependent Schrödinger equation (TDSE). A new method for solution of the latter was developed in 2007. The Conjugate Symmetric Lanczos (CSL) method for time-independent Hermitian Hamiltonians derives from time-reversal symmetry and can be viewed as a Lanczos-based propagation algorithm simplified to eliminate storage of most Lanczos vectors. While the wavelet technology discussed above can be used for the spatial (vibrational) coordinates (degrees of freedom), this CSL propagation method is independent of the spatial representation and can be used with other spatial representations. These quantum evolution algorithms are based on the matrix-exponential solution involving the Hamiltonian matrix and the resulting tools can also be used in time-domain solution of Maxwell’s EM equations. This is accomplished by first organizing the EM equations into a Hamiltonian form that resembles the TDSE, but with a “Hamiltonian” involving derivatives and dielectric functions. The CSL method applies immediately to this case, and preliminary research has been carried out into a CSL-type method for absorbing (complex dielectric) media for which the Hamiltonian-like operator is not Hermitian.

What has not been fully addressed yet is how to combine all of the wavelet characteristics – orthogonality, multiresolution description, systematic accuracy, compressibility and dynamical adaptivity – into competitively efficient algorithms. There are already algorithms in use in molecular physics such as the Discrete Variable Representation (DVR) for specific problems such as determination of anharmonic coupled

vibrational energy levels for molecules with a few atoms, and it is desirable that wavelet methods be capable of at least comparable efficiency. Yet, in trying to take matrix-based wavelet eigenvalue calculations to multiple degrees of freedom in either direct-product or contracted-direct-product bases, the limiting factor quickly becomes storage of the Hamiltonian matrix. Even using sparse-matrix representations, it is rather easy to exceed the limits of fast memory.

This is the barrier of most importance at the current moment. It is addressed here by developing a matrix-free approach to applying the Hamiltonian to a vector of wavelet expansion coefficients. This is in principle straightforward for a standard Cartesian kinetic energy operator. For the potential, we take the expansion coefficients for the potential times the wave function as proportional to the product of their individual expansion coefficients. The errors in this approximation are carefully studied and are found to be minimized by certain choices of generalized coiflets that are worked out here. The function approximation capabilities of these bases are measured by their approximation order, which is not as high as for Daubechies wavelets, and will therefore have worse errors in representation of functions. This apparent problem is resolved by the use of other convolution filters that “beat the approximation order.” Related decreases in accuracy upon applying the kinetic energy operator in the generalized coiflet bases are overcome by more accurate differential filters that turn out to be familiar. In the end, coiflet wavelet representations give single-scale bases that are very efficient at calculating the effect of the Hamiltonian operators on a coefficient vector without the need for matrices. Our matrix-free algorithm gives both storage and computational savings. There are even fewer computational steps

used than, e.g., in the sinc DVR method commonly utilized for solutions of general problems. This efficient alternative to the direct matrix-vector multiplication allows determination of select eigenvalues through use of the standard Lanczos algorithm, though in practice strong potential anharmonicities make it preferable to use a more recent robust version that avoids stagnation and/or the storage of too many Lanczos vectors.

We judge these latter results as the most important for our future progress in multidimensional multiscale wavelet calculations, and so they are placed front and center in the layout in Part I of this thesis. As a consequence, some of the subsequent results are not in chronological order. It is hoped that this does not cause confusion.

Moreover, though wavelet use in EM calculations is of strong interest going forward, preliminary theoretical calculations of SEROA are described that are based entirely on Mie theory. This is because experimental SEROA measurements are beginning to appear. However, this is insufficient theoretical assurance that the circular intensity differences are selective for chiral molecules just as they are in ordinary ROA. An electric-dipole Mie theory model of SERS is extended to higher molecular multipoles and combined with the ROA formalism in order to study the special case of molecules near silver and gold metal nanoshells with dielectric cores. This is the subject of Part II of this thesis. It is found that, even without adsorption, the strong local EM fields generally interfere with this chiral selectivity. Different circular polarization strategies are examined, and it is found that the so-called dual circular polarization method for backscatter detection from a spherical plasmonic substrate is predicted to restore the selectivity. Excitation curves of SEROA enhancement are



analyzed for both metals, and particular suggestions are made for choice of excitation region. This represents the first calculation of any type of SEROA where the surface plasmon local fields were fully included and where chiral selectivity was indeed predicted. Addition of surface roughness may be investigated at a future date using other numerical methods, perhaps one of these an efficient wavelet-based EM solver.

Part I

Wavelet Representations in  
Quantum Mechanics and  
Electromagnetics

## Chapter 2

### Compact Support Wavelets

#### 2.1 Scaling and Wavelet Representation

A wavelet transform is a basis representation using members of a fixed shape that are copied, scaled, and translated across the real line to give a scale and location representation in terms of special functions that look like little waves. The wavelet  $\psi_{jk}$  expansion [3] of function  $f$  has the form

$$f(x) = \sum_j \sum_k f_{jk}^\psi \psi_{jk}(x) \quad (2.1)$$

over all integers  $j$  and  $k$ . The basis functions  $\psi_{jk}$  are orthonormal, oscillatory, strictly localized functions created as scaled and translated copies of a single *mother* wavelet  $\psi$ ,

$$\psi_{jk}(x) = 2^{j/2} \psi(2^j x - k) . \quad (2.2)$$

A typical example of  $\psi$  is shown in red in Fig. 2.1. The idea of shifting, or translation, is shown with the black thin-lined wavelets. The colored wavelets depict the scaling idea, the finer-scale (higher  $j$ ) functions are squeezed versions of the  $j = 0$  function

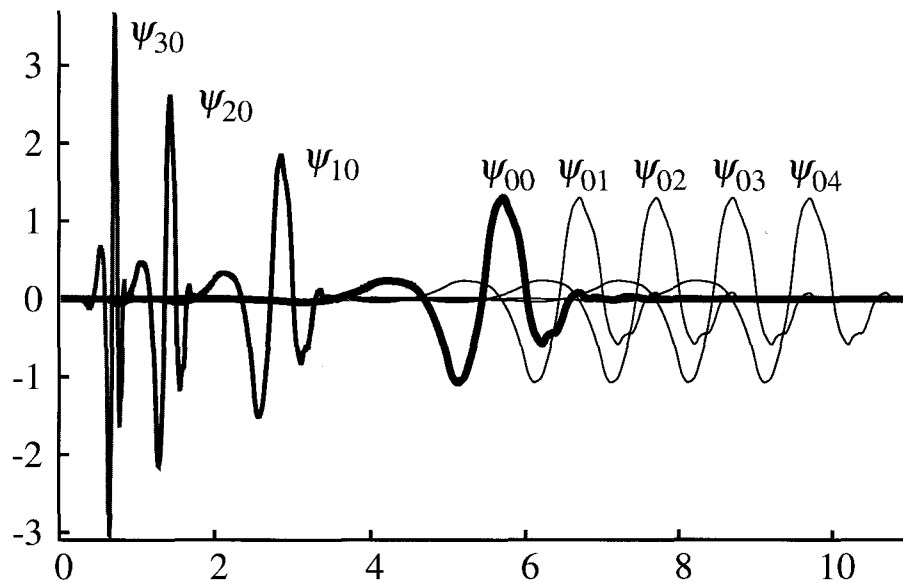


Figure 2.1: Examples of scaled wavelets at  $j = 0, 1, 2$  and  $3$ , all with location  $k = 0$ . These are the functions  $\psi = \psi_{00}, \psi_{10}, \psi_{20}$ , and  $\psi_{30}$ , respectively. Translated versions of the red  $j = 0$  wavelet are shown with thin black lines, they are  $\psi_{0k}$  with  $k = 1, 2, 3$  and  $4$ .

$\psi$ . These two ideas are important because a wavelet representation is an alternative description of  $f$  using scaled wavelets that are translated across a domain as written in Eq. (2.1).

The *wavelet transform* is formed by the *expansion coefficients* or *projection coefficients*  $f_{jk}^\psi$  that are linear projection integrals labeled by scale index  $j$  and translation index  $k$

$$f_{jk}^\psi = \langle \psi_{jk} | f \rangle = \int \psi_{jk}(x) f(x) dx . \quad (2.3)$$

The terms expansion coefficients and projection integrals are used interchangeably throughout since the  $\psi_{jk}$  form an orthonormal basis. Each wavelet expansion coefficient  $f_{jk}^\psi$  is a finite integral since the basis members  $\psi_{jk}$  have compact support, or

strict localization, i.e., they are nonzero on a finite interval (see Fig. 2.1). Wavelets provide a representation labeled with two indices, the translation index providing the location of the basis function on the real line, and the scale index providing the information about resolution in a manner loosely analogous to use of frequency. The wavelet shape being fixed, the slowly-varying aspects of a function are analyzed with wider wavelets and the detailed transient aspects are analyzed with thinner wavelets. This is shown later in Fig. 2.3.

Actual implementations of a wavelet transform are unable to keep or calculate an infinite number of location-indexed coefficients for every scale  $j$ ,  $f_{jk}^\psi$ . For sufficiently smooth functions  $f$  we can dispense with the finer scale wavelets  $\psi_{jk}$ , with larger  $j$ , by truncating the  $j$  sum in Eq. (2.1) at some upper scale cutoff. Any errors in the wavelet basis expansion resulting from the truncation can be reduced through inclusion of even finer scale wavelets.

A similar problem persists at the opposite end. One really does not want to continue  $j$  to  $-\infty$ , i.e., infinitely coarse mother wavelets. For typical wavelet representations, one chooses a coarsest scale and uses there a basis created by translates of a father wavelet or scaling function  $\phi$  [1, 4, 2]. These, like  $\psi$ , have scaled (index  $j$ ) and translated (index  $k$ ) copies,

$$\phi_{jk}(x) = 2^{j/2} \phi(2^j x - k) . \quad (2.4)$$

The functions  $\phi$  and  $\psi$  have complementary characteristics that will be discussed below.

This scaling and shifting description also applies to the wavelet functions from Eq. (2.2). The wavelets are also unit square-normalized over all scales,  $\langle \psi_{jk} | \psi_{jk} \rangle = 1$ . A typical example of  $\phi$  is shown in red in Fig. 2.2.

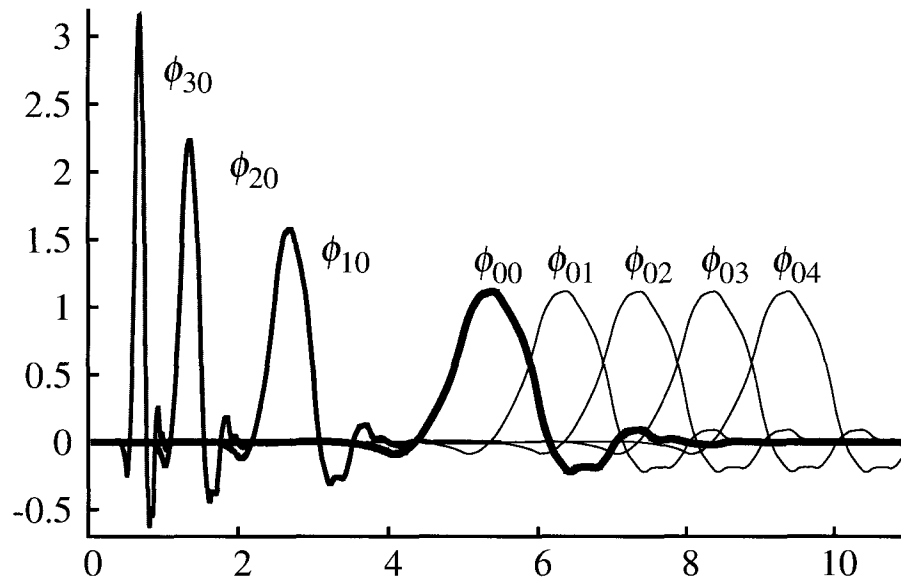


Figure 2.2: Examples of scaled scaling functions at  $j = 0, 1, 2$  and  $3$ , all with location  $k = 0$ . These are the functions  $\phi = \phi_{00}, \phi_{10}, \phi_{20}$ , and  $\phi_{30}$ , respectively. Translated versions of the red  $j = 0$  scaling function are shown with thin black lines, they are  $\phi_{0k}$  with  $k = 1, 2, 3$  and  $4$ .

Instead of the expansion as presented in Eq. (2.1), the multiscale wavelet representation of  $f$  is now described in linear combinations of scaled and translated scaling and wavelet functions over a limited scale range

$$f(x) = \sum_k f_{0k} \phi_{0k}(x) + \sum_{j'=0}^{j-1} \sum_k f_{j'k}^\psi \psi_{j'k}(x) + \mathcal{O}(2^{-jM}). \quad (2.5)$$

The first sum over integer  $k$  involves single-scale linear projection integrals over scaling

functions,

$$f_{jk} = \langle \phi_{jk} | f \rangle = \int \phi_{jk}(x) f(x) dx , \quad (2.6)$$

and basis function values  $\phi_{jk}(x)$ , while the second integer sums are scale-truncated versions of Eq. (2.1). The error of this expansion is governed by a positive integer  $M$ , the approximation order of the basis. This multiscale decomposition gives coarse-scale information in the  $j = 0$  scaling function plus different levels of detail using different scale wavelets over a range of  $j'$  values. An important notion is the alternative, but equivalent, single-scale representation at level  $j$ ,

$$f(x) = \sum_k f_{jk} \phi_{jk}(x) + \mathcal{O}(2^{-jM}) , \quad (2.7)$$

which offers a localized orthonormal basis expansion.

A final generalization, which is useful in applications and also in theoretical error analysis, allows the scale on level  $j = 0$ , reflected in the spacing between basis members  $k$  and  $k + 1$ , to differ from unity. This is accomplished by the introduction of the real-valued spacing parameter  $\lambda$ , resulting in  $\lambda$ -spaced basis function as discussed below.

Certain notational conventions are used throughout. The presence of a single integer subscript indicates translation, for example,  $\phi_k(x) = \phi(x - k)$ , with the obvious special case  $k = 0$  giving  $\phi_0(x) = \phi(x)$ . The presence of two integer subscripts,  $j$  and  $k$ , indicates change of scale by  $2^{-j}$  and translation by  $k$  units on that scale, Eq. (2.4),

with the special case  $j = 0$  giving  $\phi_{0k}(x) = \phi_k(x)$ . Finally, if the  $j = 0$  basis has spacing  $\lambda$  that is not necessarily unity, this is indicated by a superscript,

$$\phi_{jk}^\lambda(x) = \left(\frac{2^j}{\lambda}\right)^{1/2} \phi\left(\frac{2^j x}{\lambda} - k\right) = \lambda_j^{-1/2} \phi\left(\frac{x}{\lambda_j} - k\right), \quad (2.8)$$

with the special case  $\lambda = 1$  giving  $\phi_{jk}^1(x) = \phi_{jk}(x)$ . Scales for higher  $j$  are now written

$$\lambda_j = \lambda/2^j. \quad (2.9)$$

Similar conventions are used for  $\psi(x)$ .

The reference functions  $\phi(x)$  and  $\psi(x)$  are both square-normalized to unity and are orthogonal to each other, as well as each other's translates. Considering more general scales, the full set of orthogonality relations are enumerated as

$$\int \phi_{jk}^\lambda(x) \phi_{jk'}^\lambda(x) dx = \delta_{kk'} \quad (2.10)$$

$$\int \psi_{jk}^\lambda(x) \psi_{j'k'}^\lambda(x) dx = \delta_{jj'} \delta_{kk'} \quad (2.11)$$

$$\int \phi_{jk}^\lambda(x) \psi_{j'k'}^\lambda(x) dx = 0 \quad j' \geq j. \quad (2.12)$$

The Kronecker delta  $\delta_{kk'}$  is one when the two indices are equal and zero otherwise. The first line states translation orthonormality between same-scale scaling functions. The second line states translation orthonormality between same-scale wavelets as well as orthogonality between different-scale wavelets. The last line states orthogonality between scaling and wavelet functions on possibly different scales as long as the scaling



functions are members of the coarsest scale. Other important reference function conditions translate to the  $\lambda$ -scaled members as

$$\int \phi_{jk}^\lambda(x) dx = \sqrt{\lambda_j} \quad (2.13)$$

$$\int \psi_{jk}^\lambda(x) dx = 0 . \quad (2.14)$$

From these equations important properties of the fundamental functions are apparent. The father wavelet  $\phi$  has unit area while the mother wavelet  $\psi$  has vanishing area.

Wavelet representation projection integrals of a particular test function are shown in Fig. 2.3. The colored dots depict different resolutions of scaling function expansions of the form in Eq. (2.7). Within this single-scale point of view more function details are recovered as the level  $j$  is increased. In the alternative multiscale form of Eq. (2.5) a single level of coarse-scale scaling functions capture the main, slowly-varying information (red dots) while finer-scale wavelets (colored pluses) capture details such as points and edges. The colored pluses are essentially zero everywhere except sharp transitions.

It is sometimes simplest to use a scaling function representation at a fixed scale. This scale can be chosen sufficiently fine so as to encompass the important dynamic variations of the function analyzed. This can be wasteful, however. Employing the multiscale representation opens the door to other possibilities such as compression (i.e., selective deletion of wavelet functions whose expansion coefficients are negligible) or noise reduction.

With  $\lambda$ -scaled members, the single-scale and multi-scale decompositions of a func-

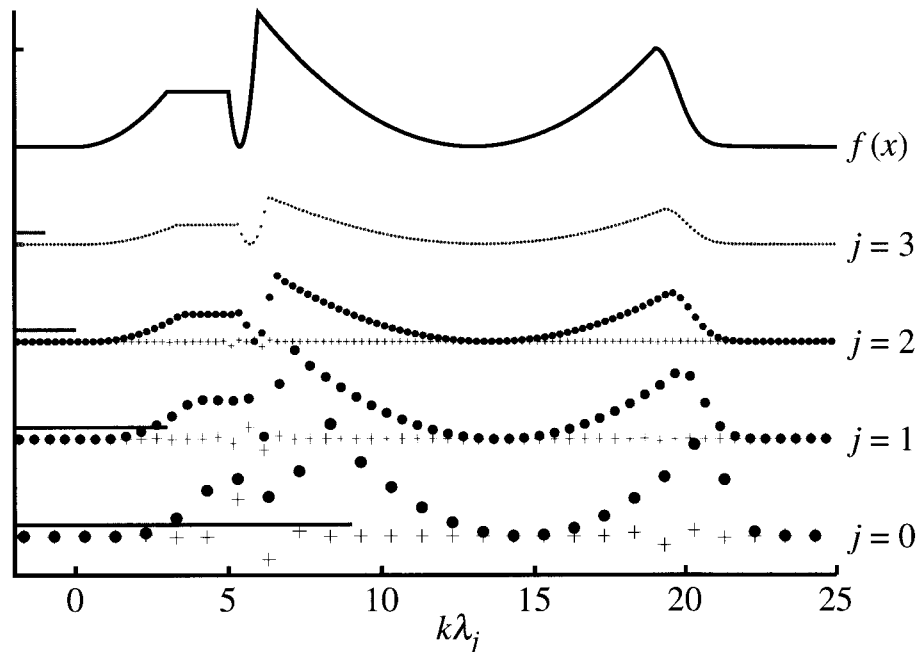


Figure 2.3: Scaling and wavelet decomposition of an example function  $f$  (top black trace). The colored dots are scaling function projection integrals and colored pluses are wavelet projection integrals. All colored traces have a uniform vertical offset for clarity. The discrete coefficients are depicted at real space locations  $k\lambda_j$ , the left-hand edge of each basis function, for  $k_{\min,j} \leq k \leq k_{\max,j}$ . The coefficients at the coarsest representation,  $j = 0$ , are spaced by  $\lambda = 1$  while the ones at the finest resolution,  $j = 3$ , are spaced by  $1/2^3 = 1/8$ . The colored bars on the left depict the extent/support of a scale- $j$  basis function (compare to Figs. 2.1 and 2.2).

tion  $f$  are given in final form,

$$f(x) = \sum_k f_{jk}^\lambda \phi_{jk}^\lambda(x) + \mathcal{O}(\lambda_j^M) \quad (2.15)$$

$$f(x) = \sum_k f_{0k}^\lambda \phi_{0k}^\lambda(x) + \sum_{j'=0}^{j-1} \sum_k f_{j'k}^{\psi,\lambda} \psi_{j'k}^\lambda(x) + \mathcal{O}(\lambda_j^M). \quad (2.16)$$

These equations are more general versions of Eqs. (2.7) and (2.5). The expansion

coefficients

$$f_{jk}^\lambda = \langle \phi_{jk}^\lambda | f \rangle = \int \phi_{jk}^\lambda(x) f(x) dx \quad (2.17)$$

$$f_{jk}^{\psi,\lambda} = \langle \psi_{jk}^\lambda | f \rangle = \int \psi_{jk}^\lambda(x) f(x) dx . \quad (2.18)$$

are given as integrals over compact support functions  $\phi_{jk}^\lambda(x)$  and  $\psi_{jk}^\lambda(x)$  that are both nonzero on the support

$$[k\lambda/2^j, (k + L - 1)\lambda/2^j] . \quad (2.19)$$

The  $L - 1$  term on the right hand side covers the extent of the last compact support function. This is discussed further in Section 2.3.

Later, in Section 2.2, efficient methods are discussed that enable the multiscale wavelet projection coefficients from Eq. (2.16) to be found through single-scale scaling function projection coefficients.

## 2.2 Multiresolution Analysis and the Two-Scale Equations

Here we discuss the underlying concept of a multiresolution analysis (MRA) [4]. Orthonormal wavelet bases, and their multi-scaling properties, provide concrete realizations of an MRA. That is, the  $\phi_{jk}^\lambda$  and  $\psi_{jk}^\lambda$  members form a basis for an MRA of general functions [3]. The orthogonal wavelets considered here allow an MRA corresponding to function subspaces at different resolutions that do not overlap.

For a particular resolution level  $j$ , the set of  $\phi_{jk}^\lambda$  for all integer  $k$  forms an orthonormal basis for the subspace denoted by  $\mathcal{V}_j$ . This subspace represents all linear

combinations of the  $\phi_{jk}^\lambda$ . The corresponding  $\psi_{jk}^\lambda$  members are an orthonormal basis for the subspace denoted by  $\mathcal{W}_j$ . This subspace represents all linear combinations of the  $\psi_{jk}^\lambda$ . The single-scale scaling function expansions of Eq. (2.15) are orthogonal projections of  $f$  onto the  $\mathcal{V}_j$  subspace. Similarly, the multi-scale expansion in Eq. (2.16) give orthogonal projections of  $f$  onto the disjoint subspaces  $\mathcal{V}_0, \mathcal{W}_0, \mathcal{W}_1, \dots, \mathcal{W}_{j-1}$ .

Since there is always more information about  $f$  at higher resolution, a coarser subspace is contained in a finer one, that is, the  $\mathcal{V}_j$  form a nested sequence of vector subspaces

$$\dots \subset \mathcal{V}_{j-1} \subset \mathcal{V}_j \subset \mathcal{V}_{j+1} \subset \mathcal{V}_{j+2} \subset \dots . \quad (2.20)$$

Therefore, all information from coarser-scale  $\mathcal{V}_{j'}$  subspaces is contained in  $\mathcal{V}_j$  for  $j' \leq j$ . This is reflected in the amplitude of the expansion coefficients shown in Fig. 2.3. For each scale index  $j$ , the dots represent the projections on  $\mathcal{V}_j$ . Due to the subspace nesting, the information about level- $j$  coefficients is then also contained in  $\mathcal{V}_{j+1}$ ,  $\mathcal{V}_{j+2}$ , etc.

Finer subspaces  $\mathcal{V}_j$  (higher  $j$ ) give zoomed representations, offering more information when compared to coarser-scale representations (lower  $j$ ). Wavelet functions, spanning the  $\mathcal{W}_j$  subspace, arise naturally in a MRA decomposition. The former contain the differences between  $\mathcal{V}_j$  and  $\mathcal{V}_{j+1}$ . The MRA analysis shows that wavelet functions arise from orthogonal differences between neighboring-scale scaling function representations. It will be shown that this implies that the whole wavelet system is formed from a single function,  $\phi$ , the father function.

The nesting of  $\mathcal{V}_j$  in  $\mathcal{V}_{j+1}$  is realized in the construction by Daubechies, who

stipulated that each scaling function  $\phi_{jk}$  is a real linear combination of only those  $\phi_{j+1,k}$  entirely contained in the former's support of  $[0, L-1]$ , for even  $L$ . For example, the father function, being an element of  $\mathcal{V}_0$ , is contained in  $\mathcal{V}_1$  and can be written as a linear combination of  $\phi_{1k}$  functions,

$$\phi(x) = \sum_{k=0}^{L-1} h_k \phi_{1k}(x) = \sum_{k=0}^{L-1} h_k \sqrt{2} \phi(2x - k) = \sum_{k=0}^{L-1} c_k \phi(2x - k) . \quad (2.21)$$

This is the *dilation equation* or *two-scale equation* of the scaling functions and it states that coarser-scale scaling functions are linear combinations of shifted, finer-scale scaling functions. The last equality shows two common alternate coefficient conventions, related by  $c_k = \sqrt{2} h_k$ . The first choice,  $h_k$ , is more appropriate to expressing  $\phi(x)$  as a linear combination of the  $\phi_{1k}(x)$  functions as they are defined in Eq. (2.4), while the second choice,  $c_k$ , is more appropriate to expressing  $\phi(x)$  as a linear combination of the same function with scaled and shifted arguments. The basis members  $\phi_{jk}$  retain their normalization no matter the choice of coefficient normalization.

Since, as discussed above,  $\mathcal{W}_0 = \mathcal{V}_1 \ominus \mathcal{V}_0$  and  $\mathcal{W}_0$  is orthogonal to  $\mathcal{V}_0$  ( $\mathcal{W}_0 \perp \mathcal{V}_0$ ), all members of  $\mathcal{W}_0$  can also be written in terms of the members of  $\mathcal{V}_1$ . For the mother function, then,

$$\psi(x) = \sum_{k=0}^{L-1} g_k \phi_{1k}(x) = \sum_{k=0}^{L-1} g_k \sqrt{2} \phi(2x - k) = \sum_{k=0}^{L-1} d_k \phi(2x - k) . \quad (2.22)$$

Again, the last equality gives an example of an alternate coefficient normalization

that absorbs the  $\sqrt{2}$  factor as  $d_k = \sqrt{2} g_k$ . The first equality makes it clear that  $\psi(x)$  is a linear combination of the same finer-scale  $\phi_{1k}(x)$  functions used for  $\phi(x)$ . This is the wavelet *two-scale equation*, and it states that coarser scale wavelet functions are linear combinations of shifted, finer-scale scaling functions. The  $c_k$  and  $d_k$  choices of normalization are usually chosen below.

Eqs. (2.21) and (2.22) state that father and mother functions are linear combinations of the  $L$  half-width scaling functions that are entirely contained in the interval  $[0, L-1]$ . Continuing the subspace containment arguments of the last two paragraphs leads to general level- $j$  *two-scale equations*

$$\phi_{jk}^\lambda(x) = 2^{-1/2} \sum_{k'=0}^{L-1} c_{k'} \phi_{j+1,2k+k'}^\lambda(x) \quad (2.23)$$

$$\psi_{jk}^\lambda(x) = 2^{-1/2} \sum_{k'=0}^{L-1} d_{k'} \phi_{j+1,2k+k'}^\lambda(x) . \quad (2.24)$$

They are general-scale versions of Eqs. (2.21) and (2.22). These equations can be derived through substitution of  $2^j x - k \rightarrow x$  in Eqs. (2.21) and (2.22) and using Eqs. (2.4) and (2.2).

The two-scale equations provide a fast method to transform from a single scale representation to a multiscale representation. This is accomplished through use of the low pass (detail-suppressing) operation

$$f_{jk}^\lambda = 2^{-1/2} \sum_{k'=0}^{L-1} c_{k'} f_{j+1,2k+k'}^\lambda \quad (2.25)$$

and the high pass (detail-extracting) operation

$$f_{jk}^{\psi,\lambda} = 2^{-1/2} \sum_{k'=0}^{L-1} d_{k'} f_{j+1,2k+k'}^{\lambda} . \quad (2.26)$$

These equations are derived through multiplication of Eqs. (2.23) and (2.24) by the function  $f(x)$  followed by integration over  $x$ . The low-pass and high-pass filters also offer fast transformations for projection coefficients between different scale representations. The level  $j - 1$  coefficients are easily calculated from level  $j$  coefficients, a direct consequence of the nested subspace structure of a MRA [Eq. (2.20)] and the two-scale equations [Eqs. (2.21) and (2.22)].

The transformation of the  $f_{jk}^{\lambda}$  to the multiscale representation  $f_{0k}^{\lambda}$  and  $f_{jk}^{\psi,\lambda}$  (over a finite range of  $j$ ) proceeds through use of the coefficients  $c_k$  and  $d_k$  alone. In fact, the actual basis members are not needed in the calculation of the wavelet transform, just the coefficients  $c_k$  and  $d_k$ . The calculation of these coefficients for different wavelet families is discussed in Section 2.3 and 2.5.

In applications, the representation index takes the values  $k_{\min,j} \leq k \leq k_{\max,j}$ , different for each level  $j$ , to cover a total spatial range of

$$[x_{\min}, x_{\max}] = [k_{\min,j} \lambda / 2^j, (k_{\max,j} + L - 1) \lambda / 2^j] . \quad (2.27)$$

The spatial range is then tuned with  $k_{\min,j}$  and  $k_{\max,j}$  values that are truncated for the physical region of interest. Along with the  $j$  truncation already discussed, this  $k$ -truncation reduces that basis to finite rank and allows the use of square-integrable

basis techniques. Independent  $k$ -truncations on different scale levels  $j$  of an MRA allow the calculations to be more efficient.

### 2.2.1 Wavelet Transform and Pyramid Algorithm

The low-pass and high-pass filters in Eqs. (2.25) and (2.26) are iteratively applied to transform the single-scale representation to the multiscale representation. This is shown in Fig. 2.4. Once a scaling function representation  $f_{jk}^\lambda$  is found this *pyramid*

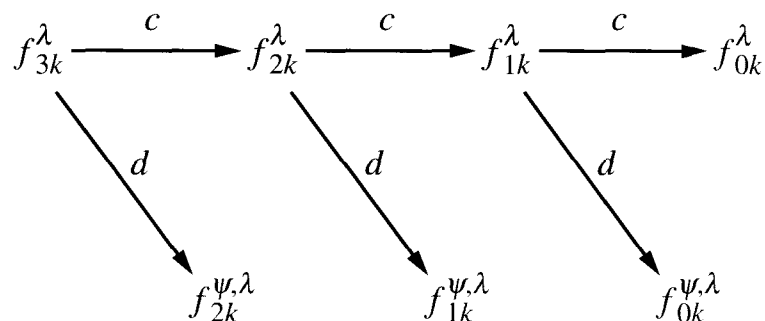


Figure 2.4: Pyramid algorithm: repeated application of low and high pass filters, depicted by  $c$  and  $d$ , respectively. The single-scale representation is shown in red (as are the other sets of coefficients in the top row) and the multiscale representation is shown in blue.

*algorithm* allows fast transformation to the multiscale representation. The low pass and high pass filterings are implemented through Eqs. (2.25) and (2.26) directly. In practice, basis functions are chosen to cover a finite range, to give a finite number of expansion coefficients. This was discussed in Section 2.1. The transformation from  $f_{jk}^\lambda$  to  $f_{j-1,k}^\lambda$  results in a representation with half the density of basis functions.

The cascaded application of the low pass filter also has application in projection coefficient refinement discussed next.



### 2.2.2 Scaling Function Expansion Coefficient Refinement

Single scale expansion coefficients calculated by wavelet quadrature in Eq. (2.47) have  $\mathcal{O}(\lambda_j^{r+1/2})$  errors for integer  $r > 0$ . Quadrature *refinement* can be used to accelerate/improve the error order (control the absolute accuracy) of wavelet quadrature through use of the low pass operation of Eq. (2.25). Refinement proceeds by multi-point (r-point) quadrature at a fine scale  $j = J > 0$  to calculate  $f_{Jk}^\lambda$  with errors of  $\mathcal{O}((\lambda/2^J)^{r+1/2})$  (which can be made as small as desired), followed by iterative recursion to coarser levels  $j < J$ . The latter operation is depicted in the top row of Fig. 2.4, where fine scale projection integrals are transformed, through discrete convolution with the  $c_k$  coefficients, to coarser scale projection integrals.

The refinement procedure uses the low pass operation to transform from the accurate  $f_{Jk}^\lambda$  to  $f_{J-1,k}^\lambda$  without loss of accuracy, followed by the transformation of  $f_{J-1,k}^\lambda$  to  $f_{J-2,k}^\lambda$ , etc. This can be continued to any target level, say  $j = 0$ . (In an MRA, one can also use the high-pass operation along the way to calculate enhanced-accuracy wavelet function projections.) The convergence of the  $f_{jk}^\lambda$  (gotten from some  $f_{Jk}^\lambda$  with  $J > j$ ) calculated by this refinement procedure can be monitored by changing the finest level  $J$ . Thus it is possible to obtain any of the projection integrals for a function  $f$  as accurately as needed.

For sufficiently fine single-scale calculations refinement is not necessary as the spacing  $\lambda_j$  gives acceptable quadrature error orders. In this case, the multi-point or single-point quadrature of Section 2.6 are all that is necessary.

## 2.3 Daubechies Scaling Function Coefficients

Wavelet bases have been introduced as orthonormal localized expansion functions. The multiscale properties were then introduced in Section 2.2, along with efficient algorithms to calculate multiscale representations as well as refinement techniques for expansion coefficients. The properties and construction of the Daubechies wavelet family is discussed in this section.

Daubechies constructed the first family of orthogonal compact support wavelets in the eighties [1, 2]. These wavelets form families indexed by their length  $L$  (positive even number) or by their approximation order  $M = L/2$ . The support of these functions is on the interval  $[0, L - 1]$  (cf. Eq. (2.19)) and the scaling functions are designed to expand  $M$  monomials  $x^p$  exactly for  $p = 0, 1, \dots, M - 1$ . Representative examples of the Daubechies family are shown in Fig. 2.5. Pointwise, these functions have only a limited number of continuous derivatives. As the support length grows, so also does the local smoothness of the father function  $\phi$  and the mother function  $\psi$ . More globally,  $\psi$  also tends to become more oscillatory with  $L$ . The scaling functions are also asymmetric, with most of the scaling function amplitude or energy (in signal-processing language) biased towards the left side of the interval. Daubechies also constructed compact support families with more symmetric scaling functions, which are called *least asymmetric* wavelets or *symmlets*. Complete symmetry of an orthogonal compact support wavelet family was proven impossible except for the discontinuous Haar basis with  $L = 2$ . Symmlets are closely related, but have scaling functions with maximum amplitude closer to the center of their support.

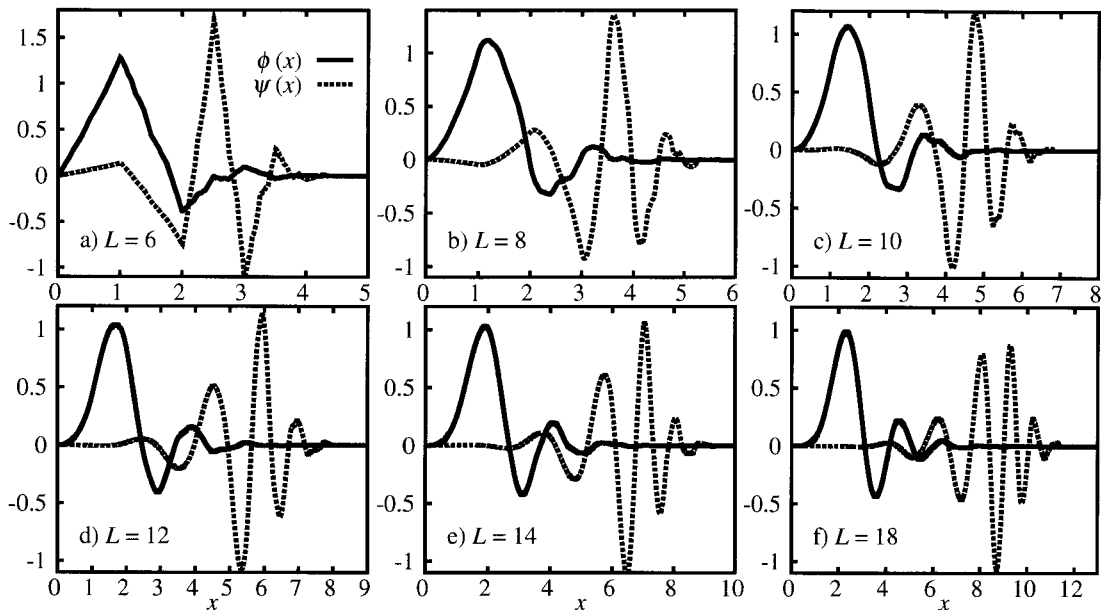


Figure 2.5: Scaling functions  $\phi(x)$  and corresponding wavelet functions  $\psi(x)$  for Daubechies compact support family of different lengths  $L$  and approximation orders  $M = L/2$ . Most plots are presented on a reduced  $x$ -range for clarity, the functions being graphically negligible well before  $x = L - 1$ .

Daubechies constructed the father function to have unit area  $\int \phi(x) dx = 1$  and to be orthogonal to integer-translated copies of itself  $\int \phi(x) \phi(x - k) dx = \delta_{0k}$ . These are the fundamental restrictions underlying the scaled-basis relations of Eqs. (2.13) and (2.10). The mother function, on the other hand, is required to have vanishing area  $\int \psi(x) dx = 0$  while also being orthogonal to integer translated copies of itself  $\int \psi(x) \psi(x - k) dx = \delta_{0k}$  and to all integer translates of scaling functions  $\int \phi(x - k) \psi(x - k') dx = 0$ . Daubechies added further constraints that  $\psi$  have a maximal number,  $M = L/2$ , of vanishing *wavelet moments*

$$\int \psi(x) x^p dx = 0 \quad p = 0, \dots, M - 1, \quad (2.28)$$

for a given  $L$ . The  $p = 0$  condition is already expressed with the vanishing area

requirement. As mentioned above, the number of vanishing wavelet moments is the approximation order of the basis, a measure that is also related to the number of monomials representable by scaling functions.

Daubechies' wavelet families were constructed to satisfy the two-scale equations from Section 2.2. In that section the *fundamental coefficients*,  $c_k$  and  $d_k$ , were introduced. The importance of these scaling and wavelet coefficients cannot be overstated. The  $c_k$  in particular are tabulated for all the familiar wavelet families, and the differences between families are directly reflected in the differences between the coefficients. It is useful to understand properties of the resulting  $\phi$  and  $\psi$  through analysis of the constraints placed on construction of the  $c_k$  and  $d_k$ . Requirements on the father and mother functions are translated to conditions/constraints of the discrete coefficients. These lead to a system of linear and quadratic equations for these coefficients which can be solved numerically.

The orthogonality conditions,  $\int \psi(x) \psi(x - k) dx = \delta_{0k}$  and  $\int \phi(x - k) \psi(x - k') dx = 0$  (considering the  $k = 0$  case is sufficient) imply that

$$\sum_{k=0}^{L-1} c_k d_{2k'+k} = 0 \quad k' = 0, \dots, L/2 - 1 \quad (2.29)$$

$$\sum_{k=0}^{L-1} d_k d_{2k'+k} = 2\delta_{0k'} \quad k' = 0, \dots, L/2 - 1. \quad (2.30)$$

With the choice

$$d_k = (-1)^k c_{L-1-k}, \quad (2.31)$$

usually made, Eqs. (2.29) and (2.30) are automatically satisfied with no further con-

siderations. The fundamental wavelet coefficients are reversed  $c_k$  with alternating minus signs. This is exactly how the mother function is created in terms of the father function. Thus, the compact-support wavelet family is built entirely from the father function's fundamental coefficients  $c_k$ , cf. Eq. (2.24).

By use of the two-scale relations and judicious changes of integration variable, the conditions above become expressed in terms of equations that the  $c_k$  must satisfy

$$(i) \quad \sum_{k=0}^{L-1} c_k = 2 \quad (2.32)$$

$$(ii) \quad \sum_{k=0}^{L-1} c_k c_{2n+k} = 2\delta_{n0} \quad n = 0, \dots, L/2 - 1 \quad (2.33)$$

$$(iii) \quad \sum_{k=0}^{L-1} (-1)^k c_k k^p = 0 \quad p = 0, \dots, M - 1. \quad (2.34)$$

To find the coefficients we assume all  $c_k = 0$  for  $k < 0$  and  $k \geq L$  and solve conditions (i)–(iii) for real  $c_k$  simultaneously.

As discussed in the Introduction, scaling functions and wavelet functions do not have closed analytic forms. This is not a problem as basis function values are found through iterative use of the two-scale equations. Scaling function values can be exactly evaluated at integers, half-integers, quarter-integers, etc. This recursive solution strategy begins with the calculation of integer values  $\phi(1), \phi(2), \dots, \phi(L - 2)$  (the endpoints at  $x = 0$  and  $x = L - 1$  are identically zero). These integer values are found as eigenvectors of an eigenvalue problem created from the two-scale equations [Eq. (2.21)]. The correct normalization of the integer values are then established through use of the rule  $\sum_k \phi_k(x) = 1$ , discussed below. Half-integers are found next

from the solved integer values, quarter-integers are found in terms of the half-integer values, etc. This method is used for the for the generation of scaling and wavelet function plots from Fig. (2.5) and any basis function plots that follow. As the basis function values are gotten only in terms of the  $c_k$ , this is an important example that demonstrates why focus is placed squarely on the fundamental coefficients – a wavelet basis is defined completely in terms of the  $c_k$  coefficients. Wavelet function values are calculated in the same recursive manner but using the  $d_k$  from Eq. (2.31) for one step of the process.

The compact support of these fundamental functions is directly related to the finite number of  $c_k$  and  $d_k$  coefficients. The resulting support [cf. Eq. (2.19)] is dictated by the indexing convention of the fundamental coefficients. The choice adopted here,  $k = 0, 1, \dots, L - 1$ , gives fundamental functions of nonzero support interval  $[0, L - 1]$ . Daubechies family characteristics are listed in Table 2.1 to accompany the plots of representative examples shown in Fig. 2.5. The Hölder exponent  $\alpha$  also shown in the

Table 2.1: Approximation orders, first moments [of Eq. (2.35)], and Hölder exponents for Daubechies scaling functions approximation order  $M$  and length  $L = 2M$ .

Daubechies scaling functions							
$L$	$M$	$m_1$					$\alpha$
4	2	0.633	974	596	215	561	4 0.5500
6	3	0.817	401	167	810	880	2 1.0878
8	4	1.005	393	213	443	250	9 1.6179
10	5	1.193	908	018	023	822	9 1.9690
12	6	1.382	160	319	031	218	6 2.1891
14	7	1.569	983	929	935	793	6 2.4604
16	8	1.757	369	493	552	121	2 2.7608
18	9	1.944	350	187	485	118	5 3.0736
20	10	2.130	968	265	544	625	1 3.3640

table is an index of worst-case local smoothness for the scaling functions. Higher  $L$  yields higher  $\alpha$  and better worst-case smoothness/differentiability [2]. The Hölder exponents have been calculated with a variation of the methods of Rioul [5].

## 2.4 Scaling Function Moments

Fundamentally important quantities in practical calculations are moments, which can also be determined directly from the  $c_k$  coefficients (covered in the preceding section). The wavelet families discussed in this thesis have vanishing wavelet moments. The corresponding continuous *scaling function moments*

$$m_p = \int \phi(x) x^p dx \quad (2.35)$$

are important quantities in wavelet-based calculations. Substitution of Eq. (2.21) into the scaling function moment definition from Eq. (2.35) gives a continuous moment relation

$$m_p = 2^{-p} \sum_{q=0}^p \binom{p}{q} \mu_{p-q} m_q \quad (2.36)$$

involving discrete scaling function moments  $\mu_p = \frac{1}{2} \sum_{k=0}^{L-1} c_k k^p$ .

It has been established from the unit-area requirement and Eq. (2.32) that  $m_0 = \mu_0 = 1$ . The remaining moments are easily calculated recursively through Eq. (2.36),

using  $\mu_0$  and  $m_0$  starting values, as

$$m_p = (2^p - \mu_0)^{-1} \sum_{q=0}^{p-1} \binom{p}{q} \mu_{p-q} m_q . \quad (2.37)$$

This expression is found by isolating  $m_p$  after separating the  $q = p$  term from the sum in Eq. (2.36). This is an exact method of calculation for continuous scaling function moments without direct evaluation of integrals. All that is needed are the  $c_k$  coefficients.

Another property, related to approximation order, concerns the expansion of monomials exactly, for  $p = 0, 1, \dots, M - 1$ , as

$$x^p = \sum_k x_{kp} \phi_k(x) . \quad (2.38)$$

Compact support wavelet families are said to exactly *interpolate* monomials up to order  $M - 1$ . The scaling functions, then, form an exact expansion basis for polynomials up to order  $M - 1$ . The expansion coefficients  $x_{kp} = \int \phi_k(x) x^p dx$  can be exactly calculated in terms of the moments  $m_p$  by change of integration variable and use of the binomial expansion.

## 2.5 Generalized Coiflet Scaling Function Coefficients

Daubechies also constructed wavelet families named after R. Coifman. We discuss a generalized version of them that will be important later. These generalized “coiflets” satisfy the same conditions of the Daubechies families discussed in Section 2.3 but



are distinguished by vanishing *shifted* moments of the father function

$$\int \phi(x) (x - m_1)^p dx = \delta_{p0} \quad 0 \leq p \leq N - 1 . \quad (2.39)$$

These requirements translate to  $N$  conditions on the canonical scaling function moments from Eq. (2.35)

$$m_p = \int \phi(x) x^p dx = m_1^p \quad 0 \leq p \leq N - 1 . \quad (2.40)$$

The previous two equations state *power-law moment conditions*. These extra shifted scaling function moment conditions result in relaxed number of vanishing wavelet moments, Eq. (2.28), when compared to Daubechies wavelet families of the same  $L$ . Coiflets have had the importance that approximation of expansion coefficients is simplified, as will be discussed in the next section.

Coiflet fundamental coefficients are also found through solution of equations involving the  $c_k$ . Along with conditions (i)–(iii) from Eqs. (2.32)–(2.34), the shifted scaling function moments translate to further conditions

$$(iv) \quad \sum_{k=0}^{L-1} c_k k^p = 2 m_1^p \quad p = 0, \dots, N - 1 . \quad (2.41)$$

on the  $c_k$  coefficients. These conditions are derived from Eq. (2.40) through use of Eq. (2.21). In the coiflet case, the orthogonality conditions (ii) are contained in conditions (iii) and (iv) and do not need to be included in the governing set of equations for the  $c_k$ .

The design goal in the construction of the original coiflets [6] was to make  $N$  and  $M$  equal. The equations determining the  $c_k$  are again a mixture of linear and quadratic equations (with a certain amount of redundancy), so that an extra scaling function moment obeying Eq. (2.40) was found [7] “for free.” Here and below, to be definite,  $N$  and  $M$  are always meant to indicate the full number of actual moment conditions satisfied. From Table 2.2 it is seen that the usual coiflet families are all characterized by  $N = M + 1$ . Plots of representative examples from Table 2.2 are shown in Fig. 2.6. In comparing this data to Table 2.1, it is seen that the penalty

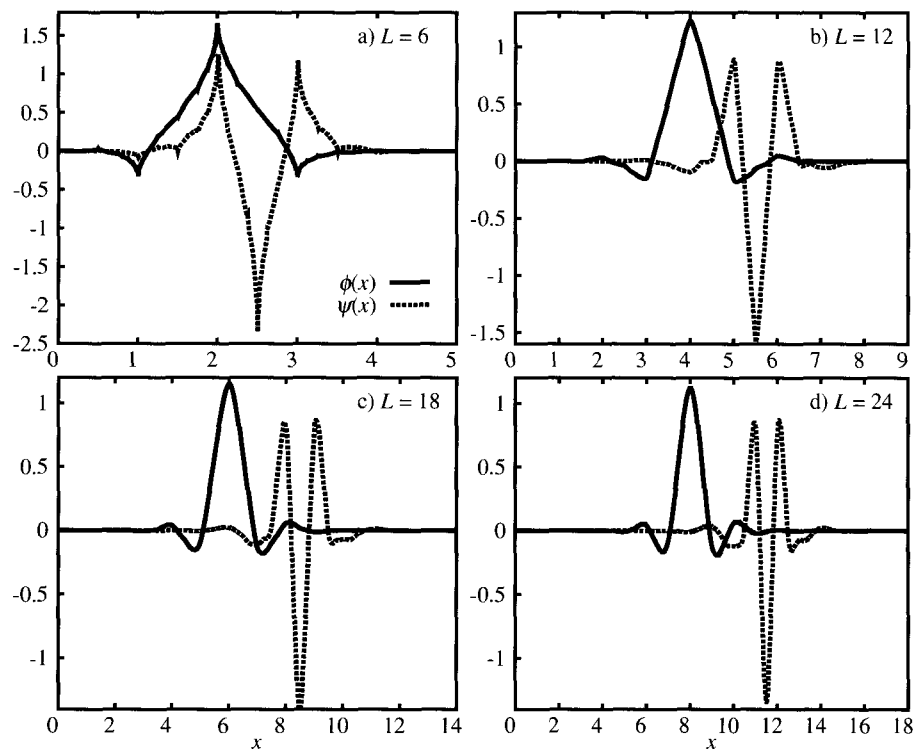


Figure 2.6: Scaling functions  $\phi(x)$  and corresponding wavelet functions  $\psi(x)$  for Daubechies compact support coiflet families of different lengths  $L$  listed in Table 2.2. Some plots are presented on a reduced  $x$ -range for clarity, the full nonzero support of each function is  $[0, L - 1]$ .

for higher  $N$  is longer function length for comparable approximation orders  $M$ . The Hölder exponent  $\alpha$  introduced as an index of worst-case local smoothness for the

scaling functions is also seen here to grow systematically with  $L$ , but not as quickly

Table 2.2: Moment orders, first moments, and Hölder exponents for coiflet scaling functions [6] shifted to start at  $x = 0$ . These integer-shifted coiflets have even order  $M$ , length  $L = 3M$ , and  $N = M + 1 = L/3 + 1$  [7].

Daubechies coiflet scaling functions				
$L$	$M$	$N$	$m_1$	$\alpha$
6	2	3	2	0.5424
12	4	5	4	1.3891
18	6	7	6	2.2083
24	8	9	8	2.8713

as for Daubechies wavelets (see Table 2.1). From the other point of view, for a given  $L$ ,  $M = L/3$  is smaller for coiflet systems in order to accommodate the increased  $N$ . Gopinath and Burrus [8] show that the Daubechies wavelet families of Section 2.3 automatically satisfy  $m_2 = m_1^2$  and always have  $N = 3$ . By comparison, coiflet families with the same  $L$  allow  $M$  to shrink in order to increase  $N$  (as shown later in Table 3.1). Their approximation orders are no longer fixed with respect to length as in the Daubechies case.

Daubechies' original construction of coiflets [2, 6] were designed with vanishing wavelet moments and vanishing scaling function moments,  $\int \phi(x) x^p dx = \delta_{p0}$  for  $0 \leq p \leq N - 1$ . These vanishing moments require integer shifting of the coiflet scaling function by an amount  $-m_s$ , resulting in a function with support  $[-m_s, L - 1 - m_s]$ . An alternative, but equivalent, point of view used in this work constructs coiflet scaling functions with vanishing *shifted* scaling function moments [see Eq. (2.39)]. This leads to coiflets with support  $[0, L - 1]$  and first moment  $m_1 = m_s$ . This means that in the special case where  $m_1$  is an integer, one may shift the support by  $-m_1$  to

obtain  $N - 1$  vanishing moments. Daubechies original coiflets can also be regarded as *integer-shifted generalized coiflets*. They are special cases of generalized coiflets, the latter identified by real-valued  $m_1$ .

## 2.6 Evaluation of Scaling Function Expansion Coefficients

To fully reconstruct  $f$ , expansion coefficients  $f_{jk}^\lambda$  and basis function values  $\phi_{jk}^\lambda(x)$  are required. While not known as an analytic function, the  $\phi_{jk}^\lambda(x)$  values can be calculated as accurately as needed as discussed in Section 2.3. With nothing more than changes of integration variable and use of binomial expansions, the exact projection integrals for polynomial functions can now be evaluated. What remains, then, is the calculation of the expansion coefficients of general functions  $f(x)$ .

The pyramid algorithm was introduced in Section 2.2.1 as an efficient method for calculation of multiscale wavelet projection integrals of Eq. (2.16) from single-scale scaling function projection integrals of Eq. (2.15). Therefore attention focuses on the calculation of scaling function projections on single scales, for which a simple method is discussed next.

### 2.6.1 Single-Point Projection Integral Evaluation

Due to its compact support and unit area for any of the above families, the scaling function  $\phi(x)$  bears some resemblance to a Dirac delta function. On finer scales  $\lambda$  the area is modified, but the principle is still the same. In applying his multiresolution wavelet algorithm directly to signal data, Stéphane Mallat [4] implicitly used the

interpretation that scaling function projections are approximately proportional to function samples, which can be expressed as

$$f_{jk}^\lambda \propto f(k\lambda/2^j) . \quad (2.42)$$

This simple prescription is the basis for much of the wavelet-based signal and image processing literature of the last couple decades. Strang and Nguyen, however, refer to this approximation as a “wavelet crime” since projections are integrals and not simple point samples.

Gopinath and Burrus [8] improved upon this approximation for Daubechies scaling functions using the fact that  $m_2 = m_1^2$ . This a relation between scaling function moments from Eq. (2.35). If a sample point at the mean position of the scaling function is used, then

$$f_{jk}^\lambda = \lambda_j^{1/2} f([k + m_1]\lambda_j) + \mathcal{O}(\lambda_j^{3+1/2}) . \quad (2.43)$$

This compares favorably to the previous sampling, for which the error exponent would be  $1 + 1/2$ . The level  $j$  does not need to be increased nearly as much to achieve the same absolute accuracy. For coiflet families, introduced in the last section, one can obtain even higher-order accuracy,

$$f_{jk}^\lambda = \lambda_j^{1/2} f([k + m_1]\lambda_j) + \mathcal{O}(\lambda_j^{N+1/2}) , \quad (2.44)$$

with the short-hand from Eq. (2.9),  $\lambda_j = \lambda/2^j$ . This expression is derived by a change

of variable and substitution of the Taylor expansion of  $f(x)$  about the point  $\lambda_j(m_1+k)$ . The calculation of scaling function moments was covered in Section 2.4. This is an important reason why researchers [9, 10, 11, 12] have used coiflets (or biorthogonal bases) in applications, for they possess higher  $N$  values compared to Daubechies wavelet families. Coiflets, then, allow simple, efficient, and accurate evaluation of projection coefficients.

This section is closed with a discussion of a method for the calculation of expansion coefficients that is independent of both the value of  $N$  and of the specific function samples used.

### 2.6.2 Multi-Point Projection Integral Evaluation

The path taken in the development of wavelet quadrature [13] considers simplification of projection integrals through a local polynomial representation of  $f$

$$f(x) \approx \sum_{q=0}^{r-1} f(x_q) L_{rq}(x) . \quad (2.45)$$

The  $x_q$  are quadrature nodes and the  $L_{rq}(x)$  are Lagrange polynomials

$$L_{rq}(x) = \prod_{\substack{q'=0 \\ q' \neq q}}^{r-1} \frac{x - x_{q'}}{x_q - x_{q'}} \quad (2.46)$$

of maximum order  $r - 1$ . The Lagrange interpolating form gives exact values of  $f$  at the quadrature nodes and has low-order polynomial behavior in between. Substitution of this interpolating form of  $f$  in the projection integral definition gives an  $r$ -point

quadrature formula in terms of quadrature weights  $\omega_q$  and function samples,

$$f_{jk}^\lambda = \lambda_j^{1/2} \sum_{q=0}^{r-1} \omega_q f(\lambda_j [k + x_q]) + \mathcal{O}(\lambda_j^{r+1/2}) . \quad (2.47)$$

The quadrature nodes  $x_q$  are relative sample positions such as  $x_q = 0, 1, 2, \dots, r-1$  and the quadrature weights are those originally calculated in the case  $\lambda = 1$  and  $j = 0$ ,

$$\omega_q = \sum_{p=0}^{r-1} \frac{L_{rq}^{(p)}(0)}{p!} m_p . \quad (2.48)$$

These scale-independent weights are simple expressions in terms of scaling function moments and derivatives of Lagrange polynomials (the Taylor expansion is exact in this case). The only  $\lambda_j$  dependence comes in the normalizing prefactor and in the positions of the samples of  $f$ .

The  $\omega_q$  can be re-used (for every  $k$ ) even if there is non-uniform spacing in the  $x_q$ . It is only in the situation when the  $x_q$  are changed from one value of  $k$  to the next that new  $\omega_q$  need to be calculated. The moments  $m_p$  pose no difficulties as they only need to be calculated once and for all, see Section 2.4.

Multi-point wavelet quadrature is still applicable in situations such as discrete data sets if it is inconvenient to shift alignment by  $m_1$ . In this (or any) case, the wavelet quadrature developed in our lab can match or beat the  $\mathcal{O}(\lambda_j^{N+1/2})$  error of the single point sample method, irrespective of the basis value of  $N$  (or  $L$ ) or of the specific function sample locations. With the multi-point wavelet quadrature, one can

also show that, for example, taking  $x_q = q + m_1$  in Eq. (2.47) produces only a single nonzero  $\omega_q$  and its value is unity, thus making the connection between single-point and wavelet quadrature. However, in the wavelet quadrature method one can take more than  $N$  quadrature points, chosen as is convenient, and obtain greater accuracy than can be obtained by using a single point. In practice, this extra accuracy is especially valuable for bases with low  $N$ .

## 2.7 Scaling Function Matrix Elements

The idea behind wavelet quadrature carries over to general function matrix elements  $f_{lk}^\lambda = \langle \phi_{jl}^\lambda | f | \phi_{jk}^\lambda \rangle$ , integrals important in quantum mechanical applications. Solution of the vibrational Schrödinger equation requires calculation of potential matrix elements. These potential matrix elements are bilinear integrals of the form

$$f_{lk}^\lambda = \langle \phi_{jl}^\lambda | f | \phi_{jk}^\lambda \rangle = \int \phi_{jl}^\lambda(x) f(x) \phi_{jk}^\lambda(x) dx \quad (2.49)$$

and are evaluated by numerical quadrature of the form

$$f_{lk} = \lambda^{1/2} \sum_{q=0}^{r-1} \Omega_{qk} f(\lambda[l + x_q]) + \mathcal{O}(\lambda^{r+1/2}) . \quad (2.50)$$

The idea is to again approximate  $f$  with its Lagrange interpolating polynomial form and integrate the resulting polynomials over the scaling function basis members,



with this approach the matrix quadrature weights are found as

$$\Omega_{qk} = \sum_{p=0}^{r-1} \frac{L_{rq}^{(p)}(0)}{p!} M_{pk} . \quad (2.51)$$

The Lagrange interpolating polynomials  $L_{rq}(x)$  were defined in Eq. (2.46) and the *matrix moments* are the bilinear form of scaling function moments,

$$M_{pk} = \int \phi(x) x^p \phi_k(x) dx . \quad (2.52)$$

Eq. (2.50) should be compared to Eq. (2.47).

## 2.8 Difficulties with the Matrix Representation

The 1D scaling function matrix elements  $f_{lk}^\lambda = \langle \phi_{jl}^\lambda | f | \phi_{jk}^\lambda \rangle$  of the last section, as written, present no difficulties. Multiplicative operators in quantum mechanical problems, in particular, present a significant storage problem in higher dimensions. In the vibrational quantum problems discussed below, matrix elements of multidimensional potential (multiplicative) operators of  $d$  degrees of freedom,  $\hat{V} = V(x_1, x_2, \dots, x_d)$ ,

$$V_{lk}^\lambda = \langle \phi_{jl_1}^\lambda \phi_{jl_2}^\lambda \cdots \phi_{jl_d}^\lambda | \hat{V} | \phi_{jk_1}^\lambda \phi_{jk_2}^\lambda \cdots \phi_{jk_d}^\lambda \rangle , \quad (2.53)$$

must be calculated. These are multidimensional integrals involving direct-product wavelet bases. With separable (sum and/or product separable) multidimensional PESs the problem is simplified to a series of 1D matrix elements. Unfortunately, real

molecular potentials are often highly coupled functions of nuclear coordinates. This presents difficulties for application of the matrix element quadrature from the last section because the multidimensional matrix must be stored, requiring (with  $N_b$  basis functions in each 1D coordinate)  $N_b^{2d}$  memory locations. In 3D, for example, full matrix storage is  $N_b^6$ . In this case the row and column indices,  $l$  and  $k$ , respectively, are each composite indices of the all the 1D matrix indices, an example of the latter being shown in Eq. (2.49). Even with sparse storage (only nonzero matrix elements) the memory footprint of the multidimensional matrix quickly exceeds fast storage of typical computers as shown in the 3D example of Fig. 2.7. Storage of the full

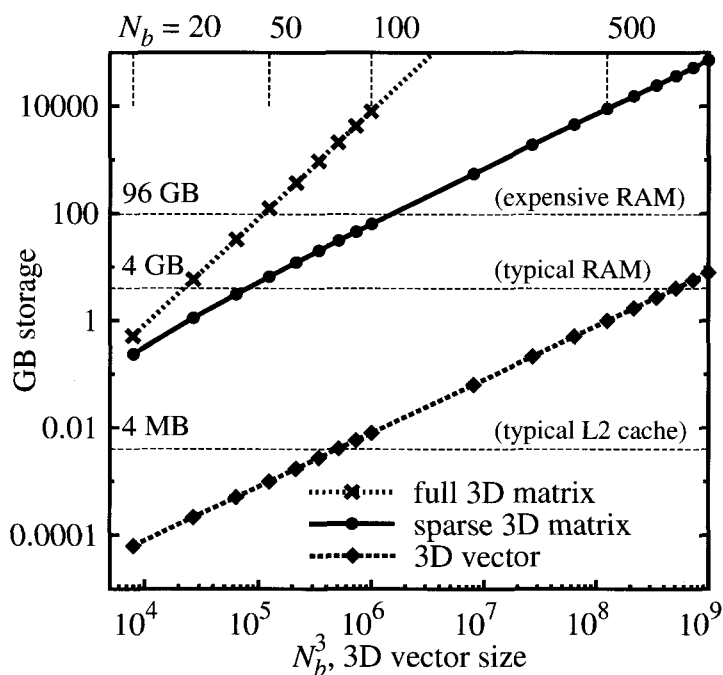


Figure 2.7: Representative potential storage requirements for different 3D direct product bases each of length  $L = 12$ . Shown on a log-log plot are the full 3D vector of size  $N_b^3$  (bottom trace) and the full 3D matrix of size  $N_b^6$  (top trace). The sparse storage falls in between (middle trace).

3D direct-product matrix is indeed seen to be out of reach for most single-processor computers. The sparse storage afforded by wavelet bases allows more functions to be

used but also succumbs to the same fate due to a large prefactor. The 3D vector, on the other hand, is representable still, even for exceedingly large  $N_b$ .

Beyond single-scale storage issues, there are other difficulties found in multiscale wavelet representations of operators. Matrices in these multiscale bases are obtained in the standard representation by using two-scale relations iteratively for both bra and ket basis functions. The resulting matrices are less sparse and become significantly more full as the number of included scales increases. As an alternative to keep the matrix-vector multiplications closer to scaling linearly with basis size, Beylkin, et al., introduced the non-standard representation where one retains some redundant submatrices involving intermediate scaling functions. However, neither standard nor non-standard representations appear to be discussed in depth anywhere in conjunction with compression. The coding for application of multidimensional multiscale matrices with dynamic (not known *a priori*) deletion of basis elements would indeed be formidable.

As mentioned, uncoupled (or separable) potential operators present no difficulties because a series of 1D matrix elements are stored, suppressing the exponential growth in storage associated with the coupled multidimensional case of realistic molecular potentials. In the next chapter, coupled multidimensional matrix elements are reduced to a single multidimensional vector to simplify these difficult cases.

## Chapter 3

# Matrix-Free Application of Hamiltonian Operators in Wavelet Bases

Our interests in wavelet-based differential equation solvers are rooted in vibrational spectroscopy and nanophotonics. The simulation of small-molecule spectra requires calculation of matrix elements of fully-coupled multidimensional molecular potential energy functions. In contrast, plasmon enhanced fields of metal nanostructures are found through applications of differential operators. In either case, the solution, whether if it is a vibrational eigenfunction or an electromagnetic (EM) field, is represented as already explained in Section 2.1.

For the approach taken here, wavelet-based solutions of quantum and EM equations require function and operator representations. Both differential (kinetic) and multiplicative (potential) operators are necessary for the quantum case, while the differential representation is all that is necessary in the EM case for sourceless isotropic media.

The most recent work, and the focus here, is the elimination of operator matrices in wavelet bases. For molecular quantum eigenvalue and dynamics calculations in multiple dimensions, it is the coupled potential energy matrices that generally

dominate storage requirements. A Coefficient Product Approximation (CPA) for the potential operator and wave function expansions in a scaling function basis dispenses with the matrix, reducing storage and coding complexity. New developments are required, however. It is determined that the CPA is most accurate for specific choices of wavelet families and these are given here. They have relatively low approximation order (number of vanishing wavelet function moments), which would ordinarily be thought to compromise both wavelet reconstruction and differentiation accuracy. Higher-order convolutional coefficient filters are determined that overcome both apparent problems. Each of these require a number of multiplication steps per expansion coefficient that can be tuned for accuracy. The result is a practical wavelet method where the effect of applying the Hamiltonian matrix to a coefficient vector can be calculated accurately without constructing the matrix.

The development of this matrix-free approach has been driven by the need for efficiency in the quantum case with general potentials. The focus here is on eigenvalue equations, but out of this work there are advantages that can be directly exploited in the area of quantum dynamics, for example, in future work on the Conjugate Symmetric Lanczos propagation method introduced in Section 5.2. It is also expected that the tuneable-accuracy filter developments can be of advantage for EM problems in either frequency- or time-domains, even though the CPA is not needed for sourceless problems. From recent more general EM applications by Pan [9, 10, 11, 12], however, we expect that the bases constructed here for use of the CPA will also have advantages there.

The vibrational time independent Schrödinger equation (TISE)

$$\hat{H} y = E y = (\hat{T} + \hat{V}) y \quad (3.1)$$

is a linear, second-order differential equation in the variables  $\mathbf{x} = (x_1, \dots, x_d)$ . The vibrational Hamiltonian is  $\hat{H}(\mathbf{x})$ , the nuclear wave function is  $y(\mathbf{x})$ , and  $E$  is the energy. The explicit dependence on  $\mathbf{x}$  in  $\hat{H}$  and  $y$  is suppressed for simplicity. The Hamiltonian is composed of the kinetic energy  $\hat{T}$  and the potential energy  $\hat{V}$ .

In a Cartesian coordinate system the Hamiltonian is written

$$\hat{H} = \hat{T} + \hat{V} = - \sum_{j=1}^d \frac{\hbar^2}{2m_j} \frac{\partial^2}{\partial x_j^2} + V(\mathbf{x}) . \quad (3.2)$$

The defining characteristics of particular systems lies in the details of the potential energy and in the masses in the kinetic energy term. In 1D, the potential depends on a single variable  $x$  and the kinetic energy has a single term,  $\hat{H} = -\frac{\hbar^2}{2m} \frac{d^2}{dx^2} + V(x)$ . The allowed vibrational energy levels can be calculated in a scaling function basis by forming the Hamiltonian matrix  $\mathbf{H}$ , with matrix elements

$$H_{lk} = \langle \phi_{jl}^\lambda | \hat{H} | \phi_{jk}^\lambda \rangle = \int \phi_{jl}^\lambda(x) \hat{H}(x) \phi_{jk}^\lambda(x) dx . \quad (3.3)$$

This requires the calculation of both kinetic and potential matrices

$$T_{lk} = \langle \phi_{jl}^\lambda | \hat{T} | \phi_{jk}^\lambda \rangle = \int \phi_{jl}^\lambda(x) \hat{T}(x) \phi_{jk}^\lambda(x) dx \quad (3.4)$$

$$V_{lk} = \langle \phi_{jl}^\lambda | \hat{V} | \phi_{jk}^\lambda \rangle = \int \phi_{jl}^\lambda(x) \hat{V}(x) \phi_{jk}^\lambda(x) dx . \quad (3.5)$$

The kinetic energy matrix elements are exactly calculable through solution of a small system of algebraic equations and the potential matrix elements can be determined accurately with the wavelet matrix quadrature of Section 2.7. In the multidimensional case the calculation of the potential energy contributions generally dominate the computational burden of constructing the Hamiltonian matrix. This is especially true when the potential is nonseparable since the potential matrix elements given in Eq. (2.53) then do not factor and one is forced to perform multiple integrals.

Stationary vibrational eigenfunctions are computed through use of an eigensolver. This diagonalization, in a direct form, requires the explicit storage and manipulation of *all* the  $H_{lk}$  elements (or all nonzero elements for sparse direct methods). Another class of eigensolvers, better suited to large sparse structured matrices, only requires the *result* of a matrix vector product

$$z_{jl}^\lambda = \sum_k H_{lk} y_{jk}^\lambda . \quad (3.6)$$

In conventional wavelet calculations, one constructs the Hamiltonian matrix in sparse form and then multiplies it into the vector of coefficients. The same procedure is used in the general Wavelet-Galerkin method [14, 15] applied in fluid mechanics and other areas. However, as discussed in the previous chapter and especially for multidimensional problems, it would be preferable if one could calculate the result of the matrix-vector product without actually constructing the Hamiltonian matrix. For the

kinetic energy operator, this can be accomplished as a convolution operation using small-length filters. For the potential energy operator, there is still needed a means of avoiding the construction of the corresponding matrix. We have developed a new method to circumvent the use of potential matrices altogether.

### 3.1 Coefficient Product Approximation for Potential Operators

The problem until now has been failure to exploit a simple fact, namely that for sufficiently fine scales the expansion coefficients for a range of  $k$  tend to follow the shape of the function itself. If one expands  $V(x)$  like in Eq. (2.15) but with coefficients  $V_{jk}^\lambda$ , the sequence of products  $V_{jk}^\lambda y_{jk}^\lambda$  should similarly follow the shape of the product function  $V(x)y(x)$ . The expansion coefficients of the latter are to a certain approximation simply proportional to  $V_{jk}^\lambda y_{jk}^\lambda$ . This represents a potential storage advantage, especially in multidimensional problems.

Instead of the matrix-vector product the CPA calculates the action of the potential as a pairwise product of expansion coefficients

$$z_{jk}^\lambda = \lambda_j^{-1/2} V_{jk}^\lambda y_{jk}^\lambda + \mathcal{O}(\lambda_j^{N+1/2}) . \quad (3.7)$$

Matrix elements are not needed, only a vector of projection integrals,  $V_{jk}^\lambda$ .

To justify the CPA first consider the scaling function representations of the func-



tions  $V$  and  $y$

$$V(x) \approx \sum_k V_{jk}^\lambda \phi_{jk}^\lambda(x) \quad (3.8)$$

$$y(x) \approx \sum_k y_{jk}^\lambda \phi_{jk}^\lambda(x) , \quad (3.9)$$

as previously considered for a different function  $f$  in Eq. (2.15) and examine the expansion coefficients  $V_{jk}^\lambda = \langle \phi_{jk}^\lambda | V \rangle$  and  $y_{jk}^\lambda = \langle \phi_{jk}^\lambda | y \rangle$ . Through use of Eq. (2.8) and substitution of  $V(x)$  by its Taylor expansion about the point  $k\lambda_j$ , the expansion coefficients can be written

$$V_{jk}^\lambda = \sum_{p=0}^{\infty} \frac{1}{p!} V^{(p)}(k\lambda_j) \int \lambda_j^{-1/2} \phi\left(\frac{x}{\lambda_j} - k\right) (x - k\lambda_j)^p dx \quad (3.10)$$

$$= \sum_{p=0}^{\infty} \frac{1}{p!} V^{(p)}(k\lambda_j) \lambda_j^{1/2} \int \phi(x) (\lambda_j x)^p dx \quad (3.11)$$

$$= \sum_{p=0}^{\infty} \frac{1}{p!} V^{(p)}(k\lambda_j) \lambda_j^{p+1/2} m_p . \quad (3.12)$$

The same process on  $y(x)$  gives

$$y_{jk}^\lambda = \sum_{p=0}^{\infty} \frac{1}{p!} y^{(p)}(k\lambda_j) \lambda_j^{p+1/2} m_p . \quad (3.13)$$

A similar analysis with  $z(x) = V(x) y(x)$  gives

$$\begin{aligned}
 z_{jk}^\lambda &= \int \phi_{jk}^\lambda(x) V(x) y(x) dx \\
 &= \sum_{p=0}^{\infty} \sum_{q=0}^{\infty} \frac{1}{p! q!} V^{(p)}(k\lambda_j) y^{(q)}(k\lambda_j) \int \lambda_j^{-1/2} \phi\left(\frac{x}{\lambda_j} - k\right) (x - k\lambda_j)^{p+q} dx \\
 &= \sum_{p=0}^{\infty} \sum_{q=0}^{\infty} \frac{1}{p! q!} V^{(p)}(k\lambda_j) y^{(q)}(k\lambda_j) \lambda_j^{p+q+1/2} m_{p+q} .
 \end{aligned} \tag{3.14}$$

All of the orthogonal compact support wavelets have scaling moments obeying  $m_2 = m_1^2$ , and generalized coiflets expand this pattern so that  $m_p = m_1^p$  for larger values of  $p = 0, 1, \dots, N - 1$ . Through these orders,  $m_{p+q} = m_p m_q$ , and the coefficients of the product function approximately factorize,

$$z_{jk}^\lambda \approx \sqrt{\lambda_j} \left( \sum_{p=0}^{\infty} \frac{1}{p!} V^{(p)}(k\lambda_j) \lambda_j^p m_p \right) \left( \sum_{q=0}^{\infty} \frac{1}{q!} y^{(q)}(k\lambda_j) \lambda_j^q m_q \right) . \tag{3.15}$$

From Eqs. (3.12), (3.13) and (3.14) we obtain the CPA result with appropriate error term given in Eq. (3.7).

The quality of the CPA is actually rather low-grade for the original Daubechies wavelets [2] (with  $N = 3$ ), requiring unreasonably small values of  $\lambda$  and/or large values of  $j$ . Investigation shows that the CPA is improved for coiflets derived by Daubechies [2, 6], and the subsequently-developed generalized coiflets [7, 16, 17, 18].

This simple product approximation for the coefficients represents a significant reduction in storage, computational, and coding requirements compared to use of the earlier methods. One needs only the two coefficient vectors of  $V$  and  $y$ . These single multidimensional vectors afford orders of magnitude less storage, see the 3D case in

Fig. 2.7. It is especially to be observed that the error in the CPA is governed by the order to which moments of the scaling functions obey a simple power-law behavior. We are thus led in the next section to pursue maximization of  $N$  (for a given length  $L$ ) as the means to optimize the CPA.

A special case occurs if  $V$  and  $y$  are low-order polynomials since the error terms then disappear exactly (cf., Eq. (1.3) of Monzón, et al. [18]). More generally, it is nontrivial that one can systematically multiply projection coefficients in this manner since the basis functions have finite width. In essence, one mimics the ability of grid discretization or DVR methods to perform function multiplication in a point-wise fashion. It should also be mentioned that similar properties will be shared by biorthogonal cardinal interpolating wavelet bases such as interpolets [19] and recent variants [20], as well as biorthogonal coiflet bases [21, 22], but the present work focuses on orthogonal bases and thereby avoids the need to solve generalized eigenvalue problems.

### 3.2 Optimized Max- $N$ Generalized Coiflets

In order to minimize CPA error we pursue wavelet bases with a maximum number of vanishing shifted scaling function moments (equivalently, a maximum number of moments satisfying a power-law condition) at the expense of less vanishing wavelet moments  $M$  (approximation order). These new generalized coiflets are thus characterized by  $M < N$ .

A single-scale expansion of  $y(x)$  at scale  $\lambda_j$  is generally approximate, reflecting (i)

that the coefficients  $y_{jk}^\lambda$  may be inaccurate and/or (ii) that  $y(x)$  may have variations that cannot be completely captured at the resolution  $\lambda_j$ . If the expansion coefficients are numerically exact, the expansion (reconstruction) has at best  $\mathcal{O}(\lambda_j^M)$  error. CPA coefficients, as discussed above, have  $\mathcal{O}(\lambda_j^N)$  error provided that the individual coefficients are at least as accurate. Generalized coiflets are ordinarily chosen with  $N \approx M$ , for which the sources of error in Eq. (3.9) are balanced. For the same  $M$ , however, this leads to larger  $L$ , or less tight localization, compared to Daubechies wavelet families (see Table 3.1). If we want to increase  $N$  considerably above  $M$ , we need to calculate new members of the generalized coiflet families.

Table 3.1: Numbers of moment conditions satisfied by different compact-support orthogonal wavelet families.

	$M$	$N$
Daubechies/Symmlet	$L/2$	3
Coiflet	$L/3$	$L/3 + 1$
MGC	$[(L + 2)/4] = [(N + 1)/2]$	$L/2$
OMGC	$[(L + 4)/4]$	$(L + 2)/2$

It may be objected that allowing lower  $M$  makes higher-order accuracy of the coefficients worthless. The reconstruction accuracy is then  $\mathcal{O}(\lambda_j^M)$ , which can become unacceptably low. This perception has been changed recently by Neelov and Goedecker [23], who show for Daubechies wavelets that a particular finite convolution of the coefficients  $\sum_{i=0}^{L-1} \omega_i y_{j,k+i}^\lambda$  produces reconstruction of  $y(x)$  at particular sample points  $k'\lambda_j$  with a much smaller error that is  $\mathcal{O}(\lambda_j^L)$ . The collection of constants  $\omega_i$  serves as a convolution filter that is able to “beat the approximation order” in reconstruction. These filter reconstruction developments are discussed later in Sec-

tion 3.4. This insight has led us to generalize the reconstruction filters to arbitrary lengths/orders and to continuous interpolation with respect to reconstruction points. These filters apply equally well to all Daubechies-like families, including the case of the maximum- $N$  generalized coiflets (MGCs). Since the latter are unbalanced with respect to  $M$  and  $N$ , they are less familiar and are therefore described below along with an extension called optimized maximum- $N$  generalized coiflets (OMGCs).

Turning to the MGCs for general non-integral choices of  $m_1$  allowing solutions with real coefficients, we find that the maximum value of  $N$  is  $L/2$ , as shown in Table 3.1. The minimum value of  $M$  is not constant, but also varies with  $L$ . Monzón, et al. [18], explicitly prove that residual dependencies between the  $\phi$  and  $\psi$  equations for  $c_k$  will always guarantee that there are at least  $M = \lfloor \frac{L+2}{4} \rfloor$  vanishing wavelet moments. Thus it is possible to favor  $N$ , but not exclusively.

As in the work by Monzón, et al. [18], targeting  $N$  and  $M$  more nearly equal, one can home in continuously on specific values of  $m_1$  that produce one extra vanishing shifted scaling function moment, increasing  $N$  by 1. In these cases we find  $M$  is either unchanged or increases by 1, depending on the value of  $L$ . We call these cases *optimized* MGCs (or OMGCs) to indicate that  $N$  has been maximized as completely as possible for a given  $L$ . OMGCs are characterized by  $N = \frac{L+2}{2}$  and  $M = \lfloor \frac{L+4}{4} \rfloor$ . Focus is placed on OMGCs in the work below since these families give the highest accuracy for both the CPA and single-point quadrature.

Table 3.2 provides the values of  $m_1$  and  $\alpha$  for all of the OMGCs we were able to determine between  $L = 6$  and  $L = 20$ . The Hölder exponents (the measure of local smoothness) are smaller than those for the Daubechies wavelets of the same

Table 3.2: Moment orders, first moments, and Hölder exponents for OMGC scaling functions shifted to start at  $x = 0$ . Number of moment conditions obeyed by and first moments of OMGCs. Other OMGCs, not shown, correspond to reflection around the midpoints.

OMGC scaling functions						
$L$	Label	$M$	$N$	$m_1$	$\alpha$	
6		2	4	2.105 967 800 055 620 6	0.5514	
8	a	3	5	2.239 549 738 364 677 7	1.0257	
	b	3	5	2.977 273 091 796 802 3	1.1004	
10		3	6	3.755 017 927 314 149 9	1.0516	
12	a	4	7	3.867 449 072 798 277 5	1.4399	
	b	4	7	5.284 552 550 893 758 5	1.6286	
14	a	4	8	5.428 073 816 691 219 6	1.5196	
	b	4	8	6.101 403 965 841 333 7	1.4659	
16	a	5	9	5.513 471 648 490 571 8	1.8200	
	b	5	9	6.204 901 221 550 508 3	1.8538	
	c	5	9	6.965 727 285 834 369 0	1.9526	
	d	5	9	7.426 339 183 865 327 4	2.1311	
18	a	5	10	7.117 162 501 237 350 2	1.9674	
	b	5	10	8.418 764 663 532 745 4	1.8579	
20	a	6	11	7.174 163 648 854 884 6	2.1799	
	b	6	11	8.513 700 459 888 850 3	2.2514	
	c	6	11	8.658 260 217 193 909 6	2.2696	
	d	6	11	9.149 297 747 742 840 8	2.4085	

length  $L$ , though this will not be an issue for our calculations. These scaling and wavelet functions are given in Figs. 3.1, 3.2, and 3.3. It is seen that the OMGCs are all relatively smooth, which is definitely not the case for MGCs at all values of  $m_1$ .

The examples for  $L = 8$  coincide with the optimized results found by Monzón, et al.[18] for nearly balanced  $M$  and  $N$ , while our results for higher  $L$  are presumed new. All OMGC  $c_k$  coefficients are tabulated in Appendix A. Their first moments  $m_1$  were already presented in Table 3.2.

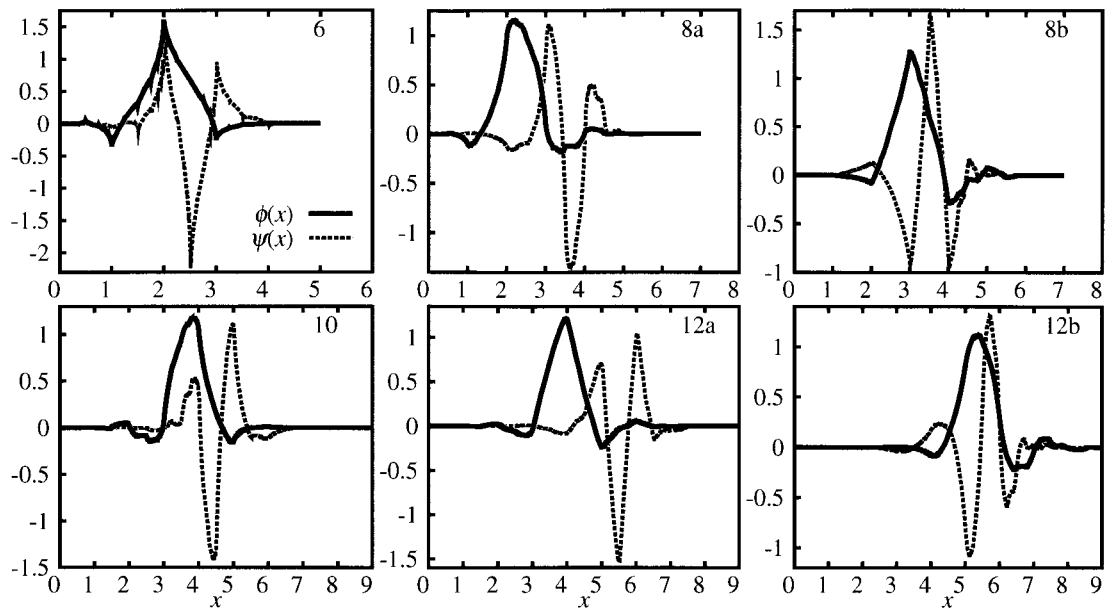


Figure 3.1: Scaling functions  $\phi(x)$  and corresponding wavelet functions  $\psi(x)$  for OMGCs of different lengths  $L = 6$ – $12$  listed in Table 3.2.

### 3.2.1 Coefficient Product Approximation Test

As a first test of the CPA we examine the action of a Morse potential  $V(x)$  on a Gaussian function  $y(x)$

$$V(x) = 100 (1 - \exp[-\frac{3}{2}(x - 3)])^2 \quad (3.16)$$

$$y(x) = \exp[-10(x - 3)^2]. \quad (3.17)$$

The steeply-rising wall of the Morse potential for smaller  $x$  dominates the product  $V y$ , as shown in Fig. 3.4. Scaling function representations  $\phi_{jk}^\lambda(x)$  are assumed. These functions are spaced by  $\lambda_j$ . We take  $\lambda = 1/4$  and consider different  $j = 0, 1, 2, \dots$ , corresponding to the different-resolution nested subspaces  $\mathcal{V}_j$ . Each subspace is truncated to a range  $k_{\min,j} \leq k \leq k_{\max,j}$  chosen so as to cover the range where the product

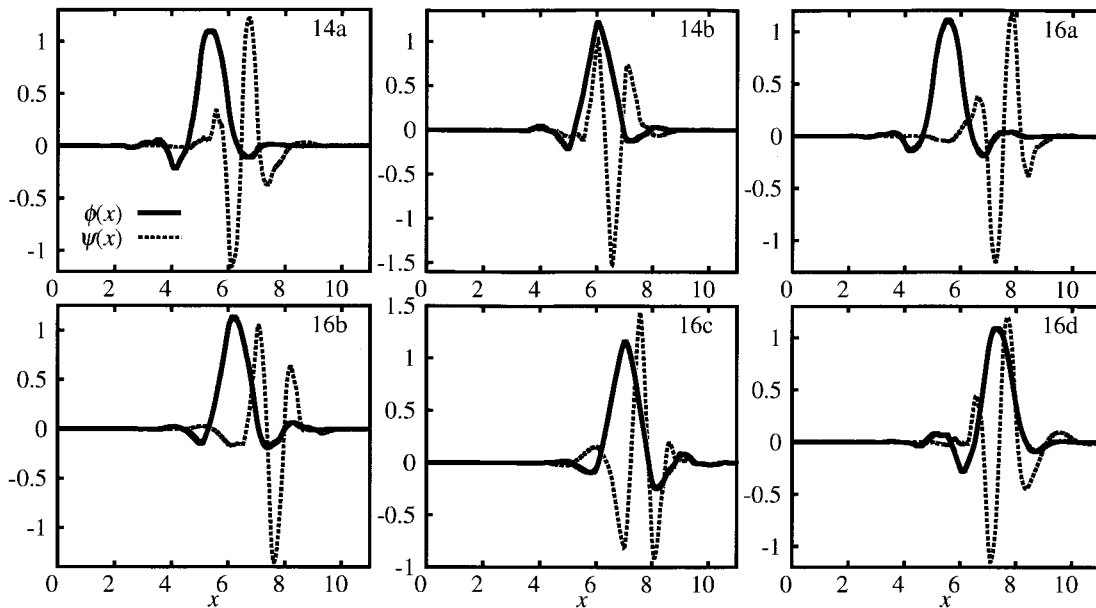


Figure 3.2: Scaling functions  $\phi(x)$  and corresponding wavelet functions  $\psi(x)$  for OMGCs of different lengths  $L = 14$ – $16$  listed in Table 3.2.

function is significant.

Scaling function expansions are constructed of  $V$  and  $y$  in Eqs. (3.8) and (3.9). The projection integrals  $V_{jk}^\lambda$  and  $y_{jk}^\lambda$  can be accurately evaluated by the wavelet quadrature [13] methods of Eq. (2.47). The single-point method of Eq. (2.44) is also available.

The only ingredient needed for the single-point quadrature formula is the accurate value of  $m_1$  (included in Tables 2.1, 2.2 and 3.2). Both this formula and the accuracy order of the CPA derive from the same power-law behavior of the moments, but in practice the CPA does not require the value of  $m_1$  for its implementation. That is, there is no issue about special alignment of the basis required in order to use the CPA.

One can control the absolute accuracy of the expansion coefficients by using refinement as in Section 2.2.2. We have refined projection coefficients for  $V(x)$ ,  $y(x)$  and  $V(x)y(x)$  in order to numerically verify the error behavior of the basic CPA itself.



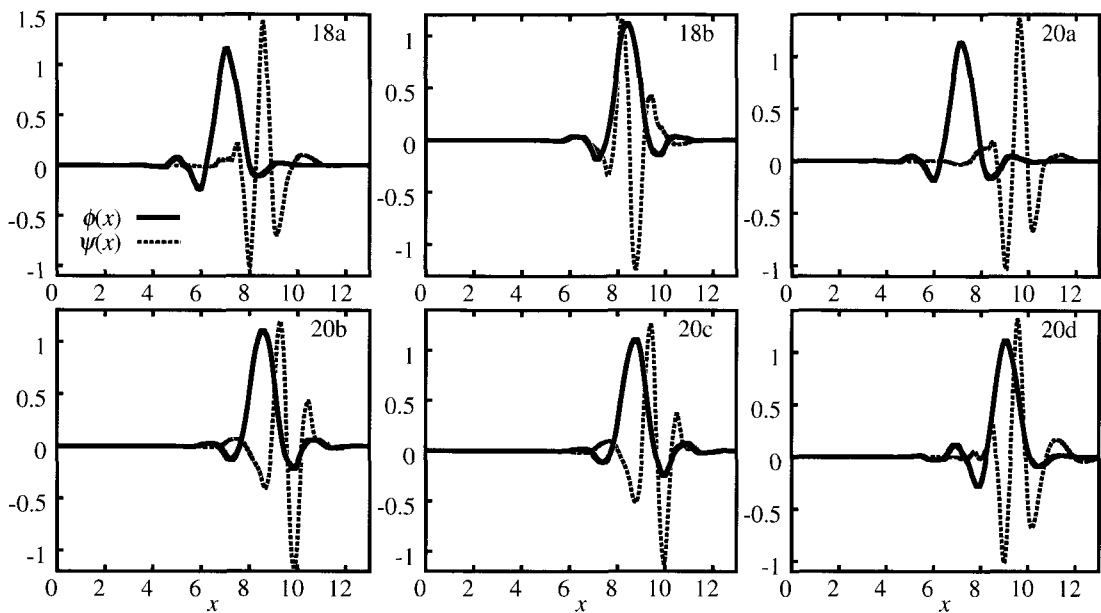


Figure 3.3: Scaling functions  $\phi(x)$  and corresponding wavelet functions  $\psi(x)$  for OMGCs of different lengths  $L = 18\text{--}20$  listed in Table 3.2.

The maximum absolute errors in CPA projection coefficients on scales  $\lambda_j$ , with  $\lambda = 1/4$ , for  $j = 0 - 8$  are shown in Fig. 3.5 for Daubechies, coiflet, and OMGC scaling function bases with the same  $L$ . It is clear that the CPA approximation is not very accurate for the Daubechies families, but is significantly better for coiflets and is definitely best for the OMGCs. The effects of finite precision using C++ code in

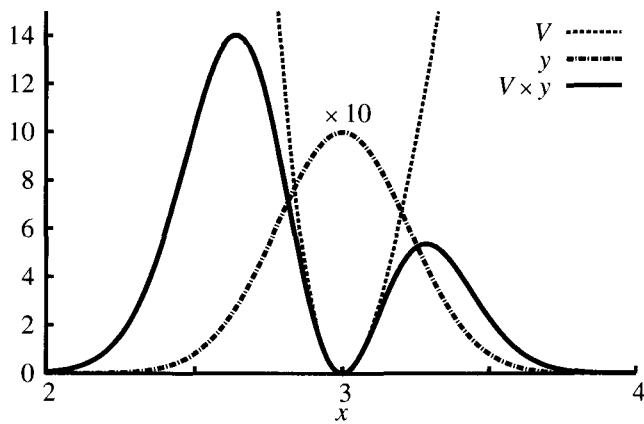


Figure 3.4: Morse potential applied to Gaussian function.

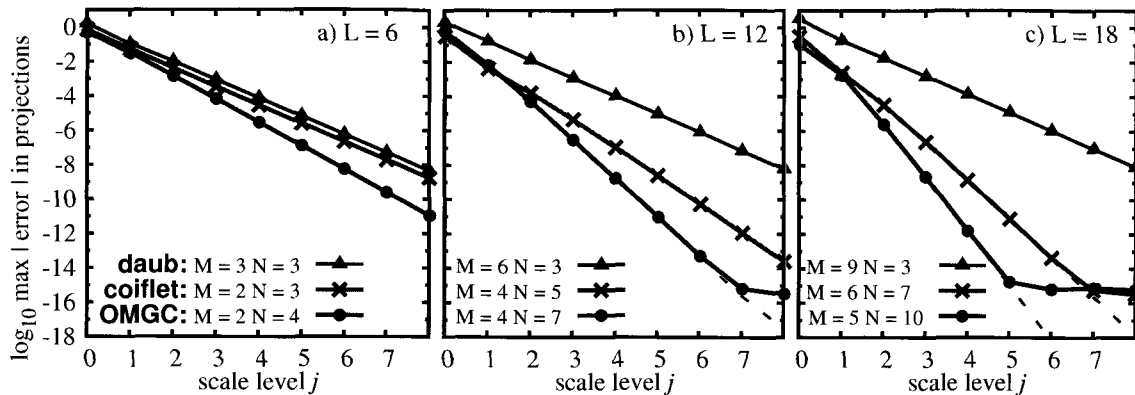


Figure 3.5: Maximum absolute errors in  $V(x)y(x)$  [Eqs. (3.16) and (3.17)] CPA projection coefficients calculated at different scales  $\lambda_j$  with  $\lambda = 1/4$  using Daubechies, Daubechies integer-shift coiflet, and OMGC scaling functions of lengths a)  $L = 6$ , b) 12, and c) 18. Basis functions covering the relevant range of  $x$  were used for each  $L$  and  $\lambda_j$  value. The  $\mathcal{O}(\lambda_j^{-L/2-1})$  behavior shown fully realizes the achievable order of error for the CPA for the OMGC family.

double precision ( $\sim 16$  decimal places) are shown in the plateau regions of the last two panels. The dashed lines represent calculations in Mathematica with higher precision.

Similar calculations have been performed using converged matrix elements of  $V$  in the matrix-vector method of multiplying functions. It is found for the OMGCs that essentially the same scaling behavior for the error is obtained using the CPA and matrix-vector methods, except that the latter is slightly better for every other value of  $L$  (8, 12, 16, ...). This is not enough of an improvement to justify the extra effort of constructing and using the potential matrix.

### 3.3 Finite-Difference Derivatives for Kinetic Operators

With the potential treatment simplified, it remains to examine the application of differential operators. The standard procedure Beylkin [24] uses for Daubechies scaling functions can be used for generalized coiflet bases as well to evaluate matrix

elements of the derivative operator. These act on function projections and produce projections of function derivatives. For example, on a unit scale, the first derivative matrix acts according to

$$\sum_{k'} D_{kk'}^{(1)} x_{k',p} = p x_{k,p-1} \quad (3.18)$$

where the  $x_{kp}$  are  $\phi_k$  projections of  $x^p$ . The matrix is banded with  $2L - 3$  bands, each element in a band being the same ( $D_{kk'}^{(1)}$  depends only on  $k' - k$ ). Explicit matrix construction and storage is therefore not necessary since one can simply save the  $2L - 3$  nonzero numbers in a row as a differential filter to be applied starting at different places along the sequence of coefficients. This saves only storage and not computational work, but there are further considerations.

While it might be thought that Eq. (3.18) holds only to  $p < M$  for which  $x^p$  is entirely in the scaling function subspace  $\mathcal{V}_0$ , it actually holds up to  $p = L = 2M$  for Daubechies wavelets, i.e., one has “superconvergence,” [25, 26] even though the higher-power monomials are not entirely contained in  $\mathcal{V}_0$ . The maximum order  $2M$  for which Daubechies-basis superconvergence holds is actually not very high considering the length  $2L - 3$  of the matrix-based filter. For the OMGCs, the maximum order is also found to be  $2M$ , but this is now much less than  $L$ . Optimizing  $N$  has reduced the maximum order of the matrix-based derivative filter for Eq. (3.18) even further.

A search was therefore undertaken for filters that satisfy Eq. (3.18) and its multiple-derivative analogs to higher  $p$  than the standard matrix-based filters. Despite initial expectations, the solutions turn out to be independent of the specific basis and to be

familiar finite difference (FD) formulae. The final result for a length- $n$   $i^{\text{th}}$ -derivative filter can be expressed as

$$D_{kk'}^{(i)} = \left[ \frac{d^i}{dx^i} L_{nk'}(x) \right]_{x=k} \quad (3.19)$$

in terms of derivatives of the Lagrange polynomials. For simplicity,  $n$  is taken as odd and the  $k'$  range is centered on  $k$ , yielding  $k$ -independent symmetric or antisymmetric filters depending on the number of derivatives  $i$ . For  $n = 3$  and  $i = 2$ , for example, this choice produces the well-known three-point FD stencil  $(1, -2, 1)$ . The fact that classical FD filters arise as the solution to the search should not be thought obvious since they are usually used for differencing on a real-space grid rather than for application to square-integrable basis functions.

We can analyze the order of error by returning to a  $\lambda$ -scaled basis. Using Taylor expansion within projection integrals, one can show that

$$\sum_{k'} D_{kk'}^{(i)} f_{k'}^\lambda = \lambda^i \int \frac{d^i f(x)}{dx^i} \phi_k^\lambda dx + \mathcal{O}(\lambda^{n+1/2}) . \quad (3.20)$$

Dividing through by  $\lambda^i$ , we see that the derivative projections at different  $k$  are obtained to formal order  $\mathcal{O}(\lambda^{n-i+1/2})$ . In the case of the second derivative, for example, the standard filter has error  $\mathcal{O}(\lambda^{2M-3/2})$ , as opposed to the FD error  $\mathcal{O}(\lambda^{n-3/2})$ , which can be tuned to control the accuracy order.

We will compare the matrix-based and FD differentiation filters numerically, focussing on the second derivative since this is important for the standard 1D quantum Hamiltonian. In a  $\lambda_j$ -scaled scaling function basis, the matrix elements  $T_{lk} =$

$\langle \phi_{jl}^\lambda | \hat{T} | \phi_{jk}^\lambda \rangle$  can be expressed by a change of integration variables as

$$T_{lk} = -\frac{\hbar^2}{2m\lambda_j^2} \int \phi(x) \frac{d^2}{dx^2} \phi_{k-l}(x) dx . \quad (3.21)$$

These depend only on  $k-l$ , and can be calculated through solution of a linear system of equations [27], as discussed before.

The behaviors of the standard and finite-difference filters are studied in Fig. 3.6 as functions of the scale  $\lambda_j$  using  $\lambda = 1/4$  and  $j = 0 - 5$ . The OMGC chosen is

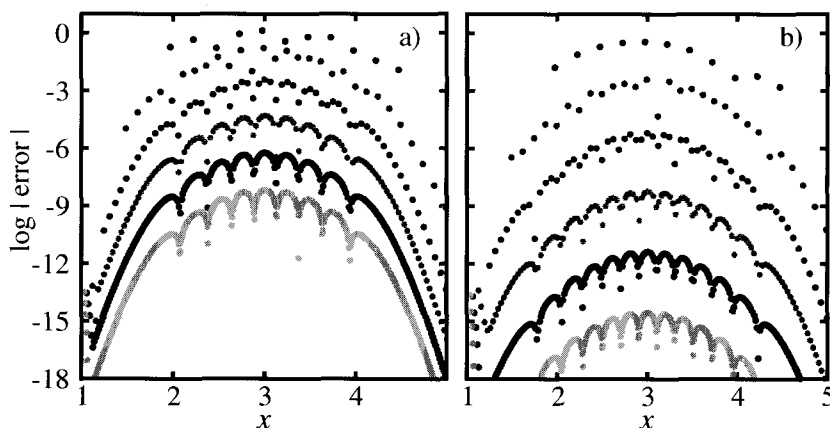


Figure 3.6: Errors in scaling function projections of second derivative of Gaussian calculated for OMGC 12a using a) standard matrix-element filter of length 21 and b) finite-difference filter of length 11. The scales used are  $\lambda_j$  using  $\lambda = 1/4$  and  $j = 0 - 5$  in descending order of absolute errors (decadic scale). The dots represent the mean positions of each included scaling function on each scale.

12a, for which  $M = 4$  and  $N = 7$ . Error is measured relative to fully-converged projections of the second derivative of the Gaussian. It is seen that the absolute error converges much more quickly for the finite-difference filter of length 11 even though it is approximately half the length ( $2L - 3 = 21$ ) of the matrix-based filter for the second derivative operator.

It is well-known in the area of grid-based electronic structure [28, 29] that ordinary

FD operators underestimate kinetic energy contributions. There it is found that they may still yield lower absolute error, even though the eigenvalue convergence is from below (non-variational). The bottom line for the current work is that a series of differentiation filters are available for use with the OMGC scaling functions that can be tuned for either higher accuracy or shorter filter length. These have applications in both the quantum and EM cases.

### 3.4 Regular and Higher-Order Filter Reconstruction

With accurate methods available to calculate projection integrals of a function  $f(x)$ , the original real space values of the function may also be required. This *reconstruction* of the original function from projection coefficients and basis function values was written in Eq. (2.15). It is a transformation to approximate sampled values of the original function at particular sample positions  $x_i$

$$f(x_i) = \sum_k f_{jk}^\lambda \phi_{jk}^\lambda(x_i) + \mathcal{O}(\lambda_j^M) . \quad (3.22)$$

The regular reconstruction procedure evaluates this sum directly. It is assumed that the expansions coefficients are known exactly or at least to higher-order error, which may be guaranteed in general by Eq. (2.44) or Eq. (2.47) and by use of refinement if necessary. The  $\phi_{jk}^\lambda(x_i)$  can be evaluated accurately using the two-scale relation if the  $x_i$  are chosen as  $\lambda$  times dyadic rationals.

In Section 2.4 it was shown that functions  $f(x) = x^p$  with  $0 \leq p < M$  are exactly expanded in scaling functions only. For  $x^p$  with  $p \geq M$  or for more general functions,

however, there are nonzero projections in wavelet subspaces  $\mathcal{W}_j$  which are missed using only an expansion in  $\mathcal{V}_0$ . Conventional wisdom then informs us that such an expansion limits the smallness of reconstruction error to  $\mathcal{O}(\lambda^M)$ . If that were true, there would be little sense in using the OMGCs since  $M$  is minimized.

As mentioned, Neelov and Goedecker [23] demonstrate in the Daubechies case ( $M = L/2$ ) that one can convolve the scaling function projection coefficients for  $f$  to find samples  $f(k\lambda)$  with error  $\mathcal{O}(\lambda^L)$  of twice the usual exponent. The filter coefficients turn out to be the same as the quadrature weights in Eq. (2.48) for  $x_q = 0, 1, \dots, L-1$ . Thus, the same filter is able to estimate projection integrals from function samples and vice versa. This ability to beat the approximation order of the basis is important for bases with a relatively low approximation order (such as the OMGCs discussed in Section 3.2) or when faster convergence is sought.

We have investigated the matter more deeply elsewhere and have determined that, for a general function  $f$ ,

$$f(\tau\lambda) = \lambda^{-1/2} \sum_{q=0}^{n-1} f_{\kappa+q}^{\lambda} A_q^{\kappa,\tau} + \mathcal{O}(\lambda^n) . \quad (3.23)$$

The quantity  $\kappa$  is the  $k$ -index of the first of the  $n$  projections. The quantity  $\tau\lambda$ , with  $\tau$  not necessarily integral, is the position of the reconstructed sample. This is the *filter reconstruction* of  $f$  from projection coefficients and length- $n$  reconstruction

filters. The filter coefficients have the form

$$A_q^{\kappa, \tau} = \sum_{p=0}^{n-1} (-1)^p \frac{a_p}{p!} L_{nq}^{(p)}(\tau - \kappa) \quad (3.24)$$

where the  $a_p$  are calculated recursively from

$$\sum_{p'=0}^p (-1)^{p'} a_{p'} m_{p-p'} = \delta_{p0} \quad (3.25)$$

one value of  $p$  at a time. For all wavelet families with the usual convention  $m_0 = 1$  (not just coiflets), it is found that  $a_p = m_p$  for  $p < L$  as a result of known relations [13, 23] between the moments defined in Eq. (2.35). In fact, we have determined that one may continue the recursion to  $p = L$  and beyond, though the  $a_p$  are then no longer equal to the  $m_p$ .

The same filters  $A_q^{\kappa, \tau}$  can be used starting at different  $\kappa$  since they depend on  $\tau$  and  $\kappa$  only through the combination  $\nu = \tau - \kappa$ . For Daubechies wavelets with  $n = L$  in Eq. (3.24), for example, it is found that  $\nu = L - 2$  or  $L - 1$  are generally best. The latter filter is the specific example utilized by Neelov and Goedeker [23].

The three OMGC scaling functions used in Fig. 3.5 are again used in Fig. 3.7 to examine convergence of reconstruction with  $j$ . All projections used are converged. It is seen immediately that conventional reconstruction converges rather slowly with  $j$ . This is as expected for low- $M$  families. Use of the  $A_q^{\kappa, \tau}$  filters with  $n = M$  actually gives parallel but worse errors. However, one may systematically increase  $n$  to increase convergence rates, completely overcoming the low- $M$  disadvantage.



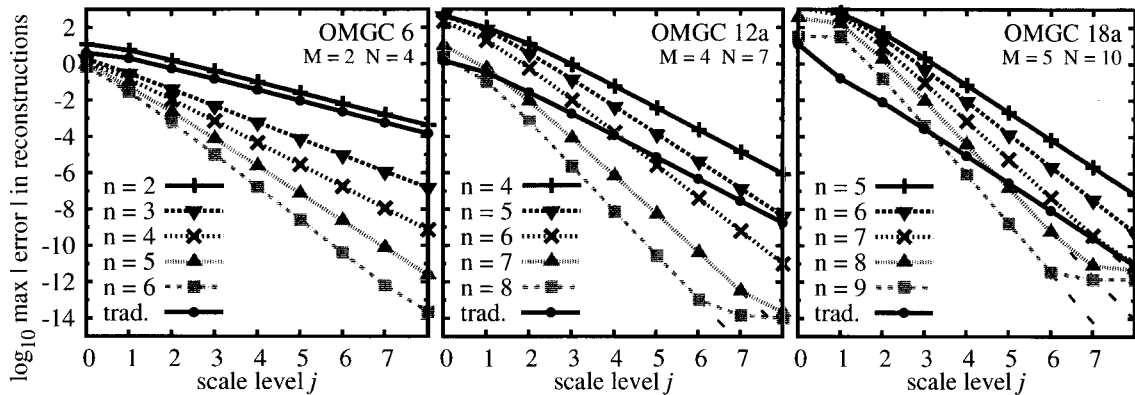


Figure 3.7: Comparison of maximum absolute errors between traditional reconstruction and filter reconstructions at different scales  $\lambda_j$  with  $\lambda = 1/4$  for the three OMGC scaling functions  $L = 6, 12a$  and  $18a$  shown in Figs. 3.1 and 3.3. Black lines correspond to traditional reconstruction with  $\mathcal{O}(\lambda_j^M)$  errors. Colored lines correspond to use of filters  $A_q^{\kappa,\tau}$  with  $n = M, M+1, M+2, \dots, M+4$ .

Floating-point error plateaus occur for the highest  $n$  and  $L$  using ordinary double precision, though it is possible that these could be further lowered by careful analysis of the numerical C++ code. They are absent in the higher precision Mathematica calculations indicated by dashed lines in Fig. 3.7.

The main thrust of the current work is to perform operator calculations entirely within the wavelet representation. Ideally, return to real space, i.e., reconstruction, is only required in post-processing steps. Nevertheless, the above results guarantee that we are not limited to the approximation order of the OMGCs in subsequently extracting the spatial information.

It should also be mentioned that Neelov and Goedeker [23] strongly advocated the use of filtering operations to reduce the computational effort associated with multi-index operators, a point of view wholly adopted in the present work.

### 3.5 Summary

Use of the product approximation for scaling function coefficients in orthogonal compact-support wavelet families has been introduced and studied. It has been shown that the CPA is especially accurate for unbalanced generalized coiflets which satisfy more scaling function than wavelet function moment conditions. The optimized versions of these functions, the OMGCs, have been determined up to  $L = 20$  and it has been shown that their use makes it entirely viable to apply potential energy operators without construction of the corresponding matrix. Ordinary reconstruction using these basis functions suffers from low approximation orders, but simple coefficient convolution filters are given which are able to implement the reconstruction process at much higher-order accuracy. Similarly, the superconvergence of derivative matrix filters is reduced with the approximation order, but FD filters are shown to overcome these limitations though eigenvalue convergence from below is to be anticipated from other work (and will indeed be found in applications).

Thus, quantum eigenvalue problems can be implemented in flexible orthogonal wavelet bases without the construction of the Hamiltonian matrix, a promising development for extension to multidimensional problems. Since the CPA and derivative filters allow one to nevertheless evaluate the effect of applying the Hamiltonian operator, Lanczos-type methods can then be exploited to calculate a number of extremal eigenvalues.

The matrix-free approach is used next in several quantum eigenvalue applications.

## Chapter 4

# Time-Independent Schrödinger Equation: Eigenvalues of a Matrix-Free Hamiltonian

The Lanczos algorithm [30, 31] is a standard method for computing eigenvalues and eigenvectors within a basis that can be implemented using only matrix-vector multiplications combined with orthogonalization. It is especially applicable here, with the effects of the matrix-vector product evaluated through the use of efficient filter operations and the CPA. One transforms to a basis with a symmetric tridiagonal matrix that in favorable cases is of much smaller size but still gives a few eigenvalues accurately.

The CPA and FD differentiation filters are first used in applying the Lanczos algorithm to harmonic and fully-anharmonic vibrational mode eigenvalues, then to a coupled anharmonic 2D model for proton transfer between two heavy atoms [32]. In both anharmonic problems the Implicitly Restarted Lanczos Method [33] (IRLM) is employed to avoid slow convergence. This is shown to be necessary because of the Lanczos algorithm itself, independent of basis choice. A brief example is also presented in the proton transfer problem to demonstrate that one can easily eliminate selected product basis functions from the 2D direct product basis. The analog in grid-based

calculations would be to use a non-rectangular grid.

## 4.1 Eigenvalues with the Lanczos Algorithm

The Lanczos algorithm [31] is a method for the computation of several eigenpairs (eigenvalues and eigenvectors) of Hermitian or real symmetric matrices. Consider a real symmetric vibrational Hamiltonian matrix  $H_{lk}$ , given as  $\mathbf{H}$  in matrix notation. The basic Lanczos algorithm gives eigenpair approximations for  $\mathbf{H}$  from diagonalization of an  $n_L \times n_L$  tridiagonal Lanczos matrix  $\mathbf{T}$  for some small value of  $n_L$ , whereas  $\mathbf{H}$  is  $m \times m$  with  $n_L \ll m$ . At the heart of this algorithm is the Lanczos recursion [34] whereby an orthonormal set of length- $m$  Lanczos vectors  $\mathbf{q}_i$  are found through an iterative reduction of the original  $m \times m$  matrix to a small  $n_L \times n_L$  tridiagonal form

$$\mathbf{T} = \mathbf{Q}^T \mathbf{H} \mathbf{Q} = \begin{pmatrix} \alpha_1 & \beta_1 & & & \\ \beta_1 & \alpha_2 & \ddots & & \\ & \ddots & \ddots & \ddots & \\ & & & \ddots & \beta_{n_L-1} \\ & & & \beta_{n_L-1} & \alpha_{n_L} \end{pmatrix}. \quad (4.1)$$

The  $m \times n_L$  matrix  $\mathbf{Q}$  is orthogonal ( $\mathbf{Q}^T \mathbf{Q} = \mathbf{I}$ ) as its columns contain the Lanczos vectors  $\mathbf{Q} = [\mathbf{q}_1, \mathbf{q}_2, \dots, \mathbf{q}_{n_L}]$ , resulting in explicit matrix elements  $\alpha_i = \mathbf{q}_i^T \mathbf{H} \mathbf{q}_i$  and  $\beta_i = \mathbf{q}_{i+1}^T \mathbf{H} \mathbf{q}_i = \mathbf{q}_i^T \mathbf{H} \mathbf{q}_{i+1}$ . The Lanczos and original Hamiltonian matrices are related by an orthogonal similarity transform.

The Lanczos recursion begins with an arbitrary starting vector  $\mathbf{b}$  with the convention that  $\beta_0 = 0$  and  $\mathbf{q}_0 = 0$ . The first Lanczos vector is calculated as  $\mathbf{q}_1 = \mathbf{b}/\|\mathbf{b}\|$ ,

the last quantity denoting the 2-norm length of a vector. Subsequent Lanczos vectors are calculated through recursive use of the famous “three-term” relation

$$\mathbf{q}_{i+1} = \frac{1}{\beta_i}(\mathbf{H}\mathbf{q}_i - \mathbf{q}_{i-1}\beta_{i-1} - \mathbf{q}_i\alpha_i) = \frac{\mathbf{f}_i}{\beta_i}, \quad (4.2)$$

where  $\beta_i = \|\mathbf{f}_i\|$ . The length- $m$  column vector  $\mathbf{f}_i$  is orthogonal to all previous Lanczos vectors but may not be normalized to unity. In matrix form this recursion can be written

$$\mathbf{H}\mathbf{Q}_i = \mathbf{Q}_i\mathbf{T}_i + \mathbf{f}_i\mathbf{e}_i^T = \begin{pmatrix} \mathbf{Q}_i & \mathbf{q}_{i+1} \end{pmatrix} \begin{pmatrix} \mathbf{T}_i \\ \beta_i\mathbf{e}_i^T \end{pmatrix} \quad (4.3)$$

using matrix-matrix products involving  $\mathbf{H}$ , the matrix  $\mathbf{Q}_i$  (containing the first  $i$  Lanczos vectors in its columns), the Lanczos matrix  $\mathbf{T}_i$  (an  $i \times i$  Lanczos matrix), and the row vector  $\mathbf{e}_i^T$  (created from the length- $i$  standard basis vector with 1 in the last element).

The importance of the Lanczos algorithm on large-scale eigenvalue problems stems mainly from the fact that the large matrix  $\mathbf{H}$  only appears, see Eq. (4.2), in a matrix vector product. Algorithms relying on a matrix vector product are a perfect setting for use of the efficient, low-storage FD/CPA alternative to the matrix vector product.

The essence of the Lanczos algorithm is to form approximate eigenvalues by diagonalization of small  $\mathbf{T}_i$  matrices. In favorable cases, the eigenvalue approximations will converge to the actual eigenvalues of the original matrix  $\mathbf{H}$  as  $i$  increases using a maximum number  $n_L$  that is much smaller than  $m$ .

## 4.2 Displaced Harmonic Oscillator

Among other things, calculated eigenvalues will have some dependence on the lengths of the FD filters. In order to examine this we first consider a simple harmonic oscillator with  $\hbar = m = 1$  and  $V(x) = 200(x - 3)^2$ , for which the lowest eigenvalue is 10. The CPA application of a quadratic potential to a Gaussian is accurate, so that the error in numerical calculations arises from the application of the kinetic energy operator. The actual analytic Lanczos vectors in this symmetric case are none other than even Hermite polynomials times the starting Gaussian (not an eigenfunction).

A limited number of Lanczos steps using the  $L = 10$  OMGC scaling function basis on scales  $1/4$  and  $1/8$  were taken to generate a  $5 \times 5$  tridiagonal matrix. The lowest eigenvalue was calculated using a number of the FD filters as well as the standard filter in the rows of the kinetic energy matrix. The results are shown in Table 4.1, where it is seen that all of the finite difference cases lead to eigenvalues below 10, but

Table 4.1: Lowest eigenvalue for harmonic oscillator calculated using the Lanczos algorithm carried to 5 Lanczos vectors. The  $L = 10$  OMGC basis is used and the CPA is used for application of the potential. Finite difference and standard matrix-based differentiation filters are used for application of the potential on two different scales  $1/4$  ( $j = 0$ ) and  $1/8$  ( $j = 1$ ).

	$j = 0$	$j = 1$
$n = 3$	9.13148	9.80063
$n = 5$	9.73578	9.98128
$n = 7$	9.87951	9.99709
$n = 9$	9.93150	9.99938
$n = 11$	9.95531	9.99984
$n = 13$	9.96800	9.99995
standard	10.92035	10.14379

converge from below as  $n$  increases. In contrast, the standard filter appearing in the

kinetic energy matrix yields energy above 10 in agreement with the Ritz variational principle. In this case, it is of length 17, which is longer than any of the FD filters. In both cases, convergence with respect to increasing  $j$  is indicated.

Once again the considerations of the projection integrals mirror the situation encountered in real space, where imbedding of FD operators in matrix formulations is known to yield lower bounds to kinetic energy contributions in electronic structure. Maragakis, et al. [28], derived modifications to make these contributions upper bounds, but Skylaris, et al. [29], concluded that this leads to greater absolute errors and that the ordinary FD operators could still be used in practical calculations because of their favorable convergence properties with finer grids. This is borne out in our calculations in wavelet space as well, though other circumstances may benefit from having an underlying variational principle. If that becomes an issue, there is always the option of using the standard filter.

### 4.3 Anharmonic Morse Potential

With the ability to control the accuracy and efficiency of applying both kinetic and harmonic potential energy operators, we now consider the Lanczos algorithm for the Morse potential in Eq. (3.16) using a starting vector corresponding to the Gaussian in Eq. (3.17).

Away from the potential minimum, the Morse potential is extremely asymmetric (see Fig. 3.4). A straightforward implementation of the Lanczos algorithm is found to perform poorly in this case. While it is known to be slow to converge in various

problems, the algorithm's difficulties are usually not discussed in sufficient detail. For this reason, we have examined the analytical functions generated by the Lanczos recursion starting from the Gaussian function centered at  $x = 3$ . These results are free of any basis-set considerations.

As shown in Fig. 4.1, successive Lanczos functions move leftward from the initial

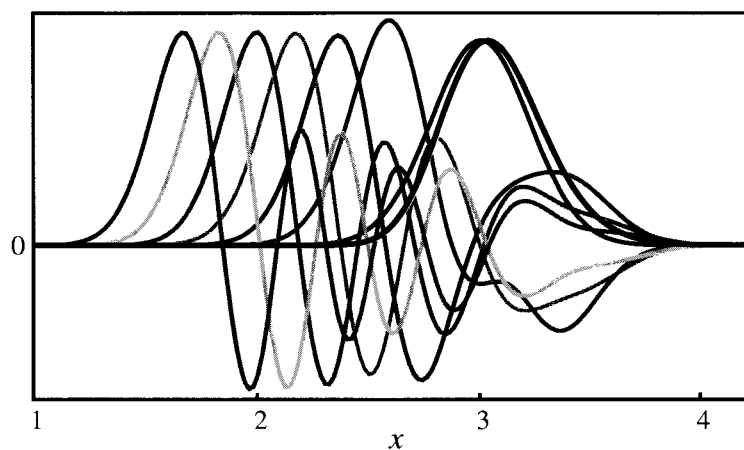


Figure 4.1: Lanczos functions/vectors calculated analytically for Morse potential. The application of the Hamiltonian asymmetrically emphasizes the left side, moving each new function further left. The thick black line represents the exact target Morse eigenfunction.

Gaussian function while the exact Morse eigenfunction, the end goal, shown with a thick black line is shifted rightward. It is the steep repulsive wall on the left that is responsible for both shifts. That the eigenfunction shifts away from the repulsion is perfectly expected. That the Lanczos vectors instead shift toward it is due to the fact that the high-energy regions of the potential function accentuate the left-hand direction every time the Hamiltonian is applied. This is combined with orthogonalization steps against previous vectors so that each new vector maintains some amplitude in the initial region, but the latter contributions are largely similar/redundant and become unable to significantly improve the linear combinations of functions approxi-



imating the true eigenfunction in its region. Thus the Lanczos process stagnates even in the exact (“infinite-precision”) version.

#### 4.3.1 Implicit Restarting with the Lanczos Algorithm

In numerical implementations, it is not uncommon for the Lanczos algorithm to require nearly as many Lanczos vectors as the original basis size. One of the important methods developed to accelerate the calculation of selective sets of eigenvalues is the IRLM [33], which is a symmetric-matrix case of the more general implicitly restarted Arnoldi methods developed by Sorensen and co-workers [35, 36, 37].

The IRLM uses only a small number of Lanczos vectors at a time, but iteratively modifies the starting vector to bring it closer to a linear combination of the true eigenvectors of interest. The idea is to continually compress the requested information for  $k$  eigenpairs into the first  $k$  columns of a length  $n_L = k + p$  Lanczos factorization through  $p$  steps of an implicitly shifted QR algorithm. Both  $k$  and  $p$  are typically modest numbers. The eigenvalues of interest are revealed in the spectrum of the order- $n_L$  tridiagonal matrix as the IRLM iterations proceed.

The temporary storage of several vectors is frequently an acceptable cost in order to take into account the contributions from large bases. The IRLM has emerged as a robust means of accelerating the convergence of the Lanczos algorithm, as well as of avoiding such issues as spurious eigenvalues [31]. It is natural to employ the IRLM in our matrix-free methods in order to counteract stagnation from the presence of strong anharmonicities.

### 4.3.2 Implicit Restarting Comparisons

The implicitly restarted Arnoldi method was used in the EM context by Hosseini et al. [38] to calculate propagation constants of dominant optical modes in plasmonic waveguides. Here the symmetric-matrix variant, IRLM, is used in the quantum eigenvalue context with our matrix-free method.

We consider the lowest eigenvalues of the Morse potential system. Calculations are carried out using two different types of bases, the OMGC 12a scaling function representation with derivative filters and the CPA, and a sinc DVR representation. The sinc DVR of Colbert and Miller [39] is a general grid discretization that treats all locations within the grid democratically and with the same resolution. It may be considered as sampling of a non-compact-support sinc (Shannon) wavelet basis, and has provided a standard against which, for example, sophisticated distributed-approximating-functional generalizations [40, 41] have been compared. While the sinc-basis kinetic energy matrix in 1D is full, this is not a serious disadvantage even for multi-mode problems since kinetic operators usually involve at most one- or two-mode operators at a time [39].

We calculate the lowest eigenvalues of the Morse potential via the IRLM in OMGC and sinc DVR bases. These are chosen to have the same spacing ( $\lambda = 1/32$ ) and number of elements (214) for comparison. For the OMGC basis with converged projections of the initial Gaussian and potential functions the  $n = 9$  FD filter and the CPA were used. For the sinc DVR basis, the full kinetic energy matrix was used. The first three eigenvalues,  $k = 3$ , are shown in Table 4.2 using  $p = 7$  extra Lanczos

vectors in each cycle for a small total of  $n_L = 10$  vectors.

Table 4.2: Morse potential eigenvalue calculations with the IRLM using OMGC 12a and sinc DVR bases. The spacing in both cases is  $\lambda = 1/32$  and discrete indices of both bases cover relevant ranges of interest. The  $k = 3$  lowest eigenvalues were sought and  $p = 7$  extra Lanczos vectors were included for implicit restarting purposes, giving  $n_L = 10$  total Lanczos vectors calculated in each IRLM iteration. For the OMGC basis, the  $n = 9$  FD filter is used for the kinetic energy and the CPA for the potential energy. Eigenvalue results are displayed for different IRLM iteration numbers and pure Lanczos  $n_L = 50$  and 100 results are shown in the middle rows. The full Hamiltonian matrix direct diagonalization results and the known exact eigenvalues are given in the bottom two rows for comparison.

IRLM itr.	OMGC 12a			sinc DVR		
	eig 1	eig 2	eig 3	eig 1	eig 2	eig 3
1	10.39444	38.58087	119.39378	10.39519	38.67638	119.72486
10	10.32616	29.70839	73.44379	10.32782	30.11745	80.75734
20	10.32537	29.33723	56.62719	10.32549	29.44911	64.98175
30	10.32535	29.29408	49.52179	10.32536	29.32584	55.47335
40	10.32535	29.28912	47.13679	10.32535	29.29683	50.41618
50	10.32535	29.28861	46.37238	10.32535	29.29029	48.02262
60	10.32535	29.28856	46.12418	10.32535	29.28891	46.93057
$n_L = 50$	10.32536	29.31178	50.84128	10.32540	29.35499	55.09444
$n_L = 100$	10.32535	29.28856	46.00176	10.32535	29.28856	46.00182
MB	10.32535	29.28856	46.00176	10.32535	29.28856	46.00176
exact	10.32535	29.28856	46.00176	10.32535	29.28856	46.00176

It is seen that a single Lanczos iteration is quite inaccurate for the second and third eigenvalues in both bases. This is due to the deficiencies discussed above of the basic Lanczos method for this problem. As the IRLM iterations proceed, however, convergence is obtained in each case. Ordinary Lanczos calculations with  $n_L = 50$  and  $n_L = 100$  are also carried out to verify that (in this method) significant numbers of vectors are needed to approach convergence even for the third eigenvalue. Full matrix (non-Lanczos) diagonalizations in each basis are included to further verify that the original bases chosen are adequate to obtain each of the targeted eigenvalues.

For select groups of eigenvalues, therefore, one can use the IRLM to deal effectively with the strongly repulsive potential wall that cause problems for the regular Lanczos algorithm. That is, even in strongly anharmonic potentials, the CPA can be used to avoid the construction-and-diagonalization of large matrices. Furthermore, the single-scale OMGC basis in this problem has been demonstrated to have an effectiveness comparable to that of the more familiar sinc DVR. There are remaining advantages of the wavelet approach, e.g., the multiple scale representations, that need to be developed in the CPA/filter context in future work. That is, it may be possible to improve the wavelet calculations so that they are more than just comparable, but a significant step has been taken here that is expected to strongly facilitate such improvements (in reducing both coding and computational complexities). The next item of business, however, is to demonstrate a multidimensional generalization of the CPA/FD filter method.

#### 4.4 2D Proton Transfer Model Potential

Sato and Iwata [32] constructed an anharmonic 2D model for the motion of a hydrogen atom of mass  $m$  between two heavier atoms each of mass  $M$ . Taking  $R$  to be the  $M - M$  separation and  $x$  to be the displacement of the  $H$  atom from their midpoint,

$$\hat{H} = -\frac{1}{2} \frac{m+M}{mM} \frac{\partial^2}{\partial x^2} - \frac{1}{M} \frac{\partial^2}{\partial R^2} - \frac{1}{M} \frac{\partial}{\partial x} \frac{\partial}{\partial R} + \frac{1}{2} K(R - R_e)^2 + D [1 - e^{-\beta(R/2+x-r_e)}]^2 + D [1 - e^{-\beta(R/2-x-r_e)}]^2 . \quad (4.4)$$

The heavy atoms interact harmonically, while the H atom motion is governed by two oppositely-facing Morse potentials. For a particular set of parameters, Sato and Iwata solved the eigenproblem using the Finite Element Method (FEM) with square grids up to 557 on a side to calculate the first 17 eigenvalues. In developing a general FEM approach for anharmonic and coupled bound vibrations, Xu, et al. [42], have repeated this calculation, needing only  $100 \times 100$  square grids to obtain the converged results shown in the second column of Table 4.3.

Table 4.3: Eigenvalues of the H-atom transfer model of Sato and Iwata[32]. The cubic Hermite FEM calculations by Xu, et al. [42], were converged with a  $100 \times 100$  grid in  $R$  and  $x$ . The wavelet calculations were performed using products of OMGC 12b scaling functions in  $R$  and  $x$  with  $\lambda_R = 1/64$ ,  $\lambda_x = 1/16$ ,  $169 \leq k_R \leq 195$ , and  $-19 \leq k_x \leq 9$ , i.e.  $27 \times 29$  2D basis functions. Single-point sampling and the CPA were used for application of the potential energy. The kinetic energy operator was applied using both  $n = 15$  FD filters and the standard matrix-based (MB) differentiation filters. Use of the latter gives unconverged upper bounds to the eigenvalues while use of the former gives convergence but from below.

Eigenvalue	Xu, et al.	OMGC/FD	OMGC/MB
1	740.11	740.11	740.13
2	743.39	743.39	743.41
3	751.96	751.96	751.99
4	755.89	755.89	755.93
5	763.91	763.91	763.99
6	768.40	768.40	768.49
7	774.59	774.59	774.64
8	775.99	775.99	776.19
9	780.91	780.91	781.15
10	787.76	787.76	787.99
11	788.62	788.62	788.90
12	793.43	793.43	793.93
13	797.06	797.06	797.23
14	800.05	800.05	800.70
15	802.11	802.11	802.43
16	805.95	805.95	806.87
17	810.33	810.33	810.53

A wavelet calculation was performed in a direct product basis of scaling functions in  $R$  and  $x$ , each with its own scale factor. Projections of the potential and the initial wave function (a sum of Gaussians in the two potential wells) were obtained using the single-point mean-position sample method without refinement for simplicity, and application of the double-well potential at each Lanczos step was performed using the CPA.

Application of the kinetic energy was barely more difficult than in the 1D case. The cross-terms require sequential application of first derivative filters that are obtained from Eq. (3.19) with  $i = 1$ . Again,  $n$  is taken to be odd, the centered filter in this case being antisymmetric. The IRLM was used with  $k = 17$  and  $p = 34$ . This large a value of  $p$  results in rapid convergence, avoiding stagnation and requiring less than 10 iterations for a basis size of 783 scaling function products. Lower values of  $p$  can be used by taking more IRLM iterations.

The lengths of the FD derivative filters were increased until the calculations were insensitive to further change,  $n = 15$ . As expected, this convergence with respect to  $n$  is from below. These results, given in the third column of Table 4.3, are identical to the number of digits shown. The matrix-based first and second derivative filters of lengths  $2L - 3$  were also used for the same basis and provide eigenvalues in the last column of the table that are converging from above as they should, but which are distinctly less converged.

In the variables  $x$  and  $R$ , coupling appears only as cross-terms in the kinetic energy. Our calculational method could be used for other coordinates as well, in which case the potential energy would be coupled. We have also performed similar hydrogen-bonding

vibrational calculations for the ground state of a model of water dimer constructed by Chmura, et al. [43], for use in investigation of quantum photodynamics. The detailed 2D potential function in this model, fit to ab initio data, is fully coupled in any set of coordinates.

Since the basis functions are localized and orthogonal, it is easy to eliminate those that contribute little. (Contractions are of course also possible for DVR bases such as the DVR-Distributed Gaussian Basis [44] or the sinc DVR [45].) We consider a simple example criterion of eliminating 2D basis functions where the projection coefficients of  $V$  are above a particular energy threshold. In Fig. 4.2 is illustrated such a contraction that still leaves all eigenvalues unchanged. The dots represent the

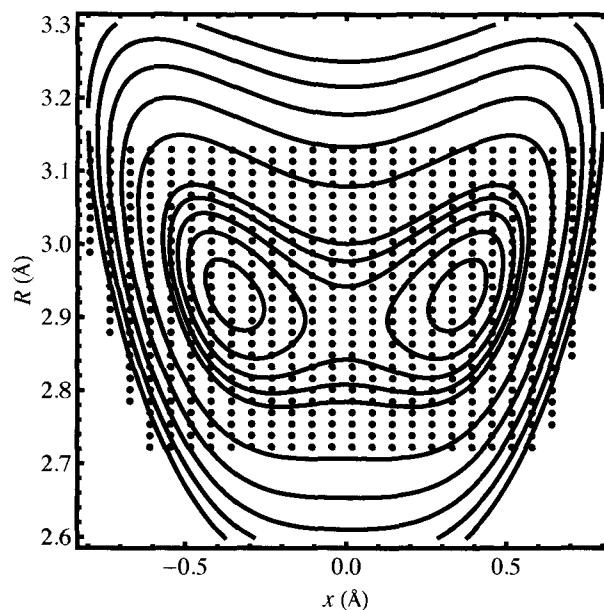


Figure 4.2: Sato and Iwata proton transfer potential function with contours at 720, 740, 760, 780, 800, 900, 1000, 1100, 1200 and 1300 vibrational units (equal to  $33.715 \text{ cm}^{-1}$ ). The dots represent mean positions of product OMGC 12b scaling functions in  $R$  and  $x$  retained in the basis after imposing the energy criterion described in the text. All 17 eigenvalues remain accurate using this basis with the CPA/FD/IRLM methods.

mean positions of the retained scaling function products, now 651 in number instead

of 783 in the direct product basis. Other selection criteria can be explored in the future, but this calculation demonstrates that one can simply prune the localized orthogonal basis functions with little effort.

As this thesis is being prepared, CPA/FD/IRLM calculations have been constructed for the large-amplitude vibrational eigenvalues of nitrosyl chloride, several of the observed transitions first seen in Dissociative Resonance Raman Spectroscopy [46, 47] experiments within the Kinsey laboratory at Rice University [48]. These calculations are on the ground state PES supplied to us by Yamashita and Kato [49], whose vibrational eigenvalues are available for comparison. Preliminary results are encouraging, so that we expect to soon have the first triatomic results from a wavelet-based calculation.



## Chapter 5

# Time-Dependent Schrödinger Equation: Evolution Equations

The TDSE is a very general foundation of quantum mechanics. In fact, it includes stationary-state solutions and the corresponding TISE as a special case. More generally, use of wavelet bases for time-propagation is a long-term goal and we have already made some contributions in this area. Chronologically, the material in this chapter predates the development of the matrix-free technology for application of the Hamiltonian operator. Nevertheless, the latter can be directly applied for polynomial propagator approaches to solving the TDSE such as the Chebyshev and Short-Iterative-Lanczos (SIL) methods, replacing the explicit matrix-vector multiplications.

During this earlier work, it was discovered that improvements could be made to the SIL propagation method for Hamiltonians that are Hermitian and time-reversal-invariant. This is a large class of applications, so it came as something of a surprise that an available simplification had not been noticed earlier. For that reason these results are set down in this chapter, using but not restricted to wavelet bases.

## 5.1 Formal Solution for Time-Independent Hamiltonian

The TDSE in the non-relativistic regime has the form

$$i\hbar \frac{\partial}{\partial t} y(\mathbf{x}, t) = \hat{H}(\mathbf{x}) y(\mathbf{x}, t) \quad (5.1)$$

where  $\hat{H}(\mathbf{x})$  is a linear time-independent Hermitian operator in  $\mathbf{x} = (x_1, \dots, x_d)$ , for  $d$  spatial degrees of freedom. We suppress the explicit dependence on  $\mathbf{x}$  for notational simplicity. The formal solution of the TDSE is

$$y(t) = \hat{U}(t) y(0) = \exp(-it\hat{H}/\hbar) y(0) . \quad (5.2)$$

Our recently developed [50] propagation algorithm is discussed first in the next section.

## 5.2 Quantum Propagation: Evolution by CSL

It is a continuing goal to achieve high-accuracy time-domain propagation of the TDSE with low computational effort [51, 52, 53, 54]. Polynomial propagation methods are a popular choice for large-scale calculations because they rely heavily on matrix-vector products which can be custom implemented in serial or parallel computing environments [51, 55, 52, 56, 57, 58]. Polynomial expansions involving orthogonal functions found by the Lanczos algorithm [34] add further advantages in that one can get accurate results with few matrix-vector products [51, 55, 56, 57].

To this end a low-order Lanczos-based polynomial propagation method for the so-

lution of the TDSE is introduced, the *Conjugate Symmetric Lanczos* (CSL) method. The CSL algorithm, discussed in the next subsection, arises from consideration of time-reversal symmetry of the TDSE for Hamiltonians not explicitly dependent on time within Krylov subspace approximations (discussed below) to the quantum propagator. One finds immediately that the Krylov basis expansion coefficients for forward propagation are simply complex conjugates of those for backward propagation. Deeper investigation reveals that this statement is also true if one transforms to an orthogonal Lanczos basis, thereby allowing efficient expansion coefficient determination by simple orthogonal projections. Remarkably, it is also found that the expansion coefficients are time-invariant, that is, they are the same for all time steps in a uniform time-stepping procedure; in practice, there are small differences due to either spatial representation or finite precision errors. The CSL method avoids the need for direct diagonalization and/or spectral estimation of the Hamiltonian, and requires nothing more than matrix-vector multiplications and inner products. The action of the matrix exponential representation of the operator is systematically approximated using only small numbers of Hamiltonian/wave-function products, and may be implemented so that only a few vectors are needed simultaneously.

Finding solutions of the TDSE usually involves two general steps: spatial discretization, which allows finite rank evaluation of the action of the Hamiltonian operator  $\hat{H}$  on the wave function, and time discretization, which utilizes finite rank approximations to the action of the exponential propagator  $\exp(-i\Delta t\hat{H}/\hbar)$  on the discretized wave function to obtain the wave function at subsequent times. The Chebyshev propagation method [58], based on a Chebyshev polynomial expansion

of the propagator, is well known for its global convergence properties, but many matrix-vector products are typically required to achieve an accuracy at or near machine precision. The SIL method [55] gives a low-order polynomial approximation, utilizing a Lanczos basis subspace where the exponential propagator is represented by a reduced dimensional matrix (cf., the discussion of the Lanczos method in the last chapter for the TISE). For large-scale problems one would like to minimize *both* the number of matrix-vector multiplications and the number of simultaneous vectors required. The Chebyshev method has the advantage of only requiring two previous vectors to generate a third, while SIL at a particular order  $n_L$  of Lanczos recursion requires all  $n_L$  vectors to be available in either fast memory or storage. The CSL method capitalizes on the reduced dimensionality of the Lanczos basis while avoiding the simultaneous need for all of the Lanczos vectors.

There are different types of spatial discretization that can be chosen. Uniform grid-based approaches allow the efficiency of the Fast Fourier Transform to be exploited [54]. Various basis function choices can be used, e.g., analytical bases associated with the use of the DVR [59, 60, 61, 62], finite elements [63, 42], etc. Orthogonal compact support wavelets are used in the present investigation which was, in fact, motivated by recent wavelet TDSE propagations using the Chebyshev method [64, 65]. The rigorous localization of the basis functions leads to sparse matrix representations of the Hamiltonian and propagator, allowing efficient customized programming of the matrix-vector multiplication steps. Within the long-range goal of developing adaptive TDSE methods, we have also investigated wavelet discretization of the time variable as well [64]. This aspect is not explored here, though the CSL method can

be employed there as well.

It is well-known in computational electromagnetics that the classical Maxwell equations in the time-domain can be expressed as a Hamiltonian system with associated exponential propagator [66]. Recent work has highlighted use of the unconditionally stable Chebyshev method for pulse propagation in non-absorbing media [67, 68], and Lanczos [69] and Faber propagation [70] methods for attenuating media. In the latter case, the field “Hamiltonian” is intrinsically non-Hermitian, a situation entirely analogous to propagations for decaying resonance states in quantum dynamics. The CSL method depends on time-reversal symmetry and the Hermiticity of the Hamiltonian, and is shown to apply immediately in a simple 1D EM non-absorbing case. However, there is a great deal of interest in calculating the electromagnetics of metal nanoparticles for, e.g., their use in surface-enhanced spectroscopies and plasmonic nanoscopic wave guides [71, 72]. Use of noble metals like silver and gold necessarily entails strong attenuation and the use of complex dielectric functions [73]. Accordingly, a method for systematic calculation of corrections to the CSL method for non-Hermitian effects is developed that involves a moderate increase in vector storage requirements, and is applied to a 1D pulse propagating across a vacuum-gold interface using a Drude model for the Au dielectric function [73].

### 5.2.1 CSL from the Lanczos Basis

Different polynomial propagation methods frequently require different numbers of matrix-vector multiplications. In part this is due to adoption of different strategic goals, for example, one-step versus multi-step propagations, adaptive versus non-

adaptive calculation, control of error build-up, etc. For moderate time steps, we are interested in determining the minimum number of matrix-vector multiplications required to achieve a particular accuracy goal. This may be examined for any choice of polynomial propagator expansion, such as the Chebyshev, SIL, and Residuum methods [56] within a Krylov basis decomposition of the exact wave function since all polynomial expansions are spanned by this basis. An  $n_L$  order Krylov subspace is the space spanned by  $n_L$  vectors  $\{\mathbf{y}, \mathbf{H}\mathbf{y}, \dots, \mathbf{H}^{n_L-1}\mathbf{y}\}$  created completely in terms of a matrix-vector products of  $\mathbf{H}$  and a vector  $\mathbf{y}$ . In the Krylov basis it is easy to ascertain the consequences of time-reversal symmetry for evolution with time independent Hamiltonians.

For short time increments  $\Delta t$ , the forward propagated solution is

$$y(t + \Delta t) = \hat{U}(\Delta t) y(t) = \exp(-i\Delta t \hat{H}/\hbar) y(t) \approx \sum_{n=1}^p a_n \hat{H}^{n-1} y(t) , \quad (5.3)$$

where the last form uses a  $p$ -term approximation to the evolution operator in a Krylov basis  $\{\hat{H}^n y(t)\}$  with coefficients  $a_n$  to be determined according to the underlying propagation method. Similarly, the backward propagated solution is

$$y(t - \Delta t) = \hat{U}^\dagger(\Delta t) y(t) = \exp(+i\Delta t \hat{H}/\hbar) y(t) \approx \sum_{n=1}^p b_n \hat{H}^{n-1} y(t) . \quad (5.4)$$

Due to the Hermiticity of  $\hat{H}$ , reversal of the sign of  $\Delta t$  corresponds to taking the Hermitian conjugate of the evolution operator. From the linear independence of the

Krylov basis functions, this is satisfied by requiring

$$a_n = b_n^* . \quad (5.5)$$

The wave function  $y(t)$  is generally complex, but only the coefficients of the Krylov basis are complex conjugated under time reversal.

At a given time  $t$ , the basis may be orthogonalized by the standard Lanczos recursion, as discussed in Section 4.1. Assuming  $y(t)$  is unit normalized, we form the continuous Lanczos basis members  $\{q_n\}$  by

$$q_1 = y(t) \quad (5.6)$$

$$q_{i+1} = \frac{1}{\beta_i} (\hat{H} q_i - q_{i-1} \beta_{i-1} - q_i \alpha_i) , \quad (5.7)$$

where  $\alpha_i = \langle q_i^T | \hat{H} | q_i \rangle$  and  $\beta_i = \langle q_{i+1}^T | \hat{H} | q_i \rangle = \langle q_i^T | \hat{H} | q_{i+1} \rangle$  with  $\beta_0 = 0$  and  $q_0 = 0$ . For Hermitian  $\hat{H}$ , the  $\alpha_i$  and  $\beta_i$  are real and form the symmetric tridiagonal matrix  $\mathbf{T}$  of the Hamiltonian in the orthogonal Lanczos basis. The Lanczos vectors are linear combinations of the complex Krylov vectors with real coefficients. Therefore, one has forward and backward expansions,

$$y(t + \Delta t) = \sum_{n=1}^{n_L} a_n^L q_n(t) , \quad (5.8)$$

$$y(t - \Delta t) = \sum_{n=1}^{n_L} b_n^L q_n(t) , \quad (5.9)$$

where the  $a_n^L$  and  $b_n^L$  are linear combinations with real coefficients of the corresponding

complex Krylov quantities,  $a_n$  and  $b_n$ , respectively. Thus, the Lanczos coefficients are also related by complex conjugation

$$a_n^L = (b_n^L)^* . \quad (5.10)$$

Let us assume that the wave function has been calculated up to time  $t$  in steps of  $\Delta t$ . Then the orthogonality of the Lanczos basis allows the  $b_n^L$  to be determined by simple projection

$$b_n^L = \langle q_n(t) | y(t - \Delta t) \rangle . \quad (5.11)$$

Once  $q_n(t)$  and  $b_n^L$  are calculated, the quantity  $(b_n^L)^* q_n(t)$  may be immediately added to the prediction for  $y(t + \Delta t)$ . One only needs vectors  $q_{n-1}(t)$  and  $q_n(t)$  to proceed to step  $n + 1$ . This simple low-order low-storage algorithm is called the *Conjugate Symmetric Lanczos* method for time-independent Hamiltonians.

Of further interest is the fact that the expansion coefficients are time-invariant. To see this, consider application of the propagator  $\hat{U}(t)$  to Eqs. (5.6) and (5.7) at time zero. Using the facts that  $\hat{U}$  and  $\hat{H}$  commute and that the  $\alpha_n$  and  $\beta_n$  are independent of time, it is easy to verify that

$$\begin{aligned} \hat{U}(t) q_1(0) &= \hat{U}(t) y(0) = y(t) = q_1(t) \\ \hat{U}(t) q_2(0) &= [\hat{H} \hat{U}(t) q_1(0) - \alpha_1 \hat{U}(t) q_1(0)] / \beta_1 = [\hat{H} q_1(t) - \alpha_1 q_1(t)] / \beta_1 = q_2(t) \\ &\dots \\ \hat{U}(t) q_{n_L}(0) &= q_{n_L}(t) . \end{aligned} \quad (5.12)$$



This means that

$$\begin{aligned}
 a_n^L(t, \Delta t) &= \langle q_n(t) | y(t + \Delta t) \rangle \\
 &= \langle q_n(0) | \hat{U}^\dagger(t) \hat{U}(t + \Delta t) | y(0) \rangle \\
 &= \langle q_n(0) | y(\Delta t) \rangle ,
 \end{aligned} \tag{5.13}$$

which is independent of  $t$ . Thus, the wave function and Lanczos basis functions change with absolute time, but their coefficients of projection,  $a_n^L$  and  $b_n^L$ , in neighboring-time wave functions rigorously depend only on  $\Delta t$ .

This is strictly true only for the exact Lanczos basis functions. When approximated in a finite basis using finite precision, there will generally be errors in the numerically determined Lanczos vectors and CSL coefficients. The Lanczos vector expansion in Eqs. (5.8) and (5.9) have the same formal appearance as in the SIL method, and the coefficients are expected to coincide for infinite precision and resolution. However, there will in practice be differences since the SIL method imposes the stronger requirement of strict unitarity of the transformation at any level of approximation (see below). We will examine the dependence of the errors on resolution using wavelets at different scales.

### 5.3 Quantum Propagation: Evolution by CSL, Chebyshev, and SIL Methods

After a brief outline of the Chebyshev and SIL propagation methods the CSL algorithm is investigated with prototypical quantum systems. The Chebyshev and SIL methods are also employed for comparative purposes. The first prototypical systems is a displaced harmonic oscillator problem serving as a model for an electronic transition. The known analytical oscillator solution not only allows examination of CSL and SIL errors, but Chebyshev errors as well. In an anharmonic example, we study a Morse oscillator system where, in lieu of an analytical solution, CSL and SIL errors are measured with respect to Chebyshev method errors. The latter may be driven down to the intrinsic errors for the fixed spatial resolution at the expense of an increased number of matrix-vector products.

The SIL method is a low order Krylov-based propagation scheme for use with small time steps. The corresponding action of the propagator on the initial wave function is given by

$$\mathbf{y}(t + \Delta t) = \exp(-i\mathbf{H}\Delta t/\hbar) \mathbf{y}(t) \approx \rho \mathbf{Q} \exp(-i\mathbf{T}\Delta t/\hbar) \mathbf{e}_1, \quad (5.14)$$

where  $\rho = \|\mathbf{y}(t)\|$  is the 2-norm of the initial vector,  $\mathbf{Q}$  is the matrix of Lanczos column vectors, and  $\mathbf{e}_1$  is an  $n_L$ -element unit column vector with one in the first row. Formally, one must still compute a matrix exponential although the dimensionality of the matrix has been reduced to that of a smaller  $n_L \times n_L$  tridiagonal matrix  $\mathbf{T}$ . This

matrix can be orthogonally transformed to a diagonal matrix  $\mathbf{D} = \mathbf{V}^T \mathbf{T} \mathbf{V}$  where the columns of  $\mathbf{V}$  contain the eigenvectors of  $\mathbf{T}$ . In this representation, the exponential propagator is simply a diagonal matrix with each element being an exponential of a scalar. Reversing the orthogonal transformation, one obtains

$$\mathbf{y}(t + \Delta t) \approx \rho \mathbf{Q} \mathbf{V} \exp(-i \mathbf{D} \Delta t / \hbar) \mathbf{V}^T \mathbf{e}_1. \quad (5.15)$$

The use of low-order Lanczos vectors minimizes the edge effects that scaling function and wavelet bases experience (the truncation is localized to the edge regions), and this can be controlled by taking the range  $x_{\min}$  and  $x_{\max}$  to be strongly outside the range where the wave function has any significant amplitude. Application of  $\mathbf{H}$  to  $\mathbf{y}(t)$  many times, e.g. for higher-order Lanczos or Chebyshev methods, will ultimately cause errors in the higher-order Lanczos vectors relative to the exact vectors. Ideally, we avoid this occurrence by keeping the order at ten or less. This can be controlled by the time-step since shorter time-steps decrease the coefficient sizes especially for higher order. A variable time-step has been employed in the earlier Residuum [74] method and can generally be employed in the SIL method [55, 75].

For a finite matrix  $\mathbf{H}$  the Chebyshev method first requires use of a scaled and shifted matrix  $\mathbf{H}' = (\mathbf{H} - E_{\text{av}})/E_{\text{hw}}$ , modifying the spectral range to  $\sim [-1, +1]$ . The average and half-width energy, defined by  $2E_{\text{av}} = E_{\text{max}} + E_{\text{min}}$  and  $2E_{\text{hw}} = E_{\text{max}} - E_{\text{min}}$ , can be calculated or estimated by different means. The action of the

propagator in the Chebyshev method is computed as

$$\begin{aligned} \mathbf{y}(t + \Delta t) &= \mathbf{U}(\Delta t) \mathbf{y}(t) \\ &\approx \exp(-iE_{av}\Delta t/\hbar) \sum_{n=0}^{n_{\max}} (2 - \delta_{n0})(i\hbar)^{-n} J_n(E_{hw}\Delta t/\hbar) \mathbf{X}_n \end{aligned} \quad (5.16)$$

where  $J_n$  are Bessel functions of the first kind and the vectors  $\mathbf{X}_n$  are generated by a series of matrix-vector multiplications in a three term recursion  $\mathbf{X}_{n>1} = 2\mathbf{H}' \mathbf{X}_{n-1} - \mathbf{X}_{n-2}$  with  $\mathbf{X}_0 = \mathbf{y}(t)$  and  $\mathbf{X}_1 = \mathbf{H}' \mathbf{X}_0$ . The Bessel function expansion coefficients decay exponentially as the index  $n$  exceeds the argument. The Chebyshev method is of course not limited to small time steps, but longer time durations require higher  $n_{\max}$  to achieve convergence.

### 5.3.1 Displaced Harmonic Oscillator

A simple vibrational model is first examined, a 1D displaced harmonic oscillator [64] with Hamiltonian given by

$$\hat{H}(x) = -\frac{\hbar^2}{2m} \frac{d^2}{dx^2} + \frac{k}{2}(x - x_0)^2. \quad (5.17)$$

The ground state wave function of the harmonic oscillator,

$$y(x, 0) = (\alpha/\pi)^{1/4} e^{-\alpha x^2/2}, \quad (5.18)$$

is used as the initial state in the propagation where  $\alpha = m\omega/\hbar = \sqrt{km}/\hbar$ . The solution to the TDSE involving  $\hat{H}$  has a known form

$$y(x, t) = (\alpha/\pi)^{1/4} \exp \left[ -\frac{\alpha}{2}(x - x_{\text{cl}})^2 + i\alpha x_0 \sin(\omega t)(x - x_{\text{cl}}) - i\frac{\alpha}{2}x_0^2 \cos(\omega t) \sin(\omega t) - i\frac{\omega t}{2} \right], \quad (5.19)$$

where  $x_{\text{cl}} = x_0 - x_0 \cos(\omega t)$ . This solution reduces to  $y(x, 0)$  at  $t = 0$ , see Fig. 4 of Wang et al. [64] The exact Lanczos vectors for the displaced oscillator turn out to be

$$q_n(x, t) = (-1)^n (2^n n!)^{-1/2} H_n(\alpha^{1/2}(x - x_{\text{cl}})) e^{-in\omega t} y(x, t), \quad (5.20)$$

that is,  $(-1)^n$  times the wave packets evolving from excited states  $n$  at  $t = 0$ . Here the Hermite polynomial  $H_n$  is centered on the classical position  $x_{\text{cl}}$ . The exact expansion coefficients are then obtained from a standard integral,

$$\begin{aligned} a_n^L(\Delta t) &= \langle q_n(t) | y(t + \Delta t) \rangle = \langle q_n(0) | y(\Delta t) \rangle \\ &= (2^n n!)^{-1/2} \left[ -i \sin\left(\frac{\omega \Delta t}{2}\right) \right]^n \exp \left[ -\frac{\alpha x_0^2}{2} (1 - e^{-i\omega \Delta t}) - i\frac{n+1}{2} \omega \Delta t \right]. \end{aligned} \quad (5.21)$$

We consider the displaced oscillator with  $\hbar = m = \omega = 1$  and  $x_0 = 1/2$ . For a single-scale expansion in scaling functions  $\phi_{jk}^\lambda$ , single time step errors are examined in Fig. 5.1 for different  $L$ , discretization steps  $\lambda$ , and time step  $\Delta t$ . These errors are defined as the maximum absolute error across all scaling function expansion coefficients. For the two values of time step used, the errors are similar and therefore dominated by

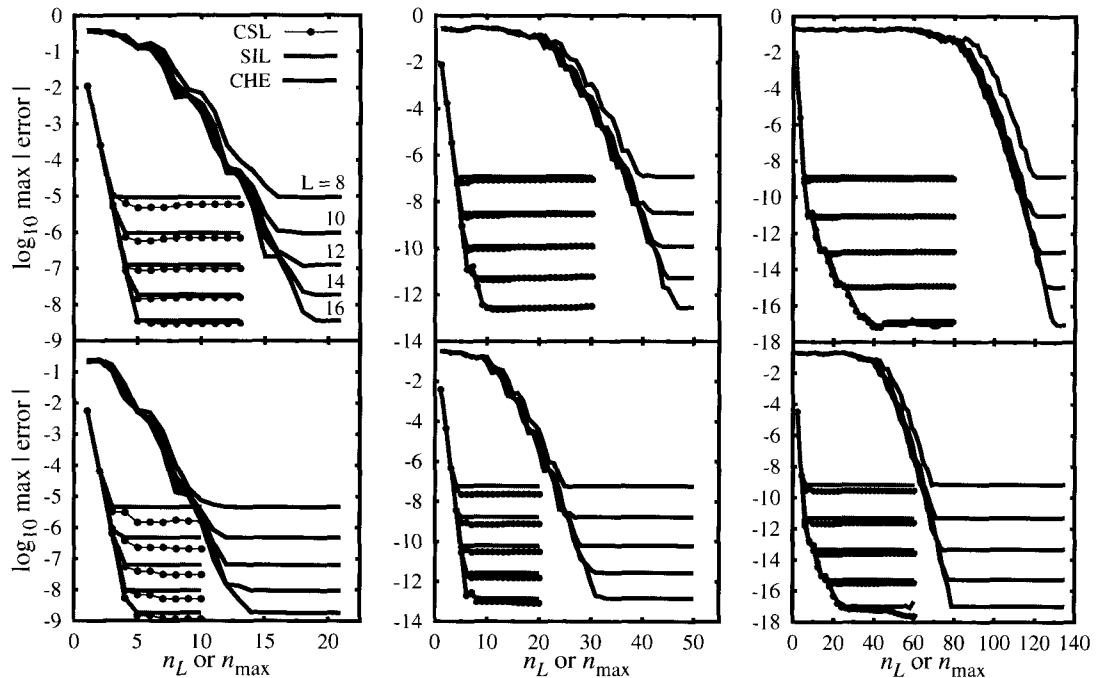


Figure 5.1: Plots of maximum scaling function coefficient errors in  $|\mathbf{y}(\Delta t)|$  versus  $n_L$  (CSL and SIL) or  $n_{\max}$  (Chebyshev) of the displaced harmonic oscillator propagated after one time step,  $\Delta t = 2\pi/2^6$  along the top row and  $\Delta t = 2\pi/2^7$  along the bottom row, when compared to the scaling function representation of the exact result. Symmetlet bases of different orders  $L$  are shown with  $\lambda_0$ ,  $\lambda_1$ , and  $\lambda_2$  equal to  $1/4$ ,  $1/8$ , and  $1/16$  column-wise, respectively. All scaling functions fully contained in the interval  $-9 \leq x \leq 10$  are used.

spatial resolution limitations. It is seen that decreasing spacing (increasing  $j$ ) leads systematically to exponentially decreasing errors, though progressively higher orders are needed at the same time in either Lanczos or Chebyshev methods to achieve these decreased errors. With a larger time step the Chebyshev method requires a larger number of matrix-vector products compared to the slight increase in required matrix-vector products for CSL and SIL. CSL and SIL errors roughly track each other. These results are expected to be improved through use of FD in place of the standard kinetic energy filters used here.

There is generally an error level below which additional numerical Lanczos vectors

in the wavelet basis drastically slow down in error reduction. For any of the polynomial methods, it is seen that saturation levels exist and are proportional to  $\lambda_j^{L/2}$  where  $L/2$  is the *approximation order* or, equivalently, one more than the polynomial order for which the scaling functions provide an exact expansion basis. Thus, higher  $L$  provides deeper convergence with somewhat increased computational cost for either Lanczos or Chebyshev methods. We can systematically choose the level of precision and use this to guide the choice of  $L$  and  $\lambda_j$ .

Multiple time step errors in dynamic scaling function coefficients are shown in Fig. 5.2 over twenty oscillator periods. For all three methods, the error shows a sharp

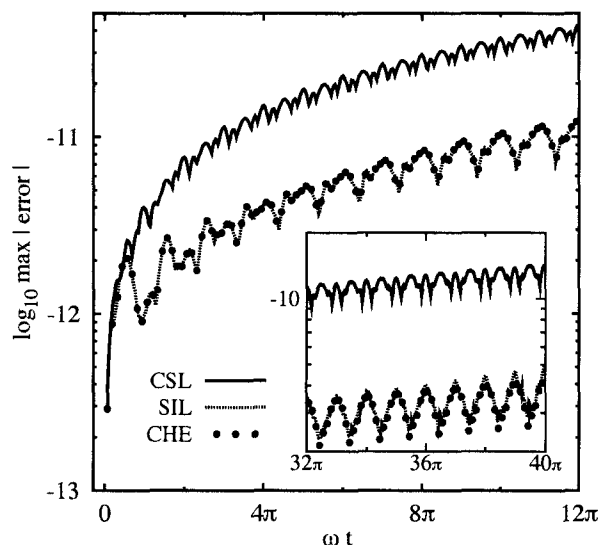


Figure 5.2: Plots of maximum scaling function coefficient errors in  $|\mathbf{y}(t)|$  of the displaced harmonic oscillator versus time ( $\Delta t = 2\pi/2^6$ ) when compared to the scaling function representation of the exact result. For every time step, the number of Lanczos vectors for both CSL and SIL is  $n_L = 21$  and the Chebyshev order is  $n_{\max} = 56$ . An  $L = 16$  symmlet basis is used with 138 functions,  $k_{\min} = -72$ ,  $k_{\max} = 65$ , and  $\lambda = 1/8$ . SIL and Chebyshev error curves track each other strongly.

increase at earlier times but levels out on the semilog plot over longer times. There are small periodic oscillations in this accumulated error, similar to those observed in a

related earlier investigation [64]. In this case, it is found that the SIL and Chebyshev cumulative errors track each other strongly and CSL errors are about an order of magnitude worse. In further examinations, the magnitudes of CSL and SIL errors are found to vary with respect to each other from case to case, so no clear-cut superiority has become established. To maintain CSL and SIL accuracy in the face of accumulated error, it was found necessary to use a higher order  $n_L = 21$  for the calculations in Fig. 5.2. The use of higher  $n_L$  values is not desirable from our point of view. There are other parameters that may be adjusted for maintaining higher accuracy in any of these methods, namely use of (1) wavelets with higher approximation order, (2) increased spatial resolution, and (3) decreased time step (the latter giving somewhat more improvement than for a single step). Figure 5.2 is just a representative example.

### 5.3.2 Morse Oscillator

We next examine the performance of the CSL algorithm for an anharmonic Hamiltonian. We use the HF molecule example used by Gray and Manolopoulos [76] in their symplectic integrator [57] propagation of the TDSE for an initial Gaussian function evolving under the influence of a Morse potential. There is no analytical solution for comparison unlike the previous case. Instead, CSL and SIL errors are referenced to converged Chebyshev results. The Hamiltonian and initial wave function are

$$\hat{H} = -\frac{\hbar^2}{2\mu} \frac{d^2}{dx^2} + D_e (1 - e^{-ax})^2 \quad (5.22)$$

$$y(x, 0) = (2\Gamma/\pi)^{1/4} e^{-\Gamma(x-d_e)^2} \quad (5.23)$$



where  $\mu = 1744.95008$  a.u.,  $D_e = 0.225084521$  a.u.,  $a = 1.1741$  a.u.,  $\Gamma = \sqrt{D_e \mu a^2 / 2}$ , and  $d_e = -0.3$  a.u. Multiple time step errors for the Morse oscillator are shown in Fig. 5.3. As in the harmonic case, there is a large jump in error during the initial

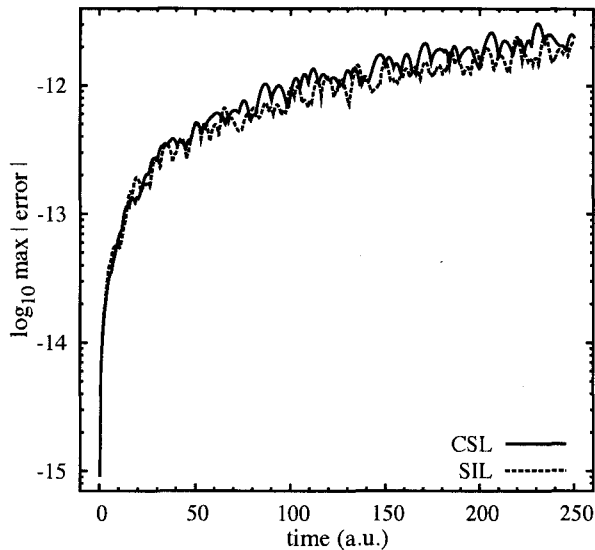


Figure 5.3: Plots of maximum Morse scaling function coefficient errors in  $|y(t)|$  versus time ( $\Delta t = 1/8$ ) compared to Chebyshev propagation. For both CSL and SIL,  $n_L = 7$ , and the Chebyshev order is  $n_{\max} = 15$ . An  $L = 12$  symmlet basis is used with 198 functions,  $k_{\min} = -32$ ,  $k_{\max} = 165$ , and  $\lambda = 1/16$ .

steps. In this particular case, however, the CSL and SIL error levels are found to be essentially identical. The number of matrix-vector products ( $n_L = 7$ ) needed for convergence is less than half of that required for the Chebyshev method ( $n_{\max} = 15$ ).

## 5.4 Electrodynamics

Recent work has been dedicated to using Chebyshev [68], Lanczos [69, 77], and Faber [70] propagation methods to solve problems of electrodynamics in different types of media. These tools familiar in quantum dynamics are enabled by virtue of the fact that Maxwell's equations may be put in the form of a TDSE.

Our choice of a wavelet spatial representation was guided by current-day nanophotonic applications where strong local EM fields can arise from surface plasmon resonances. In such cases, wavelet bases are natural for describing strong local phenomena by virtue of their inherent multiresolution capabilities. Only single scale wavelet bases are necessary for the initial 1D examples presented in the following sections; however, the real interest is in investigating 2D and 3D systems with surface plasmon resonances using multiresolution representations.

#### 5.4.1 Vacuum Propagation

The simplest case is propagation in vacuum, for which Maxwell's curl equations are

$$\epsilon_0 \frac{\partial}{\partial t} \mathbf{E} = \nabla \times \mathbf{H} \quad (5.24)$$

$$\mu_0 \frac{\partial}{\partial t} \mathbf{H} = -\nabla \times \mathbf{E} . \quad (5.25)$$

In the case of propagation along  $z$  with initial nonzero components  $E_x(z, 0)$  and  $H_y(z, 0)$ , one only needs to solve the coupled equations

$$\epsilon_0 \frac{\partial}{\partial t} E_x(z, t) = -\frac{\partial}{\partial z} H_y(z, t) \quad (5.26)$$

$$\mu_0 \frac{\partial}{\partial t} H_y(z, t) = -\frac{\partial}{\partial z} E_x(z, t) . \quad (5.27)$$

These can be put in Hermitian Hamiltonian form using scaled field components and the relation  $\sqrt{\epsilon_0\mu_0} = 1/c$  (SI units),

$$\left[ i\frac{\partial}{\partial t} - \hat{\Omega} \right] \cdot \begin{pmatrix} F_1 \\ F_2 \end{pmatrix} = \left[ i\frac{\partial}{\partial t} - \begin{pmatrix} 0 & c\hat{p}_z \\ c\hat{p}_z & 0 \end{pmatrix} \right] \cdot \begin{pmatrix} \sqrt{\epsilon_0} E_x(z, t) \\ \sqrt{\mu_0} H_y(z, t) \end{pmatrix} = 0 \quad (5.28)$$

with  $\hat{p}_z = -i\partial/\partial z$ .

We consider the example of pulse propagation for an initially complex Gaussian pulse discussed by Borisov [69], modified to propagate from large positive  $z$  to lower  $z$ ,

$$F_1(z, 0) = -F_2(z, 0) = \exp(-z^2/D^2 - ik_0 z) \quad (5.29)$$

$$F_1(z, t) = -F_2(z, t) = \exp \left[ -(z + ct)^2/D^2 - ik_0(z + ct) \right], \quad (5.30)$$

with parameters  $D = 1.75 \mu\text{m}$ ,  $\bar{\lambda} = 2 \mu\text{m}$ , and  $k_0 = 2\pi/\bar{\lambda}$ . This pulse translates unchanged through a given  $z$  region in about 25 fs. We again have an analytic solution that allows direct assessment of the propagation error. The scaling functions are chosen to have a spacing  $\lambda = D/10$ , the same as the grid spacing used in Borisov et al. [69], and a time step  $\Delta t = 1/10$  fs.

The two initial components  $F_i(z, 0)$ ,  $i = 1$  and  $2$ , are expanded in an  $L = 10$  symmlet basis with  $k_{\min} = -54$  and  $k_{\max} = 50$ . Setting  $j = 0$  and ignoring this subscript,

$$F_i(z, 0) = \sum_{k=k_{\min}}^{k_{\max}} F_{ik}^{\lambda}(0) \phi_k^{\lambda}(z). \quad (5.31)$$

The vector of coefficients,  $\mathbf{F}_i(t) = [F_{i,k_{\min}}^{\lambda}(t), \dots, F_{i,k_{\max}}^{\lambda}(t)]^T$ , may be calculated using

wavelet quadrature on a finer scale followed by two-scale recursion back to the target scale. This converges exponentially with the number of refinement scales, with four levels providing convergence to better than  $10^{-16}$  for the current problem. The only error is therefore due to the use of a finite resolution basis for the expansion, and this can be systematically decreased by choice of  $\lambda$ . Merging the vector  $\mathbf{F}_1(0)$  with its negative  $\mathbf{F}_2(0) = -\mathbf{F}_1(0)$ , the total vector  $\mathbf{F}$  has  $2N$  coefficients. The  $\mathbf{\Omega}$  operator matrix is then  $2N \times 2N$  but sparse in the scaling function representation. Otherwise, the CSL algorithm is formally the same as before. In the calculations, decomposition into the separate blocks has a computational advantage due to the form of  $\hat{\Omega}$  in Eq. (5.28).

We consider the converged projections for the three vectors  $\mathbf{F}(0)$ ,  $\mathbf{F}(\Delta t)$ , and  $\mathbf{F}(2\Delta t)$ . The expansion coefficients,  $a_n^L$  and  $b_n^L$ , of  $\mathbf{F}(2\Delta t)$  and  $\mathbf{F}(0)$ , respectively, in the Lanczos basis created from  $\mathbf{F}(\Delta t)$ , are complex conjugates to within the precision used. This differs from the oscillator case, and is presumed to be due to specifics of the matrix  $\mathbf{\Omega}$ . The logarithmic magnitudes of the  $a_n$  coefficients are shown in Fig. 5.4 for different values of  $L$ , decreasing linearly at first and then leveling off significantly. From the displaced oscillator example, the latter fact is recognized as due to scaling function approximation-order limitations in representing the exact Lanczos vectors. This is evident from the increased linear region and increasingly deeper leveling region as  $L$  increases.

The key question is the accumulation of error as multiple time steps are taken. This is shown in Fig. 5.5, where maximum absolute errors in the projection coefficients of the symmlet bases are shown for 40 time steps with  $\Delta t = 1/10$  fs. A number of

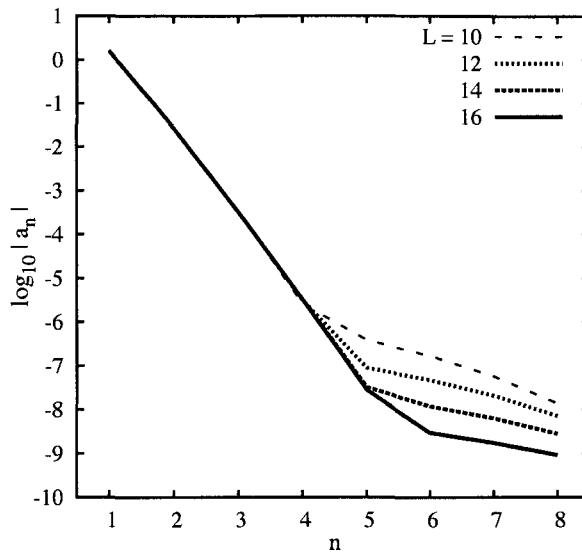


Figure 5.4: The logarithm of coefficient magnitudes,  $\log_{10} |a_n|$ , for a single time step ( $\Delta t = 1/10$  fs) in the free propagation of an EM pulse using symmlet bases with  $\lambda = D/10$  and different  $L$ : 10, 12, 14 and 16.

different values of  $L$  are used, and the top group corresponds to  $\lambda = D/10$ , the spacing used by Borisov and Shabanov [69]. The bottom group corresponds to  $\lambda = D/20$ . One can see that the accumulated error decreases with both  $L$  and scale, at least for this length of propagation.

#### 5.4.2 Propagation in Drude Materials

Non-Hermitian Hamiltonians commonly arise in molecular physics. They generally lead to complex eigenvalues and breakdown in conservation of the norm. The unconditionally stable Chebyshev expansion method has been modified by Huang, et al., [78] to handle the time propagator,  $\exp(-i\Delta t \hat{H}/\hbar)$ , for non-Hermitian  $\hat{H}$  by generalizing to Faber polynomial expansions and complex spectral domains. In the Hamiltonian formulation of electrodynamic problems, intrinsically non-Hermitian Hamiltonians also occur, e.g., when the dielectric function is complex as it is for absorbing

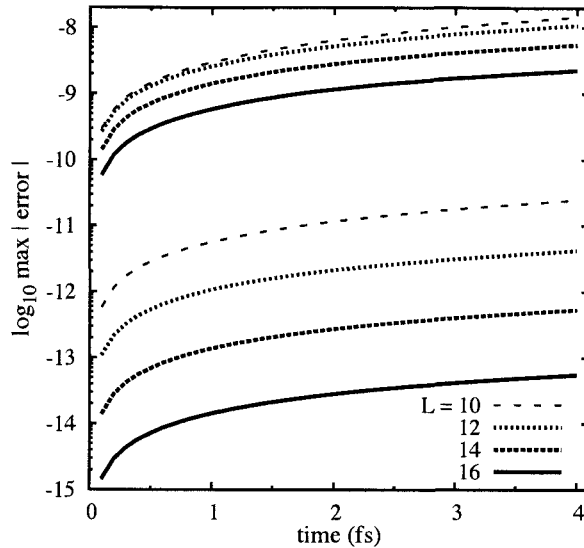


Figure 5.5: Coefficient errors for free propagation of an EM pulse for different values of  $L$  with  $n_L = 8$ . The upper four curves are for  $\lambda = D/10$ , the bottom four for  $\lambda = D/20$ .

materials. Borisov and Shabanov have very recently applied the Faber method to such cases [70]. Lanczos methods with suitable generalizations may also be applied to non-Hermitian EM Hamiltonians [77, 69]. The direct extension of the SIL method then only requires diagonalization of a smaller non-Hermitian tridiagonal [77] or Hessenberg [69]  $\mathbf{T}$  matrix, although stability must be examined. On the other hand, the CSL method relies on time-reversal symmetry, i.e., equating the Hermitian conjugate of the propagator with the propagator for reversed time. This no longer holds for Hamiltonian problems with attenuation. It is therefore of interest to examine more closely the breakdown of the CSL method in this situation.

As an example, we consider the problem of a metal with the dielectric function modeled as a Drude oscillator,

$$\epsilon(\omega) = \epsilon_\infty - \frac{\omega_p^2}{\omega(\omega + i\gamma)} . \quad (5.32)$$

Here  $\epsilon_\infty$  is the dielectric contribution due to core electrons,  $\omega_p$  the bulk plasma frequency,  $\omega$  the excitation frequency, and  $\gamma$  the attenuation width. The current calculations are carried out with  $\epsilon_\infty = 9.4$ ,  $\omega_p = 2.16 \times 10^{15}$  Hz, and  $\gamma = 1.75 \times 10^{13}$  Hz, found by a non-linear fit of experimental data [73] for gold. This is relevant to low-frequency excitation of metal particles and current research in nanophotonics. Following the time-domain development by Borisov [69], one has a basis consisting of suitably scaled  $\mathbf{E}$  and  $\mathbf{H}$  fields and vector  $\mathbf{Q}$  corresponding to the time derivative of the polarization divided by  $\omega_p$ . Once again considering propagation along the  $z$  axis, the Hamiltonian and corresponding field components take the forms

$$\hat{\Omega} = \begin{pmatrix} 0 & (c/\sqrt{\epsilon_\infty}) \hat{p}_z & -i\omega_p/\sqrt{\epsilon_\infty} \\ (c/\sqrt{\epsilon_\infty}) \hat{p}_z & 0 & 0 \\ i\omega_p/\sqrt{\epsilon_\infty} & 0 & -i\gamma \end{pmatrix}, \quad (5.33)$$

$$\begin{pmatrix} F_1 \\ F_2 \\ F_3 \end{pmatrix} = \begin{pmatrix} \sqrt{\epsilon_0 \epsilon_\infty} E_x(z, t) \\ \sqrt{\mu_0} H_y(z, t) \\ \frac{1}{\sqrt{\epsilon_0}} Q_x(z, t) \end{pmatrix}. \quad (5.34)$$

It is important to note that even after scaling, this matrix is not Hermitian due to the diagonal block containing  $-i\gamma$ .

As a substitute for the Lanczos algorithm of Section 4.1, we use the biorthogonal

Lanczos [79, 77] algorithm to handle the non-Hermiticity of the matrix  $\Omega$ ,

$$\mathbf{v}_1 = \mathbf{w}_1 = \mathbf{F}(t)/\|\mathbf{F}(t)\| \quad (5.35)$$

$$\mathbf{v}_{i+1} = (\Omega \cdot \mathbf{v}_i - \mathbf{v}_{i-1} \beta_{i-1} - \mathbf{v}_i \alpha_i)/\beta_i \quad (5.36)$$

$$\mathbf{w}_{i+1} = (\Omega^\dagger \cdot \mathbf{w}_i - \mathbf{w}_{i-1} \beta_{i-1}^* - \mathbf{w}_i \alpha_i^*)/\beta_i^* \quad (5.37)$$

where the  $\alpha_i = \mathbf{w}_i^\dagger \cdot \mathbf{H} \cdot \mathbf{v}_i$  and  $\beta_i = \sqrt{\mathbf{w}_{i+1}^\dagger \cdot \mathbf{v}_{i+1}}$  are complex and the tridiagonal matrix  $\mathbf{T}$  is complex symmetric. Even though there is an additional matrix-vector product per iteration, we choose this over the Arnoldi algorithm [69] which requires storage of all vectors. In addition to the arrays for past and future wave functions, the CSL algorithm minimally requires storage for two (four) additional vectors in the orthogonal (biorthogonal) case.

Since the CSL condition,  $a_n^L(\Delta t) = b_n^L(\Delta t)^*$ , does not hold in this case, it is instructive to investigate the difference of the CSL coefficients in terms of  $\mathbf{F}(t)$  propagated one time step in the forward and backward directions and the biorthogonal Lanczos basis,

$$a_n^L(\Delta t) - b_n^L(\Delta t)^* = \mathbf{w}_n^\dagger(t) \cdot e^{-i\Delta t \Omega} \cdot \mathbf{F}(t) - [\mathbf{w}_n^\dagger(t) \cdot e^{i\Delta t \Omega} \cdot \mathbf{F}(t)]^* \quad (5.38)$$

$$= \sum_{p=0}^{\infty} \frac{(-i\Delta t)^p}{p!} \left\{ \mathbf{w}_n^\dagger(t) \cdot \Omega^p \cdot \mathbf{F}(t) - [\mathbf{w}_n^\dagger(t) \cdot \Omega^p \cdot \mathbf{F}(t)]^* \right\}, \quad (5.39)$$

using the Taylor series representation of the exponential operators. The Krylov vectors generated by  $\Omega$  acting on  $\mathbf{F}(t)$  are simply linear combinations of the  $\mathbf{v}_m$  Lanczos



vectors,

$$\boldsymbol{\Omega}^p \cdot \mathbf{F}(t) = \|\mathbf{F}(t)\| \sum_{m=0}^p S_m^{(p)} \mathbf{v}_m(t) \quad (5.40)$$

where  $S_m^{(p)}$  are functions of the  $\alpha_n$  and  $\beta_n$  Lanczos coefficients and can be recursively calculated via the expression

$$S_m^{(p)} = \sum_{r=\max(m-1,0)}^{\min(m+1,p-1)} S_r^{(p-1)} T_{r+1,m+1} \quad (5.41)$$

for  $p \geq 2$  and  $0 \leq m \leq p$  with  $S_0^{(0)} = 1$ ,  $S_0^{(1)} = \alpha_1$ ,  $S_1^{(1)} = \beta_1$ , and  $T_{ij}$  as the  $(i, j)$  element of  $\mathbf{T}$ .

After inserting Eq. (5.40) into (5.39) and using the biorthogonality relationship,  $\mathbf{w}_n^\dagger(t) \cdot \mathbf{v}_m(t) = \delta_{mn}$ , the final expression for the needed correction takes the form

$$a_n^L(\Delta t) - b_n^L(\Delta t)^* = \|\mathbf{F}(t)\| (2i) \sum_{p=n}^{\infty} \frac{(-i\Delta t)^p}{p!} \text{Im}[S_n^{(p)}]. \quad (5.42)$$

Note that in the simple case of Hermitian  $\boldsymbol{\Omega}$ ,  $\alpha_n$  and  $\beta_n$  are real,  $\text{Im}[S_n^{(p)}] = 0$ , and the correction terms vanish in agreement with earlier results. Also, we see that the correction terms have leading behavior  $(\Delta t)^p$ ; thus, it is important to choose smaller time steps in order to reduce the number of correction terms needed to achieve a target accuracy level. The first two dominating terms at  $p = n$  and  $n + 1$  have simple expressions, i.e.,  $S_n^{(n)} = \prod_{j=1}^n \beta_j$  and  $S_n^{(n+1)} = (\prod_{j=1}^n \beta_j)(\sum_{k=1}^{n+1} \alpha_k)$ . The forms of higher  $p$  are more complicated and are best evaluated using the recursion relation

in Eq. (5.41).

To recap, the CSL algorithm is adjusted for the non-Hermitian case by using the biorthogonal Lanczos algorithm and adding correction terms to  $b_n^L(\Delta t)^*$  in order to calculate the proper  $a_n^L(\Delta t)$  coefficients of the vectors  $\mathbf{v}_n(t)$  in the composition of the future vector  $\mathbf{F}(t + \Delta t)$ . Depending on the number of correction terms used, there is a need to calculate  $\alpha_{n'}$  and  $\beta_{n'}$ , where  $n' > n$ . In other words, when calculating  $a_n^L(\Delta t)$ , one needs to go a few recursion steps ahead in the biorthogonal Lanczos algorithm in order to obtain the full set of  $\alpha_{n'}$  and  $\beta_{n'}$  coefficients needed to calculate  $S_n^{(p)}$  for  $p > n$ . In order to handle this requirement, one could either budget the time of computations by storing the higher order Lanczos vectors  $\mathbf{v}_{n'}$  calculated in conjunction with the  $\alpha_{n'}$  and  $\beta_{n'}$  factors for later use in the algorithm, or one could save memory at the expense of time by simply recalculating  $\mathbf{v}_n$  vectors as needed.

We specifically examine the case where one starts with a Gaussian pulse for the  $F_1$  and  $F_2$  fields ( $F_3 = 0$ ) as in Eq. (5.29) centered in a vacuum half-space ( $z > 0$ ) at  $z = 3D$  and impinging on a gold metal half-space ( $z < 0$ ) with the aforementioned Drude dielectric function (see Fig. 5.6). The quantities  $\epsilon_\infty$ ,  $\omega_p$ , and  $\gamma$  are independent of  $z$  in the gold half-space, but change discontinuously to, respectively, 1, 0, and 0 in vacuum. Due to this, one needs to be careful of the operational ordering of elements in Eq. (5.33), e.g., the (1,2) element of  $\mathbf{\Omega}$  is  $c\epsilon_\infty^{-1/2}(z)\hat{p}_z$  and the (2,1) element is  $c\hat{p}_z\epsilon_\infty^{-1/2}(z)$ . In the finite scaling function representation, these functions are represented as symmetric matrices with elements requiring twelve levels of refinement for a  $10^{-11}$  convergence. The matrix elements are trivial if either the bra or ket basis function does not include the gold-vacuum interface in its support. It is only the

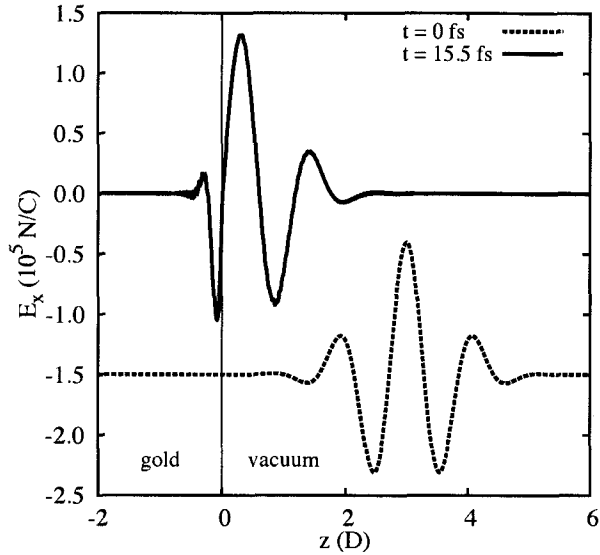


Figure 5.6: Gold-vacuum interface plot of  $\text{Re}(E_x(z, t))$  calculated by a Faber polynomial expansion. Two time snapshots are shown, the initial field curve at  $t = 0$  fs is offset for clarity. An  $L = 10$  symmet basis is used with 552 functions,  $k_{\min} = -160$ ,  $k_{\max} = 391$ , and  $\lambda = D/40$ , and  $\Delta t = 1/20$  fs.

$(L - 2) \times (L - 2)$  block where both supports include the interface that requires such extensive refinement if quadrature techniques are used. In the multiscale representation, whose use is postponed for future work, this means that only a small number of wavelets at each finer scale will be needed in order to much more efficiently represent effects of the discontinuity. In this initial investigation we are primarily interested in establishing whether or not errors can be systematically controlled in the presence of both attenuation and dielectric discontinuities.

Figure 5.6 shows the pulse initially in vacuum and later as it impinges on the gold half-space. Figure 5.7 tracks the maximum absolute error in a 35 fs time period of the CSL algorithm with a varying number of correction terms compared to a Faber polynomial expansion run ( $n_{\max} = 15$ ) converged to the precision limit of  $10^{-16}$ . As pointed out by Huang et al. [78], the Faber method reduces to the Chebyshev

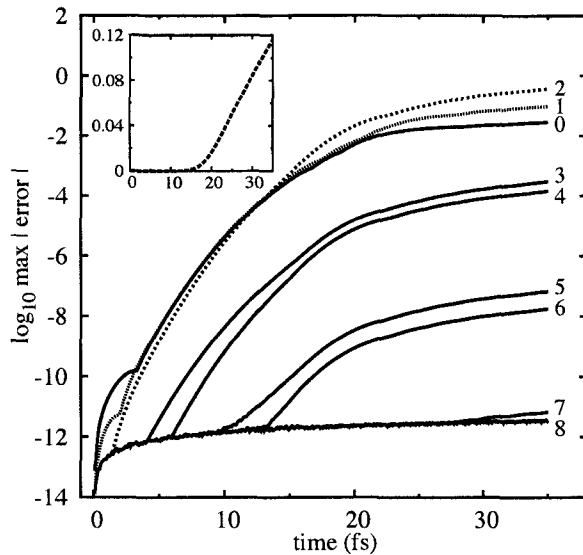


Figure 5.7: Maximum errors in vacuum-gold pulse propagation over time using the adjusted CSL algorithm. Each plot is labeled on the right with a value corresponding to the number of correction terms defined in Eq. (5.42). The inset shows the attenuation measured by the decrease in norm of  $\mathbf{F}(t)$  over the same time period. An  $L = 10$  symmlet basis is used with 272 functions,  $k_{\min} = -80$ ,  $k_{\max} = 191$ ,  $\lambda = D/20$ , and  $\Delta t = 1/20$  fs.

method of Eq. (5.16) with the difference that  $E_{av}$  and  $E_{hw}$  are calculated such that the spectrum of the scaled and shifted matrix  $\mathbf{H}'$  falls within a unit circle on the complex plane. It is seen that the non-Hermiticity corrections provide a systematic means to decrease error over the course of many time steps. However, for a fixed number of correction terms, there is ultimately a sharp transition to higher disagreement, and the time for this transition is longer for a higher number of corrections terms. By way of contrast, propagation strictly within gold metal produces differences that follow the same patterns at longer times (the maximum absolute error is always found on the gold side in the interface problem), but that do not exhibit the sharp transitions for any correction order. It therefore appears that the cumulative error at long times is dominated by the non-Hermitian nature of the operator, while the clear transitions

are attributable to the presence of the interface before the cumulative differences due to non-Hermiticity are reached. It is interesting that the even correction orders appear to contribute little, though the reasons for this are as yet unclear.

Sharp interfaces provide problems in all EM computational methods. In the Finite-difference Time-domain method, subgridding techniques are used to provide greater accuracy at the expense of increased computational effort [71]. In the alternative Pseudospectral Time-domain method [71], implemented using either Fourier or Chebyshev basis functions, one is handicapped by Gibbs phenomena. Borisov and Shabanov obtain greater accuracy using nonlinear coordinate transformation to increase the sampling density near the interface [80]. Min, et al., approach this problem using Gegenbauer reconstruction [81] to eliminate the Gibbs oscillations. Wavelet bases are also not exempt from Gibbs oscillations, but allow for facile multi-scale extension of the basis tailored specifically to the immediate neighborhood of the interface. This useful aspect of wavelets underlies the development of the Multiresolution Time-domain method in electromagnetics [82], complementary to the spectral methods pursued here (see also, e.g., Fujii and Hoefer [83]).

## 5.5 Summary

This chapter has introduced a simple low-order polynomial propagation method for the solution  $\mathbf{y}(t)$  of the TDSE with a time-independent Hamiltonian. It has been determined analytically and numerically that the projection coefficients of  $\mathbf{y}(t \pm \Delta t)$  on the Lanczos basis formed from  $\mathbf{y}(t)$  are (1) simple complex conjugates of each

other and (2) independent of  $t$ . This has allowed use of the CSL propagation method, which proceeds through matrix-vector and vector inner products. One avoids direct calculation of the matrix exponential propagation operator and requires low storage in the basic form of the method. A wavelet primitive basis has been used, but the CSL method does not depend on this. Careful examination of the errors were made and it was detailed precisely how these depend on the approximation order of the wavelet families used.

Simple EM applications were also considered by virtue of the ability to put Maxwell's Equations in Hamiltonian form. In view of the importance of absorbing materials, complex dielectric functions and propagators involving non-Hermitian matrices were then considered. A first scheme for CSL corrections due to non-Hermiticity was developed and applied in the case of a pulse encountering a gold-vacuum planar interface. This leads to increases in either computation or storage requirements. While these are modest, it is desirable to minimize these increases, and this will be the subject of future investigations.

## **Part II**

# **SEROA: Surface-Enhanced Raman Optical Activity**

There is great interest today in nanophotonics, i.e., manipulation of light by particles and structures of sub-wavelength dimensions. One of the important applications is the enhancement of Raman scattering by molecules on or near noble metal nanoparticles. The strong local EM fields near silver and gold nano-spheres, shells, rods, and other particles are in large part the reason for the strong increases in signal, giving rise to SERS and less-developed variants such as SEROA. SEROA measurements have been made and published, but there is much uncertainty about how to interpret the results and whether or not it can even in principle be implemented as a spectroscopy selective for chiral molecules as is true for ROA. This chapter is concerned with theoretical confirmation of a first scenario where chiral selectivity of SEROA is indeed expected.

In the long run, we expect wavelets to be useful for calculation of near fields for nanoparticles supporting surface plasmons and needing different levels of resolution. For the time being, the questions about SEROA practicality are of their own interest and we consider the use of highly symmetric spherical metal nanoshells. These have been the focus of much work from the groups of Naomi Halas, Peter Nordlander, and others at Rice University, and they have the merit that the EM fields and light-scattering properties can be calculated using Mie theory. Wavelet approaches are therefore not needed here, and the wavelet (Part I) and surface-enhancement (Part II) calculations of this thesis are completely distinct for now. Chronologically, the contents of this chapter run in parallel with the work described in Chapters 2–5.

This work is joint with Richard Lombardini, published in papers by Acevedo, et al. [84] and Lombardini, et al. [85].



## Chapter 6

### SEROA

#### 6.1 Introduction

Metal nanoparticles supporting surface plasmon modes of the conduction electrons are capable of strongly modifying the spectroscopy of attached or nearby molecules. A leading example is surface-enhanced Raman scattering (SERS) [86, 87, 88, 89], for which the Raman cross-section is typically several orders of magnitude higher than in the absence of the plasmonic particle. This enhances the usefulness of Raman scattering as a vibrational spectroscopy, e.g., for chemical and biomolecule analysis and sensing [90, 91]. Raman optical activity (ROA) [92, 93], which is exhibited in differences between right- and left-circularly-polarized Raman-scattering intensities, provides a spectroscopy that is sensitive to chirality in molecules and that would similarly benefit from development of a surface-enhanced Raman optical activity (SEROA) [94, 95, 96, 97, 98, 99, 100, 101, 102, 103, 104, 105, 106, 107]. However, ROA depends on subtle interplay between the electric dipole ( $E1$ ) moment of the molecule and its magnetic dipole ( $M1$ ) and electric quadrupole ( $E2$ ) moments, and much work will be needed to understand precisely how this interplay is affected by the strong local EM fields near nanoparticles of silver, gold, and other metals.

Here this question is examined in detail for the particular situation of chiral molecules moving near spherical metal nanoshells with dielectric cores [108]. For such a scenario, it is possible to extend and merge the classical-fields model of SERS by Kerker, Wang and Chew (KWC) [109] and the off-resonant formalism for ROA by Barron and Buckingham [92]. The resulting formalism, developed here, allows prediction of SEROA circular intensity differences (CIDs) and their enhancements as functions of excitation frequency in terms of the dynamic ROA response tensors. In conjunction with a recent chiroptical orbital model [110], it is also shown to allow an investigation of particular circumstances where SEROA retains the selectivity of ROA to molecules with chiral symmetry. A schematic of a typical dual circular polarization SEROA experiment is shown in Fig. 6.1.

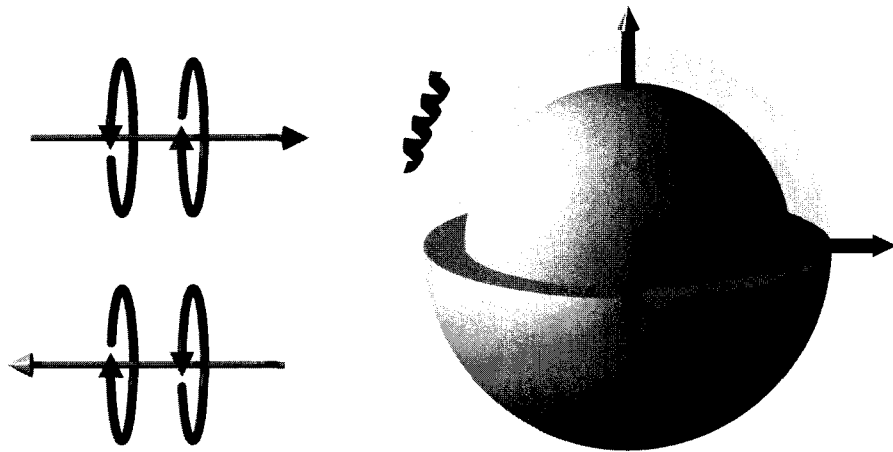


Figure 6.1: Schematic of SEROA experiments considered here. Chiral molecules in the electromagnetic enhancement range of a metal nanoshell with a dielectric core are probed, modulating between circular polarization senses for incident and/or scattered light in backscattering. Red = right-handed and Blue = left-handed.

Different SEROA variations are possible depending on the polarizations of incident and analyzed scattered light. The possibilities are termed incident circular po-

larization (ICP), scattered circular polarization (SCP), and two forms of dual circular polarization (DCP), in analogy to ROA terminology. These polarization schemes are discussed below and it is found that chiral selectivity is predicted for SCP (or ICP) only if one averages over molecular rotations and over an ensemble of molecules surrounding the particle. Rotational averaging alone appears sufficient in DCP SEROA for our simple scenario of a spherical substrate and far-from-resonance excitation, a finding potentially important for carrying SEROA to lower analyte concentrations. Even though the laser frequency is assumed to be far-from-resonance with molecular transitions, it can in general be very close to resonance with surface plasmon modes. Ag and Au nanoshell excitation profiles are investigated throughout the visible spectrum for two different forms of DCP polarization experiments. Excitation of both dipole and quadrupole plasmon modes are investigated, and it is delineated how total and differential scattering depend in those cases on the polar angle of the molecule relative to the incident beam direction. We end with concrete suggestions for excitation strategies appropriate to this type of SEROA experiment.

## 6.2 Ordinary and Surface-Enhanced Raman Optical Activity

### 6.2.1 Ordinary ROA

Assuming a monochromatic EM field of frequency  $\omega_0$  in spectral regions where the molecule is transparent, the description of ordinary non-resonant ROA uses the complex induced  $E1$ ,  $M1$ ,  $E2$  multipole moments (electric dipole  $\mathbf{d}$ , magnetic dipole  $\mathbf{m}$ ,

electric quadrupole  $\Theta$ ) of the molecule [92, 111]

$$d_j = \alpha_{jk} E_k + G_{jk} B_k + \frac{1}{3} A_{jkl} \frac{\partial}{\partial x_k} E_l + \dots \quad (6.1)$$

$$m_j = G_{kj}^* E_k + \dots \quad (6.2)$$

$$\Theta_{jk} = A_{ljk}^* E_l + \dots \quad (6.3)$$

(See Eqs. (2.6.34) of Barron [111], where tildes are used to distinguish these generally complex quantities.) A repeated index summation convention is used in Eqs. (6.1)–(6.3), and MKS units are employed throughout. The  $\alpha_{jk}$  are elements of the electric dipole-electric dipole polarizability tensor  $\alpha$ , the  $G_{jk}$  are those of the electric dipole-magnetic dipole optical activity tensor  $\mathbf{G}$ , and the  $A_{jkl}$  are those of the electric dipole-electric quadrupole optical activity tensor  $\mathbf{A}$ . If the wave functions may be taken as real, then  $\alpha$  and  $\mathbf{A}$  are real and  $\mathbf{G} = -i\mathbf{G}'$  is imaginary [112]. The incident electric field  $\mathbf{E}$  and magnetic field  $\mathbf{B}$  both depend on frequency  $\omega_0$  and position  $\mathbf{r}$ , this dependence being simplest in the case of a plane wave. It is assumed that these fields correspond to  $e^{-i\omega_0 t}$  time behavior.

In a classical field picture, the molecule supports radiating  $E1$ ,  $M1$ ,  $E2$  multipole fields [113] that, for Raman scattering, oscillate at a frequency  $\omega$  shifted from  $\omega_0$  by a vibrational quantum. Thus, for example, there is an EM field with vectors  $\mathbf{E}^{(E1)}(\omega, \mathbf{r})$ ,  $\mathbf{B}^{(E1)}(\omega, \mathbf{r})$  generated from  $\mathbf{d}$ , as well as corresponding fields generated by  $\mathbf{m}$  and the electric quadrupole tensor. These are detailed by Jackson [113], who uses a quadrupole tensor  $\mathbf{Q}$  that is twice the tensor  $\Theta$  used by Barron and Buckingham [92].

In the electric dipole approximation, only  $\mathbf{d}$  is considered and only the  $\alpha \cdot \mathbf{E}$  con-

tribution to it in Eq. (6.1) is included. For ROA, however, it is necessary to include the other contributions to  $\mathbf{d}$  shown in Eq. (6.1) and to include the other radiating multipole fields, with induced moments calculated at least through the leading electric field contributions. If the oscillating moments are regarded quantum mechanically, time-dependent perturbation-theory yields sum-over-intermediate-states forms for all of the response tensors [92]. These involve products of absorption and emission transition matrix elements (in off-resonant virtual-state terminology), and those where both matrix elements are of the electric dipole operator ( $\alpha$ ) dominate the total intensities.

The different polarization schemes introduced earlier are depicted in Fig. 6.2. Each

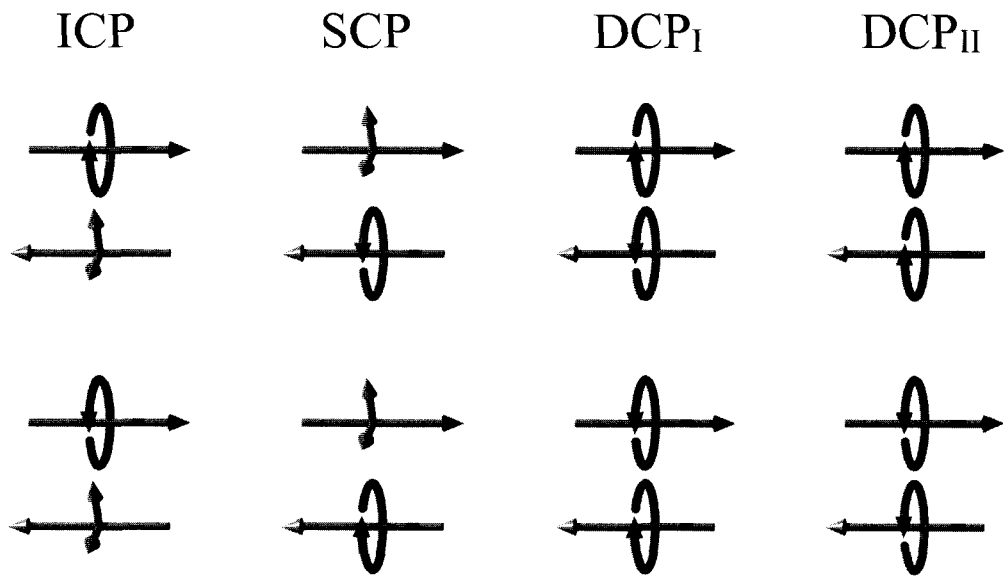


Figure 6.2: Polarization of incident and scattered light in Fig. 6.1 for different circular polarization ROA/SEROA experiments. Linearly- or un-polarized light is measured in scattering for ICP and is used in incidence for SCP experiments. Intensity sums and differences in each case are formed between the top and bottom scattering processes shown.

these schemes are applicable in both ROA and SEROA cases. The intensities can be

calculated from components of the (cycle-averaged) Poynting vector,

$$\mathbf{S} = \frac{1}{2\mu_0} \text{Re}(\mathbf{E}_{\text{rad}} \times \mathbf{B}_{\text{rad}}^*) \quad (6.4)$$

where

$$\mathbf{E}_{\text{rad}} = \mathbf{E}^{(E1)} + \mathbf{E}^{(M1)} + \mathbf{E}^{(E2)} + \dots \quad (6.5)$$

and similarly for  $\mathbf{B}_{\text{rad}}$ . Here  $\mu_0$  is the free-space magnetic permeability. Barron and Buckingham derived explicit expressions for intensity differences with plane-wave excitation using the asymptotic forms for the fields [92]. For example, with an initial CW field of amplitude  $E_0$  propagating along  $z$  and having either right or left circular polarization vectors  $(\hat{x} \mp i \hat{y})/\sqrt{2}$ , the ICP difference in  $x$ -polarized Rayleigh intensities detected at distance  $r$  along  $y$  is calculated to leading orders as

$$S_x^R - S_x^L = \frac{\omega_0^4 \mu_0 E_0^2}{16\pi^2 c^2 r^2} \left\langle \text{Im}(c \alpha_{xy} \alpha_{xx}^* + \alpha_{xy} G_{xy}^* + \alpha_{xx} G_{xx}^* + \alpha_{xy} G_{xz}^* - \alpha_{xx} G_{yz}^*) \right. \\ \left. + \frac{\omega_0}{3} \text{Re}(\alpha_{xx} A_{xzy}^* - \alpha_{xy} A_{xzx}^* + \alpha_{xy} A_{xxy}^* - \alpha_{xx} A_{yxy}^*) \right\rangle, \quad (6.6)$$

where  $c$  is the speed of light. The angular brackets indicate orientational averaging, appropriate for randomly oriented molecules in gas or solution phase. The averaging is accomplished by standard integration of products of direction cosine matrix elements, and leads to vanishing of any “ $\alpha\alpha$ ” contributions (i.e., averages over products of  $\alpha$  tensor elements) to intensity differences. However, nonzero  $\alpha G$  and  $\alpha A$  contributions are still obtained for molecules that have chiral symmetry. These are typically  $10^{-3}$ – $10^{-5}$  times the total (non-differential) intensity [100], requiring long ROA data

acquisition times.

Luber, et al. [114], have recently reviewed earlier investigations of the relative sizes of the  $\alpha G$  and  $\alpha A$  cross terms in unenhanced ROA and performed a density functional theory analysis across a series of organic compounds including alkanes, alkenes, amino acids and larger peptides. With exceptions of certain C-H stretching modes, the calculated ROA spectra were little-changed when the  $\alpha A$  terms were neglected. These are the most difficult terms to calculate, so neglecting them would simplify *ab initio* spectral simulations of ordinary ROA.

### 6.2.2 Surface-Enhanced ROA

In the presence of a metal nanoparticle supporting surface plasmons, the situation changes considerably. Even if the molecule is not in direct contact, local field enhancements strongly modify the Raman scattering and must be included in the scattering formalism. For the simplest case of spherical metal particles in the electric dipole approximation, this has been accomplished in the Mie theory investigation by KWC [109]. First, the induced dipole is calculated as  $\mathbf{d} = \boldsymbol{\alpha} \cdot (\mathbf{E} + \mathbf{E}_s) = \boldsymbol{\alpha} \cdot \mathbf{E}_t$  where  $\mathbf{E}_s$  is the wave produced when the plane wave  $\mathbf{E}$  scatters from the nanoparticle. The resulting dipole  $\mathbf{d}$  then emits an electric field  $\mathbf{E}^{(E1)}$  that can be associated with a classical electric dipole oscillating at the Raman-shifted frequency  $\omega$ . This field also scatters from the nanoparticle and produces the field  $\mathbf{E}_s^{(E1)}$ . The total Raman-shifted field intensity observed at position  $\mathbf{r}$  is then proportional to  $|\mathbf{E}^{(E1)}(\mathbf{r}) + \mathbf{E}_s^{(E1)}(\mathbf{r})|^2$ .

The overall picture with higher molecular multipoles in the presence of the plasmonic nanoparticle is the following. An incident plane wave field  $\mathbf{E}$  of frequency

$\omega_0$  scatters from the nanoparticle, producing another field  $\mathbf{E}_s$ . The nearby molecule is thus exposed to a total local field  $\mathbf{E}_t = \mathbf{E} + \mathbf{E}_s$  which induces oscillation of the molecular multipoles at the Raman-shifted frequency  $\omega$ . The resulting  $E1$ ,  $M1$ , and  $E2$  fields  $\mathbf{E}^{(E1)}$ ,  $\mathbf{E}^{(M1)}$ , and  $\mathbf{E}^{(E2)}$ , respectively, each also scatter off the nanoparticle. Thus, the total radiative field reaching the detector is  $\mathbf{E}_{\text{rad},t} = \mathbf{E}_t^{(E1)} + \mathbf{E}_t^{(M1)} + \mathbf{E}_t^{(E2)}$ , where, e.g.,  $\mathbf{E}_t^{(E1)} = \mathbf{E}^{(E1)} + \mathbf{E}_s^{(E1)}$ . Each of the electric fields naturally has an accompanying magnetic field. An example, where a molecule lies on the  $y$  axis outside a spherical metal particle, is shown schematically in Fig. 6.3.

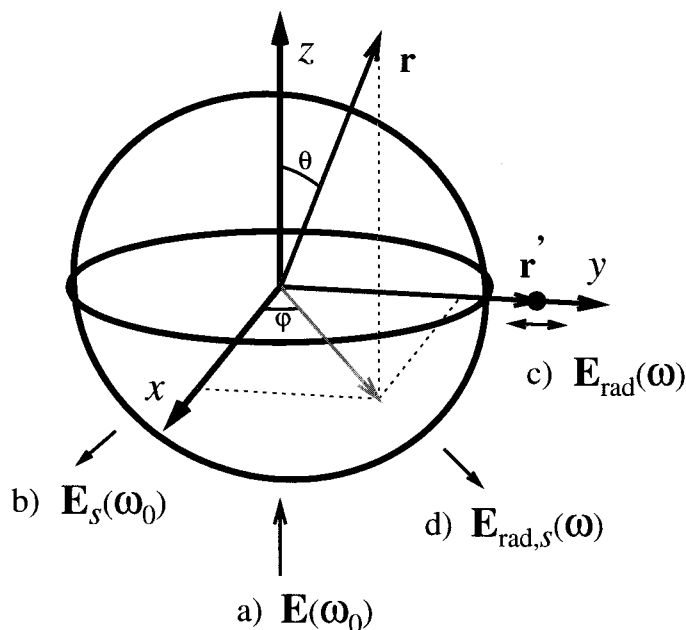


Figure 6.3: A molecule at position  $\mathbf{r}'$  outside a metal nanoparticle centered at the origin is exposed to a) an external plane-wave field and b) its wave scattered from the particle, both at frequency  $\omega_0$ . Molecular multipole moments are then induced corresponding to c) a composite field radiating from the molecule and d) a secondary field scattered from the particle, both at Raman-shifted frequency  $\omega$ . Both c) and d) can be broken into  $E1$ ,  $M1$ , and  $E2$  parts as  $\mathbf{E}_{\text{rad}} = \mathbf{E}^{(E1)} + \mathbf{E}^{(M1)} + \mathbf{E}^{(E2)}$  and  $\mathbf{E}_{\text{rad},s} = \mathbf{E}_s^{(E1)} + \mathbf{E}_s^{(M1)} + \mathbf{E}_s^{(E2)}$  with  $\mathbf{E}_{\text{rad},t} = \mathbf{E}_{\text{rad}} + \mathbf{E}_{\text{rad},s}$ .

Explicitly, the KWC generalization is (the symbol  $:$  is used for double tensor



contraction)

$$\mathbf{d} = \boldsymbol{\alpha} \cdot (\mathbf{E} + \mathbf{E}_s) + \mathbf{G} \cdot (\mathbf{B} + \mathbf{B}_s) + \frac{1}{3} \mathbf{A} : \boldsymbol{\nabla}(\mathbf{E} + \mathbf{E}_s) + \dots \quad (6.7)$$

$$\mathbf{m} = (\mathbf{E} + \mathbf{E}_s) \cdot \mathbf{G}^* + \dots \quad (6.8)$$

$$\mathbf{Q} = 2(\mathbf{E} + \mathbf{E}_s) \cdot \mathbf{A}^* + \dots \quad (6.9)$$

$$\mathbf{E}_{\text{rad},t} = \mathbf{E}^{(E1)} + \mathbf{E}_s^{(E1)} + \mathbf{E}^{(M1)} + \mathbf{E}_s^{(M1)} + \mathbf{E}^{(E2)} + \mathbf{E}_s^{(E2)} + \dots \quad (6.10)$$

$$\mathbf{B}_{\text{rad},t} = \mathbf{B}^{(E1)} + \mathbf{B}_s^{(E1)} + \mathbf{B}^{(M1)} + \mathbf{B}_s^{(M1)} + \mathbf{B}^{(E2)} + \mathbf{B}_s^{(E2)} + \dots \quad (6.11)$$

Similarly to Eq. (6.4), the Poynting vector is then calculated as  $\mathbf{S} = \text{Re}(\mathbf{E}_{\text{rad},t} \times \mathbf{B}_{\text{rad},t}^*)/2\mu_0$ . Out of this expression, there will be leading terms that can again be identified as  $\alpha\alpha$ ,  $\alpha G$  and  $\alpha A$ . Their coefficients will be different than for ROA, however.

In terms of the electromagnetic picture, there are two related types of enhancement mechanisms. First, the induced multipole moments are increased due to the addition of strong scattered local fields and gradients. The radiating fields are increased by this effect and further increased by their own scattering from the nanoparticle. Within the electric dipole approximation for SERS, it turns out that the enhancement is roughly a product of factors that are  $g^2(\omega_0) g^2(\omega)$  evaluated at the laser and Raman-shifted frequencies [109]. When more molecular multipoles are included, the extra intensity terms containing them may each exhibit their own enhancement curves, and it becomes necessary to develop further extensions of the KWC vector spherical harmonic field calculations.

### 6.3 Mie Theory for EM Scattering Problems:

#### Plane Wave Scattering

The three-component functions used for solution of the vector Helmholtz equation with spherical symmetry are denoted  $\mathbf{L}_{\sigma lm}^z$ ,  $\mathbf{M}_{\sigma lm}^z$ , and  $\mathbf{N}_{\sigma lm}^z$ . The  $\mathbf{L}_{\sigma lm}^z$  are not required for a solenoidal (divergenceless) electromagnetic field [115, 116, 117]. In spherical coordinates  $r, \theta, \phi$ , the other functions are

$$\mathbf{M}_{\sigma lm}^z(k \mathbf{r}) = \hat{\theta} m z_l(k r) \frac{P_l^m(\cos \theta)}{\sin \theta} \begin{pmatrix} -\sin m\phi \\ \cos m\phi \end{pmatrix} - \hat{\phi} z_l(k r) \frac{dP_l^m(\cos \theta)}{d\theta} \begin{pmatrix} \cos m\phi \\ \sin m\phi \end{pmatrix} \quad (6.12)$$

$$\begin{aligned} \mathbf{N}_{\sigma lm}^z(k \mathbf{r}) = & \hat{r} l(l+1) \frac{z_l(k r)}{k r} P_l^m(\cos \theta) \begin{pmatrix} \cos m\phi \\ \sin m\phi \end{pmatrix} + \hat{\theta} \eta_l^z(k r) \frac{dP_l^m(\cos \theta)}{d\theta} \begin{pmatrix} \cos m\phi \\ \sin m\phi \end{pmatrix} \\ & + \hat{\phi} m \eta_l^z(k r) \frac{P_l^m(\cos \theta)}{\sin \theta} \begin{pmatrix} -\sin m\phi \\ \cos m\phi \end{pmatrix} \end{aligned} \quad (6.13)$$

The index  $\sigma = e$  or  $o$ , according to whether, respectively, the upper or lower function of  $\phi$  is used. The associated Legendre polynomials  $P_l^m(\cos \theta)$  are chosen with the Condon-Shortley phase choice. The superscript  $z = j$  if  $z_l(k r) = j_l(k r)$  and  $z = h$  if  $z_l(k r) = h_l^{(1)}(k r)$ , corresponding to spherical Bessel functions regular at the origin and to outgoing spherical Hankel functions, respectively. The remaining radial functions are  $\eta_l^z(x) = [x z_l(x)]'/x$ , where the prime indicates differentiation with respect to  $x$ .

Let us assume that a CW laser field  $\mathbf{E}$  with frequency  $\omega_0$ , wavenumber  $k_0$  and wavelength  $\lambda_0$  is incident on a nanosphere centered on the origin. If the surrounding

medium has refractive index  $n$ , then  $\omega_0 = k_0 c/n = 2\pi c/(n\lambda_0)$ . Specifying that  $\mathbf{E}$  corresponds to  $e^{-i\omega_0 t}$  time-dependence, propagation is along the  $z$ -axis and polarization is along the  $x$ -axis, then [115]

$$\mathbf{E}(\mathbf{r}) = E_0 \hat{x} e^{ik_0 z} = E_0 \sum_{l=1}^{\infty} i^{l+2} \frac{2l+1}{l(l+1)} [\mathbf{M}_{ol1}^j(k_0 \mathbf{r}) - i \mathbf{N}_{el1}^j(k_0 \mathbf{r})] . \quad (6.14)$$

Similar expansions hold for internal nanoparticle fields and scattered external fields, all of which must be matched at the particle surface. For the scattered field, this leads to

$$\mathbf{E}_s(\mathbf{r}) = E_0 \sum_{l=1}^{\infty} i^{l+2} \frac{2l+1}{l(l+1)} [a_l(\omega_0) \mathbf{M}_{ol1}^h(k_0 \mathbf{r}) - i b_l(\omega_0) \mathbf{N}_{el1}^h(k_0 \mathbf{r})] , \quad (6.15)$$

where  $a_l(\omega_0)$  and  $b_l(\omega_0)$  are well-known Mie coefficients involving the permittivities of the nanosphere and the medium [118, 116, 117]. The expansions for other initial polarizations (e.g., along the  $y$ -axis) will also involve the other vector functions  $\mathbf{M}_{el1}^z(k_0 \mathbf{r})$  and  $\mathbf{N}_{ol1}^z(k_0 \mathbf{r})$ .

If the nanoparticle is instead a metal nanoshell with a dielectric material core, the complete solution requires coefficient matching at both inner and outer surfaces using different expansions in each region. However, the expansion basis in the external region is the same as for a nanosphere, and only the explicit forms for the Mie coefficients  $a_l$  and  $b_l$  differ [119]. For scattering with molecules external to the nanoparticle, it is only this external field that is needed. In everything that follows we use the more versatile nanoshell geometry with its tunable surface plasmons for

purposes of generality, and solid nanospheres are regarded as the special case where the dielectric core vanishes.

In the Mie theory literature, the nanoparticle field contributions for  $l = 1, 2, 3, \dots$  are called dipole, quadrupole, octupole,  $\dots$  modes, respectively. These are not to be confused with the molecular multipole moments of the same names that are the focus here. Nevertheless, all nanoparticle-multipole terms, as well as all orders of retardation (i.e., effects due to the finite speed of light), are included in the calculations.

The other expansions required in Eq. (6.7) are the magnetic field  $\mathbf{B}$  and the outer product  $\nabla\mathbf{E}$  (a two-dimensional tensor). The  $\mathbf{B}$  expansion is easily obtained by using  $i\omega_0\mathbf{B} = \nabla \times \mathbf{E}$  and the curl equations [116],

$$\nabla \times \mathbf{M}_{\sigma lm}^z = k_0 \mathbf{N}_{\sigma lm}^z \quad \nabla \times \mathbf{N}_{\sigma lm}^z = k_0 \mathbf{M}_{\sigma lm}^z . \quad (6.16)$$

For fields evaluated at the Raman frequency these same relations hold but with  $\omega$  and  $k$  instead of  $\omega_0$  and  $k_0$ . The  $\nabla\mathbf{E}$  expansion has also been implemented in spherical coordinates, though these terms need to be grouped carefully so that apparent singularities at  $\theta = 0$  or  $\pi$  cancel properly, and is converted to Cartesian coordinates as needed.

The incident plane wave field  $\mathbf{E}$  and the scattered field  $\mathbf{E}_s$  both co-exist outside the particle, as do their magnetic field and gradient field counterparts (not indicated). Focusing on the induced electric dipole of Eq. (6.7) in the electric dipole approximation, the magnitude of  $\mathbf{d}$  is determined by  $\mathbf{E} + \mathbf{E}_s$  at the position  $\mathbf{r}'$  of the molecule. As a general measure of the transition intensity, independent of the specific choice of

polarizability tensor, the quantity  $|\mathbf{E} + \mathbf{E}_s|^2/|\mathbf{E}|^2$  is shown as a function of wavelength for a 40/50 nm (inner/outer radius) silver nanoshell in Fig. 6.4 for two different initial polarizations and for the molecule outside the outer shell surface. Also shown

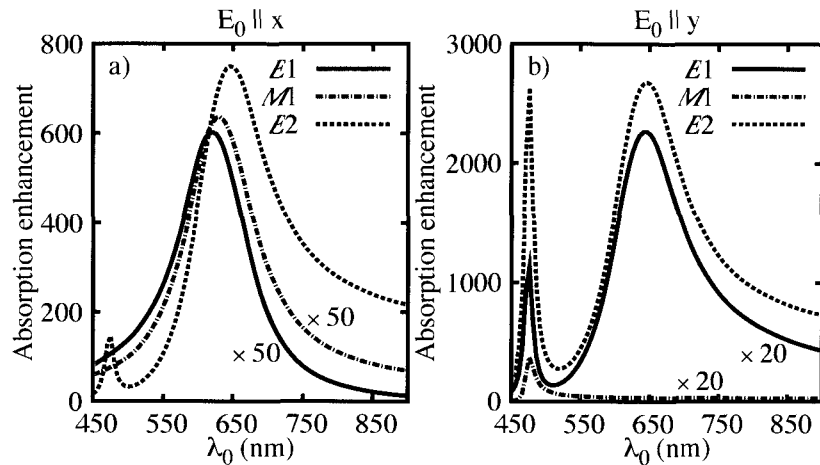


Figure 6.4: Enhancement factors for incident fields involved in absorption by a 40/50 nm silver nanoshell. Here  $|\mathbf{E} + \mathbf{E}_s|^2/|\mathbf{E}|^2$ ,  $|\mathbf{B} + \mathbf{B}_s|^2/|\mathbf{B}|^2$ , and  $|\nabla\mathbf{E} + \nabla\mathbf{E}_s|^2/|\nabla\mathbf{E}|^2$  are shown to each have their own enhancement curves as functions of wavelength and of initial polarization. The incident electric field  $\mathbf{E}$  is along the  $x$  axis in a) and along the  $y$  axis in b). Fields are evaluated at the molecular position  $\mathbf{r}'$  1 nm outside the nanoshell along the  $y$  axis.

are corresponding factors for magnetic dipole and electric quadrupole transitions,  $|\mathbf{B} + \mathbf{B}_s|^2/|\mathbf{B}|^2$  and  $|\nabla\mathbf{E} + \nabla\mathbf{E}_s|^2/|\nabla\mathbf{E}|^2$ , where the latter square norm is a summation over the absolute-squares of the components of the gradient tensor. These represent generalized enhancement plots for the different pure-multipole absorption transitions.

The broader long-wavelength resonance features in Fig. 6.4 correspond to  $l = 1$  (nanoparticle-dipole) contributions in Eqs. (6.14) and (6.15), while the narrower short-wavelength features correspond to  $l = 2$  (nanoparticle-quadrupole). It is seen that these enhancements are generally greater for polarization in the direction of

the molecule ( $y$  polarization here), and that the molecular  $E2$  enhancements are the strongest. The  $M1$  enhancements are the smallest, though they can be comparable to the  $E1$  enhancements in some cases. These conclusions continue to hold upon examining other geometries and polarizations. The dynamic variation of the local fields is sufficiently strong that the electric field gradient, and hence the  $E2$  response tensor  $\mathbf{A}$ , becomes a more significant contributor to scattering than in the absence of the nanoparticle [cf., Eq. (6.7)].

For the  $\alpha G$  and  $\alpha A$  terms, this examination is only half the story. There are similar cross-terms whether it is the absorption step or the emission step that is  $E1$ , and we have so far only discussed the case corresponding to  $E1$  emission. Equations (6.8) and (6.9) are pertinent to establishing  $M1$  and  $E2$  radiating fields due to  $E1$  absorption. Will the resulting cross-terms have similar enhancement curves in these separate cases? The direct way to answer this requires evaluation of these higher multipole fields, the task to which we turn next.

## 6.4 Multipole Field Scattering

### 6.4.1 Field Expansions from the Dyadic Green Tensor

The classical EM fields observed at  $\mathbf{r}$  due to molecular multipole moments at  $\mathbf{r}'$  may be derived by using the dyadic electromagnetic Green tensor [109, 120, 121]. Solutions of the full scattering problem were detailed in Acevedo, et al. [84]. The final forms are given here.

Each of the primary molecular multipole fields produces a field scattered from

the nanoparticle, so that the total fields at the Raman-shifted frequency are each a sum of primary and scattered contributions. To determine the scattered fields, one may match tangential electric and magnetic field components at the shell boundaries in Mie-type calculations. For determination of the radiation in the far zone, we are interested in the region  $r > r'$ . The total  $E1$  electric field is

$$\mathbf{E}_t^{(E1)}(\mathbf{r}) = \frac{i k^3}{\pi \varepsilon \varepsilon_0} \sum_{\sigma=e}^o \sum_{l=1}^{\infty} \sum_{m=0}^l D_{lm} \left[ \mathbf{M}_{\sigma lm}^h(k \mathbf{r}) f_{\sigma lm}^{(E1,t)} + \mathbf{N}_{\sigma lm}^h(k \mathbf{r}) g_{\sigma lm}^{(E1,t)} \right] \quad (6.17)$$

$$f_{\sigma lm}^{(E1,t)} = \mathbf{M}_{\sigma lm}^j(k \mathbf{r}') \cdot \mathbf{d} + a_l(\omega) \mathbf{M}_{\sigma lm}^h(k \mathbf{r}') \cdot \mathbf{d} \quad (6.18)$$

$$g_{\sigma lm}^{(E1,t)} = \mathbf{N}_{\sigma lm}^j(k \mathbf{r}') \cdot \mathbf{d} + b_l(\omega) \mathbf{N}_{\sigma lm}^h(k \mathbf{r}') \cdot \mathbf{d} \quad (6.19)$$

where  $D_{lm} = (2 - \delta_{m0}) \frac{2l+1}{4l(l+1)} \frac{(l-m)!}{(l+m)!}$  and the  $a_l(\omega)$  and  $b_l(\omega)$  coefficients are precisely the same Mie coefficients as in Eq. (6.15) but evaluated at the Raman-shifted frequency  $\omega$ . Of special note is the fact that they are not dependent on  $m$ . The free-space electric permittivity  $\varepsilon_0$  and magnetic permeability  $\mu_0$  satisfy  $1/c = \sqrt{\varepsilon_0 \mu_0}$ . The corresponding quantities in a general material are taken to be  $\varepsilon \varepsilon_0$  and  $\mu \mu_0$ , where the relative permittivity  $\varepsilon$  and permeability  $\mu$  satisfy  $\sqrt{\varepsilon \mu} = k c / \omega = n$ , with  $k$  the wavenumber and  $n$  the index of refraction at the Raman-shifted frequency  $\omega = k c / n = 2\pi c / (n\lambda)$ . The index of refraction is generally complex for absorbing materials. Only non-magnetic materials ( $\mu = 1$ ) are considered below.

Similarly, the total  $M1$  electric field is

$$\mathbf{E}_t^{(M1)}(\mathbf{r}) = -\frac{k^3 c \mu \mu_0}{\pi n} \sum_{\sigma=e}^o \sum_{l=1}^{\infty} \sum_{m=0}^l D_{lm} \left[ \mathbf{N}_{\sigma lm}^h(k \mathbf{r}) f_{\sigma lm}^{(M1,t)} + \mathbf{M}_{\sigma lm}^h(k \mathbf{r}) g_{\sigma lm}^{(M1,t)} \right] \quad (6.20)$$

$$f_{\sigma lm}^{(M1,t)} = \mathbf{M}_{\sigma lm}^j(k \mathbf{r}') \cdot \mathbf{m} + b_l(\omega) \mathbf{M}_{\sigma lm}^h(k \mathbf{r}') \cdot \mathbf{m} \quad (6.21)$$

$$g_{\sigma lm}^{(M1,t)} = \mathbf{N}_{\sigma lm}^j(k \mathbf{r}') \cdot \mathbf{m} + a_l(\omega) \mathbf{N}_{\sigma lm}^h(k \mathbf{r}') \cdot \mathbf{m} \quad (6.22)$$

and the total  $E2$  electric field is

$$\mathbf{E}_t^{(E2)}(\mathbf{r}) = \frac{i k^3}{6\pi \varepsilon \varepsilon_0} \sum_{\sigma=e}^o \sum_{l=1}^{\infty} \sum_{m=0}^l D_{lm} \left[ \mathbf{M}_{\sigma lm}^h(k \mathbf{r}) f_{\sigma lm}^{(E2,t)} + \mathbf{N}_{\sigma lm}^h(k \mathbf{r}) g_{\sigma lm}^{(E2,t)} \right] \quad (6.23)$$

$$f_{\sigma lm}^{(E2,t)} = \nabla' \cdot \mathbf{Q} \cdot \mathbf{M}_{\sigma lm}^j(k \mathbf{r}') + a_l(\omega) \nabla' \cdot \mathbf{Q} \cdot \mathbf{M}_{\sigma lm}^h(k \mathbf{r}') \quad (6.24)$$

$$g_{\sigma lm}^{(E2,t)} = \nabla' \cdot \mathbf{Q} \cdot \mathbf{N}_{\sigma lm}^j(k \mathbf{r}') + b_l(\omega) \nabla' \cdot \mathbf{Q} \cdot \mathbf{N}_{\sigma lm}^h(k \mathbf{r}') \quad (6.25)$$

The molecular multipole moments with  $\mathbf{r}'$  as the origin are ( $\rho$  is the charge density)

$$\mathbf{d} = \int \mathbf{s} \rho(\mathbf{s}) d\mathbf{s} \quad \mathbf{m} = \frac{1}{2} \int \mathbf{s} \times \mathbf{J}(\mathbf{s}) d\mathbf{s} \quad Q_{\alpha\beta} = \int (3s_\alpha s_\beta - s^2 \delta_{\alpha\beta}) \rho(\mathbf{s}) d\mathbf{s} \quad (6.26)$$

where the quadrupole tensor here is traceless and symmetric.

The  $E2$  contribution is the most difficult and depends on the parametrization chosen for the electric quadrupole tensor. We choose the five independent quantities defining this traceless tensor as  $Q_{\pm} = (Q_{xx} \pm Q_{yy})/2$ ,  $Q_{xy}$ ,  $Q_{xz}$ , and  $Q_{yz}$ . Then the operator  $\nabla' \cdot \mathbf{Q}$  in the previous two equations is a row vector  $\nabla' \cdot \mathbf{Q} = \hat{x} [(Q_+ + Q_-) \frac{\partial}{\partial x'} + Q_{xy} \frac{\partial}{\partial y'} + Q_{xz} \frac{\partial}{\partial z'}] + \hat{y} [Q_{xy} \frac{\partial}{\partial x'} + (Q_+ - Q_-) \frac{\partial}{\partial y'} + Q_{yz} \frac{\partial}{\partial z'}] + \hat{z} [Q_{xz} \frac{\partial}{\partial x'} + Q_{yz} \frac{\partial}{\partial y'} - 2Q_+ \frac{\partial}{\partial z'}]$ .

The fields in Eqs. (6.17), (6.20) and (6.23) include radiating molecular multipole



fields plus scattered versions of these fields, depicted respectively, as c) and d) in Fig. 6.3. The pure radiating multipole fields  $\mathbf{E}^{(E1)}(\mathbf{r})$ ,  $\mathbf{E}^{(M1)}(\mathbf{r})$ , and  $\mathbf{E}^{(E2)}(\mathbf{r})$  are special cases of these equations obtained by setting the Mie coefficients  $a_l(\omega)$  and  $b_l(\omega)$  to zero. All corresponding magnetic fields can be obtained using the relations in Eq. (6.16).

The first electric field is precisely as obtained by KWC [109] and includes contributions from general  $m$ , unlike the plane wave expansion. The significance of the above results is that the scattered version of each multipole field can be evaluated in terms of known vector functions (or operations thereon) and Mie-type coefficients  $a_l(\omega)$  and  $b_l(\omega)$  that are *precisely* the same as those arising in the plane wave expansion except evaluated at a different frequency. There are no other unknowns. This result in the  $E1$  case was discussed for spheres by KWC, but is seen to be more general.

The full solution including the higher multipoles in the scattering is put in the form here,

$$\begin{aligned}\mathbf{E}_{\text{rad},t} &= \mathbf{E}_t^{(E1)} + \mathbf{E}_t^{(M1)} + \mathbf{E}_t^{(E2)} \\ &= \mathbf{T}^{(E1)} \cdot \mathbf{d} + \mathbf{T}^{(M1)} \cdot \mathbf{m} + \mathbf{T}^{(E2)} : \mathbf{Q} ,\end{aligned}\tag{6.27}$$

involving the induced molecular moments  $\mathbf{d}$ ,  $\mathbf{m}$ , and  $\mathbf{Q}$  and tensors  $\mathbf{T}^{(E1)}$ ,  $\mathbf{T}^{(M1)}$ , and  $\mathbf{T}^{(E2)}$  whose explicit forms can be extracted directly from Eqs. (6.17)–(6.25).

The induced molecular moments depend on the molecular hyperpolarizability tensors (*vide infra*) and the incident-plus-scattered field quantities  $\mathbf{E}_t$ ,  $\mathbf{B}_t$  and  $\nabla\mathbf{E}_t$  (a 2D tensor formed from outer products of 1D vectors) at the position of the molecule

in the near zone. The three  $\mathbf{T}$  tensors are of size  $3 \times 3$ ,  $3 \times 3$ , and  $3 \times 3 \times 3$ , respectively. Their elements contain the information on the solution of the scattering problems, including complicated sums of products of vector spherical harmonics in the molecular position  $\mathbf{r}'$  and the direction of observation  $\mathbf{r}$ . They also depend on Mie scattering coefficients at the Raman-scattered frequency  $\omega$  (as would be calculated if the incident plane wave were at that frequency). This was detailed in Section 6.3.

#### 6.4.2 Sum Reduction by Analytic Evaluation of $\sigma$ and $m$ Sums

For some scattering geometries, e.g., input field propagation along the  $z$ -axis, polarization vector and molecule along the  $y$ -axis, and observation along the  $x$ -axis, KWC point out that the  $E1$  results of Eqs. (6.17)–(6.19) reduce to simple expressions. For more general geometries, especially for increasing  $kr$  or  $kr'$ , convergence can be excruciatingly slow.

Here a strong simplification in each of the  $\mathbf{T}$  tensors is made. The nested summations involved can become computationally expensive for high accuracy, as remarked even in the SERS case by Kerker, et al. [109] There are three indices,  $l$ ,  $m$  and  $\sigma$ . The nanoparticle multipole index  $l$  (1 for dipole, 2 for quadrupole, etc.) relates to spherical Bessel functions  $j_l(kr)$ , outgoing Hankel functions  $h_l^{(1)}(kr)$ , and their derivatives ( $k$  is the wavevector in the external medium). Both  $l$  and the azimuthal index  $m$  are used for the associated Legendre polynomials  $P_l^m(\cos \theta)$  and their derivatives, while  $\sigma$  (values  $e$  or  $o$ ) are related to the even and odd azimuthal trigonometric functions  $\cos(m\phi)$  and  $\sin(m\phi)$ . We have been able to perform all sums over  $m$  and  $\sigma$  analytically. If  $\gamma$  is the angle between  $\mathbf{r}$  and  $\mathbf{r}'$ ,  $\cos \gamma = \hat{\mathbf{r}} \cdot \hat{\mathbf{r}}' = \cos \theta \cos \theta' + \sin \theta \sin \theta' \cos(\phi - \phi')$ , we

can use the spherical harmonic addition theorem in the form [113],

$$P_l(\cos \gamma) = \sum_{m=0}^l (2 - \delta_{m0}) \frac{(l-m)!}{(l+m)!} P_l^m(\cos \theta) P_l^m(\cos \theta') \cos[m(\phi - \phi')] \quad (6.28)$$

to express all the  $m$  and  $\sigma$  summations in the  $\mathbf{T}$  tensors in terms of low-order derivatives of  $P_l(\cos \gamma)$ .

For the  $E1$  case, one ultimately ends up with a single  $l$ -sum of the form

$$\mathbf{E}_l^{(E1)}(\mathbf{r}) = \frac{i k^3}{\pi \varepsilon \varepsilon_0} \sum_{l=1}^{\infty} \frac{2l+1}{4} [\hat{\mathbf{R}}_{ul}^{(E1)} P_l(\cos \gamma)] \cdot \mathbf{d} , \quad (6.29)$$

where  $\hat{\mathbf{R}}_{ul}^{(E1)}$  is a  $3 \times 3$  tensor *operator* acting on  $P_l(\cos \gamma)$ . In spherical coordinates, the rows of  $\hat{\mathbf{R}}_{ul}^{(E1)}$  are labelled by  $r, \theta, \phi$  and the columns by  $r', \theta', \phi'$ . The tensor is defined component-by-component in Table 6.1 utilizing the following definitions:

$$u_{la}(kr') = j_l(kr') + a_l(\omega) h_l^{(1)}(kr') \quad u_{lb}(kr') = j_l(kr') + b_l(\omega) h_l^{(1)}(kr') \quad (6.30)$$

$$w_{la}(kr') = \eta_l^j(kr') + a_l(\omega) \eta_l^h(kr') \quad w_{lb}(kr') = \eta_l^j(kr') + b_l(\omega) \eta_l^h(kr') \quad (6.31)$$

$$\eta_l^j(x) = \frac{1}{x} \frac{d}{dx} x j_l(x) \quad \eta_l^h(x) = \frac{1}{x} \frac{d}{dx} x h_l^{(1)}(x) . \quad (6.32)$$

Equation 6.29 thus provides an explicit form for  $\mathbf{T}^{(E1)}$

$$\mathbf{T}^{(E1)} = \frac{i k^3}{\pi \varepsilon \varepsilon_0} \sum_{l=1}^{\infty} \frac{2l+1}{4} [\hat{\mathbf{R}}_{ul}^{(E1)} P_l(\cos \gamma)] \quad (6.33)$$

that is efficient for general geometries with  $r > r'$ .

Table 6.1: Components of the  $\hat{\mathbf{R}}_{ul}^{(E1)}$  tensor operator in spherical coordinates for  $r > r'$ .

$l(l+1) \frac{h_l^{(1)}(kr)}{kr} \frac{u_{lb}(kr')}{kr'} \frac{\partial}{\partial \theta}$	$\frac{h_l^{(1)}(kr)}{kr} \frac{u_{lb}(kr')}{kr'} \frac{\partial}{\partial \theta'}$	$\frac{h_l^{(1)}(kr)}{kr} \frac{w_{lb}(kr')}{\sin \theta'} \frac{\partial}{\partial \phi'}$
$\eta_l^h(kr) \frac{u_{lb}(kr')}{kr'} \frac{\partial}{\partial \theta}$	$\frac{h_l^{(1)}(kr) u_{la}(kr')}{l(l+1) \sin \theta \sin \theta'} \frac{\partial}{\partial \phi} \frac{\partial}{\partial \phi'} + \frac{\eta_l^h(kr) w_{lb}(kr')}{l(l+1)} \frac{\partial}{\partial \theta} \frac{\partial}{\partial \theta'}$	$-\frac{h_l^{(1)}(kr) u_{la}(kr')}{l(l+1) \sin \theta} \frac{\partial}{\partial \theta'} \frac{\partial}{\partial \phi} + \frac{\eta_l^h(kr) w_{lb}(kr')}{l(l+1) \sin \theta'} \frac{\partial}{\partial \theta} \frac{\partial}{\partial \phi'}$
$\eta_l^h(kr) \frac{u_{lb}(kr')}{kr'} \frac{1}{\sin \theta} \frac{\partial}{\partial \phi}$	$-\frac{h_l^{(1)}(kr) u_{la}(kr')}{l(l+1) \sin \theta'} \frac{\partial}{\partial \theta} \frac{\partial}{\partial \phi'} + \frac{\eta_l^h(kr) w_{lb}(kr')}{l(l+1) \sin \theta} \frac{\partial}{\partial \theta'} \frac{\partial}{\partial \phi}$	$\frac{h_l^{(1)}(kr) u_{la}(kr')}{l(l+1)} \frac{\partial}{\partial \theta} \frac{\partial}{\partial \theta'} + \frac{\eta_l^h(kr) w_{lb}(kr')}{l(l+1) \sin \theta \sin \theta'} \frac{\partial}{\partial \phi} \frac{\partial}{\partial \phi'}$

For the  $M1$  case, the reduced expression for the electric field is

$$\mathbf{E}_t^{(M1)}(\mathbf{r}) = -\frac{k^3 c \mu \mu_0}{\pi n} \sum_{l=1}^{\infty} \frac{2l+1}{4} [\hat{\mathbf{R}}_{ul}^{(M1)} P_l(\cos \gamma)] \cdot \mathbf{m}. \quad (6.34)$$

The tensor operator components for  $r > r'$  are listed in Table 6.2. Equation (6.34) provides a compact formula for the tensor  $\mathbf{T}^{(M1)}$  analogously to the  $E1$  case shown in Eq. (6.33).

Table 6.2: Components of the  $\hat{\mathbf{R}}_{ul}^{(M1)}$  tensor operator in spherical coordinates for  $r > r'$ .

0	$\frac{h_l^{(1)}(kr)}{kr} \frac{u_{lb}(kr')}{\sin \theta'} \frac{\partial}{\partial \phi'}$	$-\frac{h_l^{(1)}(kr)}{kr} \frac{u_{lb}(kr')}{\sin \theta'} \frac{\partial}{\partial \theta'}$
$h_l^{(1)}(kr) \frac{u_{la}(kr')}{kr'} \frac{1}{\sin \theta} \frac{\partial}{\partial \phi}$	$\frac{h_l^{(1)}(kr) w_{la}(kr')}{l(l+1) \sin \theta} \frac{\partial}{\partial \theta'} \frac{\partial}{\partial \phi} + \frac{\eta_l^h(kr) u_{lb}(kr')}{l(l+1) \sin \theta'} \frac{\partial}{\partial \theta} \frac{\partial}{\partial \phi'}$	$\frac{h_l^{(1)}(kr) w_{la}(kr')}{l(l+1) \sin \theta \sin \theta'} \frac{\partial}{\partial \phi} \frac{\partial}{\partial \phi'} - \frac{\eta_l^h(kr) u_{lb}(kr')}{l(l+1)} \frac{\partial}{\partial \theta} \frac{\partial}{\partial \theta'}$
$-h_l^{(1)}(kr) \frac{u_{la}(kr')}{kr'} \frac{\partial}{\partial \theta}$	$\frac{\eta_l^h(kr) u_{lb}(kr')}{l(l+1) \sin \theta \sin \theta'} \frac{\partial}{\partial \phi} \frac{\partial}{\partial \phi'} - \frac{h_l^{(1)}(kr) w_{la}(kr')}{l(l+1)} \frac{\partial}{\partial \theta} \frac{\partial}{\partial \theta'}$	$-\frac{h_l^{(1)}(kr) w_{la}(kr')}{l(l+1) \sin \theta'} \frac{\partial}{\partial \theta} \frac{\partial}{\partial \phi'} - \frac{\eta_l^h(kr) u_{lb}(kr')}{l(l+1) \sin \theta} \frac{\partial}{\partial \theta'} \frac{\partial}{\partial \phi}$

For the  $E2$  case, there are more components and more complexity. Nevertheless, from Eqs. (6.17)–(6.25), the total  $E2$  field can be expressed as

$$\mathbf{E}_t^{(E2)}(\mathbf{r}) = \frac{i k^3}{6\pi\epsilon\epsilon_0} \sum_{l=1}^{\infty} \frac{2l+1}{4} [\nabla' \cdot \mathbf{Q} \cdot \hat{\mathbf{R}}_{tl}^{(E1)T}]^T P_l(\cos \gamma) \quad (6.35)$$

$$= \frac{i k^3}{6\pi\epsilon\epsilon_0} \sum_{l=1}^{\infty} \frac{2l+1}{4} \hat{\mathbf{R}}_{tl}^{(E1)} P_l(\cos \gamma) \overleftarrow{\nabla}' : \mathbf{Q} \quad (6.36)$$

where the multiple transposes on the first line serve only to correctly contract  $\nabla' \cdot \mathbf{Q}$  with the indices of the primed variables. In the equivalent last line, the gradient with the left arrow acts to the left to avoid use of transposes. (Symmetry of the  $\mathbf{Q}$  matrix is also used here.) This provides a compact form for the  $\mathbf{T}^{(E2)}$  tensor using the  $E1$  tensor and the gradient operator that we use in calculations.

All field calculations here use these reduced-dimension expansions, which simplify computation sufficiently that coding can be executed in Mathematica. The magnetic field components may be obtained directly from the electric field components using Maxwell's curl equations.

## 6.5 Polarizations in SEROA

### 6.5.1 Polarization-Specific Intensity Formulas

Intensity at the detector is evaluated using cycle-averaged components of the Poynting vector in the far zone [92]. The influence of the near-zone scattering then remains in the Mie coefficients multiplying radial scattering functions in  $kr'$ . The transformation to the far zone is achieved by using the asymptotic forms of the radial

functions in  $kr$  [109]. For large observation distance  $r$ , we have that  $\mathbf{E}_{\text{rad},t}$ ,  $\mathbf{B}_{\text{rad},t}$ , and the propagation vector (parallel to  $\hat{r}$ ) are all at right angles and the intensity can be expressed in terms of  $\mathbf{E}_{\text{rad},t}$  alone.  $\mathbf{E}_{\text{rad},t}$  and  $\mathbf{B}_{\text{rad},t}$  are both proportional to  $e^{ikr}/r$ , the Poynting vector is radial and  $|\mathbf{S}| = |\mathbf{E}_{\text{rad},t}|^2 n / 2\mu_0 c$ , where  $n = 1.33$  is the refractive index of water. Using the expressions for the induced molecular multipoles in terms of the total initial fields, the radiated intensity along direction  $\lambda$  (to the first couple orders in the multipole expansion) is proportional to  $|E_{\text{rad},t,\lambda}|^2$ , indexed by  $\lambda$  assuming a value of  $x$ ,  $y$ , or  $z$ .

Substituting for the induced dipole moments in Eq. (6.27) by use of Eqs. (6.7)–(6.9), we get the components of the total radiative field

$$\begin{aligned}
 E_{\text{rad},t,\lambda} \approx & \sum_{\mu,\nu} T_{\lambda,\mu}^{(E1)} \left( \alpha_{\mu,\nu} E_{t,\nu} - i G'_{\mu,\nu} B_{t,\nu} + \frac{1}{3} \sum_{\rho} A_{\mu,\nu,\rho} \frac{\partial}{\partial r'_{\nu}} E_{t,\rho} \right) \\
 & + \sum_{\mu,\nu} T_{\lambda,\mu}^{(M1)} (i G'_{\nu,\mu} E_{t,\nu}) + \sum_{\mu,\nu,\rho} T_{\lambda,\mu,\nu}^{(E2)} (2 A_{\rho,\mu,\nu} E_{t,\rho})
 \end{aligned} \tag{6.37}$$

in terms of the response tensors and the local fields oscillating at the initial frequency  $\omega_0$ . As the molecule rotates, so do the response tensors. Averaging the square of Eq. (6.37) over orientations, dropping very small terms involving only products of

higher-multipole **G** or **A** tensor elements,

$$\begin{aligned}
 |E_{\text{rad},t,\lambda}|^2 &\approx \sum_{\sigma,\tau,\mu,\nu} E_{t,\tau}^* T_{\lambda,\sigma}^{(E1)*} T_{\lambda,\mu}^{(E1)} E_{t,\nu} \langle \alpha_{\sigma,\tau} \alpha_{\mu,\nu} \rangle + 2 \operatorname{Re} \left\{ \sum_{\sigma,\tau,\mu,\nu} E_{t,\tau}^* T_{\lambda,\sigma}^{(E1)*} \right. \\
 &\times \left[ \frac{1}{3} T_{\lambda,\mu}^{(E1)} \sum_{\rho} \frac{\partial}{\partial r'_\nu} E_{t,\rho} \langle \alpha_{\sigma,\tau} A_{\mu,\nu,\rho} \rangle + 2 \sum_{\rho} T_{\lambda,\mu,\nu}^{(E2)} E_{t,\rho} \langle \alpha_{\sigma,\tau} A_{\rho,\mu,\nu} \rangle \right] \Big\} \\
 &+ 2 \operatorname{Im} \left\{ \sum_{\sigma,\tau,\mu,\nu} E_{t,\tau}^* T_{\lambda,\sigma}^{(E1)*} \left[ T_{\lambda,\mu}^{(E1)} B_{t,\nu} \langle \alpha_{\sigma,\tau} G'_{\mu,\nu} \rangle - T_{\lambda,\mu}^{(M1)} E_{t,\nu} \langle \alpha_{\sigma,\tau} G'_{\nu,\mu} \rangle \right] \right\}. \quad (6.38)
 \end{aligned}$$

The far-from-resonance molecular response tensors  $\alpha$ ,  $\mathbf{G}'$  and  $\mathbf{A}$  are of types  $E1/E1$ ,  $E1/M1$ , and  $E1/E2$ , respectively, as described in the book by Barron [111] and discussed earlier. We see that the intensity terms here, as for ROA, group into  $\alpha\alpha$ ,  $\alpha G$ , and  $\alpha A$  terms, depending on the particular products of response tensor components. The angular brackets indicate averaging over rotational variables of the molecule, which proceeds in the same way for both ROA and the present version of SEROA.

The averages may be evaluated, as usual, by expressing response tensors in terms of the molecule-fixed frame quantities and direction cosine matrix elements, followed by integration over the Euler angles [111]. This expresses intensities in terms of the same ROA invariants appearing in regular ROA [111]. The rotational averages in

Eq. (6.38) are all expressible in terms of the frame-invariant quantities [122]

$$\alpha = \frac{1}{3} \sum_{\sigma} \alpha_{\sigma\sigma} , \quad \beta^2(\alpha) = \frac{3}{2} \sum_{\sigma} \sum_{\tau} \alpha_{\sigma\tau} \alpha_{\sigma\tau} - \frac{1}{2} \sum_{\sigma} \alpha_{\sigma\sigma} \sum_{\tau} \alpha_{\tau\tau} \quad (6.39)$$

$$G' = \frac{1}{3} \sum_{\sigma} G'_{\sigma\sigma} , \quad \beta^2(G') = \frac{3}{2} \sum_{\sigma} \sum_{\tau} \alpha_{\sigma\tau} G'_{\sigma\tau} - \frac{1}{2} \sum_{\sigma} \alpha_{\sigma\sigma} \sum_{\tau} G'_{\tau\tau} \quad (6.40)$$

$$\beta^2(A) = \frac{1}{2} \sum_{\sigma} \sum_{\tau} \alpha_{\sigma\tau} A_{\sigma\tau}^{\varepsilon} \quad (6.41)$$

In the latter we employ the double contraction of the tensor  $\mathbf{A}$  with the Levi-Civita antisymmetric tensor ( $\varepsilon_{\sigma\mu\nu}$  elements are +1 for indices in cyclic order, -1 for anticyclic order, 0 otherwise) [92],  $A_{\sigma\tau}^{\varepsilon} = \sum_{\mu} \sum_{\nu} \varepsilon_{\sigma\mu\nu} A_{\mu\nu\tau}$ . These ROA invariants [123, 124, 122, 124] in Eq. (6.41) are an extension of the far-from-resonance Placzek invariants used in ordinary Raman scattering [125]. All of the molecule-specific information is contained in these scalar quantities, which may be calculated in the molecular frame if electronic structure programs are used. The quantities that these rotational averages multiply in Eq. (6.38) are considerably different than in ROA, but it is still possible to express all the intensities for each polarization scheme in terms of these reduced constants.

There are two principal differences between Eq. (6.38) and its ROA limit (no nanoparticle). The first is the use of the total local fields and gradients,  $\mathbf{E}_t$ ,  $\mathbf{B}_t$ , and  $\nabla' \mathbf{E}_t$ , that depend on the incident frequency  $\omega_0$  and are evaluated at the molecular position  $\mathbf{r}'$ . These have contributions from the scattering of the plane wave by the nanoparticle that do not all point in the same directions as their plane wave components. The second is the make-up of the  $\mathbf{T}$  tensors, which depend both on the



plasmonic nanoparticle and on details of the molecular scattering via multipole fields at frequency  $\omega$ . There are other slight differences since, even far-from-resonance, there are two distinct types of  $\alpha G$  terms and two distinct types of  $\alpha A$  terms in Eq. (6.38), corresponding to whether the upward or downward transition is  $E1$ . These terms combine more gracefully in the far-from-resonance ROA formalism [92]. This limit can be verified by eliminating the nanoparticle, i.e., making all Mie scattering coefficients zero, but we have so far not obtained a simplification of the  $\alpha G$  and  $\alpha A$  cross-terms in Eq. (6.38) when the nanoparticle is present.

Equation (6.38) can be modified for each of the different polarization schemes. Let us take right/left circular polarization vectors as  $(\hat{x} \mp i\hat{y})/\sqrt{2}$  for propagation along the positive  $z$  axis as usual. For ICP, Eq. (6.38) applies straightforwardly by using  $\mathbf{E} = E_0(\hat{x} \mp i\hat{y})/\sqrt{2}$  on incidence, calculating the scattering wave from the nanoparticle, then constructing the total local fields and gradients at the molecule position  $\mathbf{r}'$ . For SCP SEROA, one uses linear incident polarization for these fields in Equation (6.38), but combines the  $\lambda = x$  and  $y$  cases with complex coefficients. (For light propagating in the backscatter geometry, the  $R$  and  $L$  polarizations as measured by a common observer will switch from their definitions in the incident beam.) For DCP SEROA, these considerations must be combined.

### 6.5.2 Selectivity in ICP and SCP

Differential intensities will be dominated by  $\alpha\alpha$  contributions unless they are exactly zero. In ROA this is guaranteed by averaging over molecular rotations. In SEROA this must be carefully examined. If  $\alpha\alpha$  differences fail to vanish, they may

arise from either chiral or achiral molecules and SEROA measurements are not strictly interpretable in terms of chirality in the molecular analyte.

Insight can be gained by focusing on a single nanoparticle plasmon multipole and on just the  $\alpha\alpha$  intensity contributions important to total Raman scattering. Let us consider the frequency range for which the  $l = 1$  (dipole plasmon) mode is the chief contributor to  $\mathbf{T}^{(E1)}$  in Eq. (6.33). The radiative fields may be calculated according to Table 6.1 in terms of the molecular position  $r'$ ,  $\theta'$ ,  $\phi'$  for backscatter observation along  $r \rightarrow \infty$ ,  $\theta = \pi$ , and  $\phi = 0$ . The molecular position also enters the  $\alpha\alpha$  intensity terms on the right-hand side of Eq. (6.38) through the total local field. If the incident plane wave is taken to propagate along positive  $z$  and to have its polarization vector in the  $x - y$  plane with values  $E_{0x}$  and  $E_{0y}$ , the  $l = 1$  local field at the molecular position can be worked out to be (in spherical components)

$$\mathbf{E}_t = \frac{3}{2} \left[ \frac{u_{1b0}}{k_0 r'} \sin \theta' E'_{0x}, (i u_{1a0} + w_{1b0} \cos \theta') E'_{0x}, (w_{1b0} + i u_{1a0} \cos \theta') E'_{0y} \right]^T. \quad (6.42)$$

The  $u$  and  $w$  functions of  $r'$  are as defined in Eqs. (6.30) and (6.31), except that the subscript zero implies  $k \rightarrow k_0$  and  $\omega \rightarrow \omega_0$ . The field quantities with primes are rotated versions of the incident field vectors  $E'_{0x} = E_{0x} \cos \phi' + i E_{0y} \sin \phi'$  and  $E'_{0y} = -E_{0x} \sin \phi' + i E_{0y} \cos \phi'$ .

If we take  $\theta' = \pi/2$ , for example, with  $E_{0x}$  and  $E_{0y}$  both real, it is found that the

rotationally-averaged  $\alpha\alpha$  contributions to the differential intensity are

$$\begin{aligned}
 (I_R - I_L)_{\alpha\alpha} = & \left( \frac{3k^2}{4\pi\epsilon\epsilon_0} \right)^2 \frac{3}{160} [(E_{0x}^2 - E_{0y}^2) \sin 2\phi' - 2E_{0x}E_{0y} \cos 2\phi'] \\
 & \times \left\{ -2\beta^2(\alpha) \left[ \frac{4}{k_0 r' k r'} \text{Im}(u_{1b0}^* w_{1b0} u_{1b} w_{1b}^*) + \text{Im}(u_{1a0}^* w_{1b0} u_{1a} w_{1b}^*) \right] \right. \\
 & \left. + \frac{4}{3} [9\alpha^2 - \beta^2(\alpha)] \left[ \frac{4}{k_0 r' k r'} \text{Im}(u_{1b0}^* w_{1b0} u_{1b}^* w_{1b}) + \text{Im}(u_{1a0}^* w_{1b0} u_{1a}^* w_{1b}) \right] \right\}
 \end{aligned} \tag{6.43}$$

This has factored into  $r'$  and  $\phi'$  parts. Previously, we have investigated the cases  $E_{0x} = 0$  and  $E_{0y} = 0$ , for which Eq. (6.43) has an overall factor of  $\sin 2\phi'$ . These results also hold for other values of  $l$  and of  $\theta'$ . This simple angular dependence is therefore the behavior in  $\phi'$  noted empirically before [84]. The new consideration is that cross-terms proportional to  $\cos 2\phi'$  will occur if both  $E_{0x} \neq 0$  and  $E_{0y} \neq 0$ . Then these  $\alpha\alpha$  differential contributions will not vanish at  $\phi' = \pi/2$ , though they will still vanish on averaging over  $\phi'$ .

### 6.5.3 Selectivity in DCP

DCP is one situation in which both  $E_{0x} \neq 0$  and  $E_{0y} \neq 0$ , but it is a special case since the amplitudes are of the same magnitude and precisely  $90^\circ$  out of phase. The analytical behavior of the  $\alpha\alpha$  terms was therefore examined again in this case. For  $l = 1$  and  $\theta' = \pi/2$  once more, using  $R$  incident polarization, it was found that the leading intensity terms for  $R$  (upper sign) and  $L$  (lower sign) scattered polarizations

are

$$\begin{aligned}
 (I_{R/L}^R)_{\alpha\alpha} = \frac{|E_0|^2 27k^4}{5120\pi^2 \varepsilon^2 \varepsilon_0^2} & \left\{ \left[ 6\alpha^2 - \frac{2}{3}\beta^2(\alpha) \right] \left| u_{1a}u_{1a0} \mp w_{1b}w_{1b0} - 4\frac{u_{1b}}{kr'} \frac{u_{1b0}}{k_0r'} \right|^2 \right. \\
 & + \beta^2(\alpha) \left( 32 \left| \frac{u_{1b}}{kr'} \right|^2 \left| \frac{u_{1b0}}{k_0r'} \right|^2 + 2|u_{1a}u_{1a0}|^2 + 2|w_{1b}w_{1b0}|^2 \right. \\
 & \left. \left. + 4 \left| u_{1a} \frac{u_{1b0}}{k_0r'} + \frac{u_{1b}}{kr'} u_{1a0} \right|^2 + 4 \left| w_{1b} \frac{u_{1b0}}{k_0r'} \mp \frac{u_{1b}}{kr'} w_{1b0} \right|^2 + |u_{1a}w_{1b0} \mp u_{1a0}w_{1b}|^2 \right) \right\} \quad (6.44)
 \end{aligned}$$

This is *completely independent of  $\phi'$* . Furthermore, when  $L$  incident light is used, one finds the same results, i.e.,

$$(I_R^R)_{\alpha\alpha} = (I_L^L)_{\alpha\alpha} , \quad (I_L^R)_{\alpha\alpha} = (I_R^L)_{\alpha\alpha} . \quad (6.45)$$

This is important information. The DCP<sub>I</sub> in-phase difference then reduces to

$$I_R^R - I_L^L = (I_R^R - I_L^L)_{\alpha G} + (I_R^R - I_L^L)_{\alpha A} \quad (6.46)$$

while the DCP<sub>II</sub> strategy out-of-phase differences reduces to

$$I_L^R - I_R^L = (I_L^R - I_R^L)_{\alpha G} + (I_L^R - I_R^L)_{\alpha A} , \quad (6.47)$$

both of which are free of any contamination from  $\alpha\alpha$  terms.

This leads directly to the question of other values of  $\theta'$ . It is straightforward to continue the analytical analysis using symbolic algebra, though the increased number of terms for general  $\theta'$  is much too large to present here. The result is that the

quantities  $(I_R^R)_{\alpha\alpha}$ ,  $(I_L^R)_{\alpha\alpha}$ ,  $(I_R^L)_{\alpha\alpha}$ , and  $(I_L^L)_{\alpha\alpha}$  all remain independent of azimuth, and Eqs. (6.45) are verified to hold for all polar and azimuthal molecular directions. They were furthermore verified analytically for  $l = 2$ , the quadrupole plasmon mode. Thus, *any  $\alpha\alpha$  contributions to differential intensities, which can be due to either chiral or achiral molecules, appear to be completely avoided in backscatter DCP SEROA.*

One can similarly calculate  $\alpha G$  and  $\alpha A$  contributions through symbolic algebra, though the intermediate calculations are also too lengthy to include. In the final analysis, we find that backscatter DCP gives the specific results

$$(I_L^L)_{\alpha G} = -(I_R^R)_{\alpha G} , \quad (I_R^L)_{\alpha G} = -(I_L^R)_{\alpha G} , \quad (6.48)$$

$$(I_L^L)_{\alpha A} = -(I_R^R)_{\alpha A} , \quad (I_R^L)_{\alpha A} = -(I_L^R)_{\alpha A} , \quad (6.49)$$

so that normalized CIDs for DCP<sub>I</sub> and DCP<sub>II</sub> simplify to

$$\Delta_I = \frac{I_R^R - I_L^L}{I_R^R + I_L^L} = \frac{(I_R^R)_{\alpha G} + (I_R^R)_{\alpha A}}{(I_R^R)_{\alpha\alpha}} = -\frac{(I_L^L)_{\alpha G} + (I_L^L)_{\alpha A}}{(I_L^L)_{\alpha\alpha}} \quad (6.50)$$

$$\Delta_{II} = \frac{I_L^R - I_R^L}{I_L^R + I_R^L} = \frac{(I_L^R)_{\alpha G} + (I_L^R)_{\alpha A}}{(I_L^R)_{\alpha\alpha}} = -\frac{(I_R^L)_{\alpha G} + (I_R^L)_{\alpha A}}{(I_R^L)_{\alpha\alpha}} \quad (6.51)$$

These relations hold for both ROA and our SEROA model.

While DCP scattering has some advantages in ordinary ROA [126, 127, 128], they appear to be considerably more dramatic here. In particular, it is not necessary to invoke additional ensemble averaging to eliminate possible interference from achiral molecules. One can consider the DCP investigation of small analyte concentrations without concern that scattering intensity differences are contaminated by

achiral molecules for some directions around the spherical nanoparticle.

In an indirectly-related vein, the experiments by Kneipp, et al., [98] already used a backscatter DCP<sub>1</sub> SEROA arrangement for adenine adsorbed on isolated silver colloidal particles. While adenine is not chiral by itself, the authors suggest that the differential scattering observed arises from formation of a chiral complex with the surface. The significance of the circular intensity differences has been the subject of some debate [101, 93] that will probably take some time to resolve. Certainly the current results do not apply directly to the experiment by Kneipp, et al., since adsorption is not considered here. They do, however, argue that it would be interesting to have more experimental investigations of DCP SEROA.

## 6.6 Application to a Chiral Molecule Model

We wish to obtain SEROA enhancement profiles throughout the visible/NIR spectrum incorporating both absorption and emission enhancements, similar to the SERS enhancement profiles calculated by KWC (their Fig. 2). Besides including higher multipoles, however, we also want to include wavelength dependence of the molecular response tensors and we want the latter to be the “derived” response tensors appropriate for Raman transitions. For example, according to Placzek theory [92, 125, 129], the correct polarizability tensor to use for vibrational scattering between initial  $v^i$  and final  $v^f$  vibrational levels is  $\langle v^f | \boldsymbol{\alpha} | v^i \rangle$ , where  $\boldsymbol{\alpha}$  may be Taylor-expanded about

the equilibrium molecular geometry to give

$$\langle v^f | \alpha_{kl} | v^i \rangle = (\alpha_{kl})_e \delta_{v^f v^i} + \sum_j (\partial \alpha_{kl} / \partial Q_j)_e \langle v^f | Q_j | v^i \rangle + \dots \quad (6.52)$$

The first term corresponds to Rayleigh scattering while the next terms correspond in the harmonic approximation to the various Raman fundamental modes. Similarly the  $\mathbf{G}'$  and  $\mathbf{A}$  tensors can be Taylor-expanded [92] and their first derivatives calculated with respect to the normal coordinate  $Q_j$  of interest. For a fundamental transition in mode  $j$  in the harmonic approximation, the quantum sum-over-states formulae for the derived response tensors are [111]

$$\frac{\partial \alpha_{kl}}{\partial Q_j} = \frac{2}{\hbar} \frac{\partial}{\partial Q_j} \sum_{n \neq 1} \frac{\omega_{n1}}{\omega_{n1}^2 - \omega^2} \text{Re} [\langle 1 | \hat{d}_k | n \rangle \langle n | \hat{d}_l | 1 \rangle] \quad (6.53)$$

$$\frac{\partial G'_{kl}}{\partial Q_j} = -\frac{2}{\hbar} \frac{\partial}{\partial Q_j} \sum_{n \neq 1} \frac{\omega}{\omega_{n1}^2 - \omega^2} \text{Im} [\langle 1 | \hat{d}_k | n \rangle \langle n | \hat{m}_l | 1 \rangle] \quad (6.54)$$

$$\frac{\partial A_{ikl}}{\partial Q_j} = \frac{1}{\hbar} \frac{\partial}{\partial Q_j} \sum_{n \neq 1} \frac{\omega_{n1}}{\omega_{n1}^2 - \omega^2} \text{Re} [\langle 1 | \hat{d}_i | n \rangle \langle n | \hat{Q}_{kl} | 1 \rangle] \quad (6.55)$$

Within the Born-Oppenheimer separation, both energies and transition matrix elements depend on the normal coordinates.

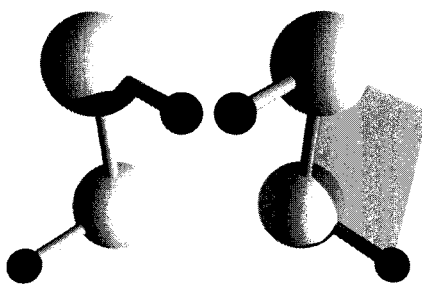


Figure 6.5: Enantiomers of  $\text{H}_2\text{S}_2$ .

While there is progress being made in the ab initio calculation of such quantities [114, 130, 131, 132], it is more useful for our current purposes to adopt the qualitative twisted-arc model, which has been applied by Trost and Hornberger [110] to hydrogen persulfide,  $\text{H}_2\text{S}_2$  (Fig. 6.5) a small molecule forming enantiomeric pairs. The simple 1D twisted-arc model considers a delocalized electron to move within a “box” formed from two planar arcs joined at the center of  $\text{H}_2\text{S}_2$  and twisted with respect to each other by the dihedral angle  $\chi$ . Trost and Hornberger derive quantum mechanical wave functions and matrix elements exhibiting simple  $\chi$  dependences, allowing sum-over-states evaluation of ROA tensors that can easily be differentiated with respect to  $\chi$ . Thus we can obtain derived ROA tensors depending both on the excitation frequency (dynamical tensors) and on the particular vibrational coordinate that controls the chirality of the molecule. Ignoring coupling to other coordinates,  $\chi$  is approximately the torsional normal coordinate  $Q_4$  of  $\text{H}_2\text{S}_2$ , which has wavenumber [133]  $\tilde{\nu}_4 \sim 420 \text{ cm}^{-1}$  and a diagonal harmonic force constant [134]  $f_{44} \sim 0.092 \text{ aJ/rad}^2$ .

One can readily differentiate the parametric  $\chi$  dependence of the tensors from the twisted-arc model to obtain  $d\boldsymbol{\alpha}/d\chi$ ,  $d\mathbf{G}'/d\chi$ , and  $d\mathbf{A}/d\chi$  appropriate to Raman excitation. This is done in the calculations, though we continue to use the  $\boldsymbol{\alpha}$ ,  $\mathbf{G}'$ , and  $\mathbf{A}$  notation for simplicity in the text. Issues of reactivity are ignored as this is a spectroscopic model that will be augmented only by plasmonic enhancement effects. The first excited electronic state is in the UV region of the spectrum, so the Raman scattering we calculate is effectively far-from-resonance.

As before, we consider 40/50 Ag and Au nanoshells with silica cores (40 nm inner radius, 50 nm outer radius). The dielectric functions for Ag and Au, widely



used in SERS, are obtained by frequency-interpolating the tabulation of Johnson and Christy [135]. The dielectric constant for the silica core is taken as 2.04 and that for an aqueous surrounding medium as  $n^2$ , where the index of refraction  $n = 1.33$ .

The signal intensity obtained at the remote detector location  $(r, \theta, \phi)$ ,  $kr \gg 1$ , is proportional to  $|\mathbf{F}(\theta, \phi)|^2$  [109], where

$$\mathbf{F}(\theta, \phi) = \left[ r e^{-ikr} \mathbf{E}_{\text{rad},t}(r, \theta, \phi) \right]_{kr \rightarrow \infty} . \quad (6.56)$$

The latter is a superposition of contributions from the different multipole fields and is evaluated using known asymptotic forms for the spherical Bessel functions. One may calculate enhancements of radiated intensity in specific directions as done by KWC for  $E1$ -only emission, calculating  $\mathbf{F}(\theta, \phi)$  in both the presence and absence of the nanoparticle. This ratio can of course be singular in directions for which the unenhanced  $\mathbf{F}(\theta, \phi)$  vanishes, so we seek non-singular characteristic measures of the enhancements each type of radiation field can produce.

We can label  $\mathbf{F}$  in each polarization channel by the same subscripts and superscripts used above, e.g.,  $\mathbf{F}_R^R$ . From Eqs. (6.50) and (6.51), one can express the CIDs directly in terms of these quantities. For the Ag nanoshell, 600 nm excitation, and the particular molecular position  $r' = 51$  nm,  $\theta' = \phi' = \pi/2$ , each of the different cases of  $|\mathbf{F}|^2$  is decomposed into  $\alpha\alpha$ ,  $\alpha G$  and  $\alpha A$  contributions in Table 6.3. Each component is calculated to convergence using  $l_{\text{max}} = 12$  for calculation of incident wave scattering and  $l_{\text{max}} = 20$  for calculation of molecular multipole field scattering. The result is independent of the choice of  $\phi'$ . Equations (6.45), (6.48) and (6.49) are

Table 6.3: Intensity factors for 600 nm DCP backscattering with model H<sub>2</sub>S<sub>2</sub> 1 nm outside 40/50 Ag nanoshell with  $\theta' = \phi' = \pi/2$ . Results are independent of  $\phi'$ . Each column sum is overall positive, though individual components need not be. Units are  $V^2$ .

	$ \mathbf{F}_R^R ^2$	$ \mathbf{F}_L^R ^2$	$ \mathbf{F}_R^L ^2$	$ \mathbf{F}_L^L ^2$
$\alpha\alpha$	4.72261994e-30	8.12869194e-30	8.12869194e-30	4.72261994e-30
$\alpha G$	-3.44471119e-36	-2.24170169e-36	2.24170169e-36	3.44471119e-36
$\alpha A$	-8.15333967e-36	2.37864046e-35	-2.37864046e-35	8.15333967e-36

fully verified here, as can be seen from identical  $\alpha\alpha$  values (so differences vanish) and identical-but-opposite  $\alpha G$  and  $\alpha A$  values across the columns.

If one replaces the Mie coefficients in Table 6.3 with zero, the ordinary ROA results will follow this same pattern except that the out-of-phase intensity factors  $|\mathbf{F}_L^R|_{\alpha G}^2 = |\mathbf{F}_R^L|_{\alpha G}^2 = |\mathbf{F}_L^R|_{\alpha A}^2 = |\mathbf{F}_R^L|_{\alpha A}^2 = 0$ . In this limit, the far-from-resonance backscatter DCP<sub>II</sub> arrangement ROA signal vanishes, and ICP/SCP/DCP<sub>I</sub> ROA gain equivalence [136, 137]. The DCP<sub>II</sub> intensities actually only vanish exactly in this limit for Rayleigh scattering, though they are small for Raman scattering to the extent that  $(\omega - \omega_0)/\omega$  is small. With inclusion of the plasmonic effects of the nanoshell, DCP<sub>II</sub> becomes somewhat stronger and so we include comparison of both forms of DCP here.

Figure 6.6 shows components  $|\mathbf{F}_R^R|_{\alpha\alpha}^2$  and  $|\mathbf{F}_L^R|_{\alpha\alpha}^2$  for the Ag nanoshell as computed with the molecule positioned at three polar angles  $\theta' = 0, \pi/2$ , and  $\pi$ . The total DCP<sub>I</sub> and DCP<sub>II</sub> scattering intensities are proportional to these two factors, respectively, as can be seen from Eqs. (6.45), (6.48), and (6.49). One can observe the nanoshell dipole mode at longer wavelengths and the quadrupole and octupole modes at shorter wavelengths. It is immediately clear that the dipole surface plasmon mode dominates for the molecule near the equator, while quadrupole modes dominate for molecules

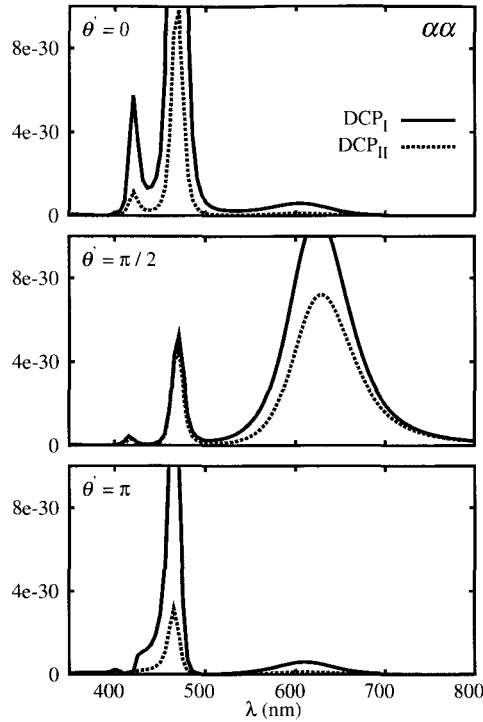


Figure 6.6: Calculation of the 40/50 Ag nanoshell DCP  $\alpha\alpha$  total scattering intensity factors  $|\mathbf{F}_R^R|^2$  and  $|\mathbf{F}_L^R|^2$  as functions of excitation wavelength at three different polar angles of the molecule and 1 nm outside the shell radius. The nanoshell-dipole features are most pronounced for equatorial molecules, while nanoshell-quadrupole features are most pronounced in the polar regions. Units are  $V^2$ .

near the poles. The modes are well-separated energetically, and therefore the relative importance of different polar angles can change markedly with excitation energy. It is further observed that the DCP<sub>I</sub> Raman scattering is generally larger than the DCP<sub>II</sub> Raman scattering. This is consistent with the  $b$  vibrational symmetry of the torsional mode of  $\text{H}_2\text{S}_2$  in  $\text{C}_2$  geometry and the depolarized character of Raman measurements for DCP<sub>I</sub> in backscatter geometries.

Figure 6.7 shows the corresponding  $\alpha G$  and  $\alpha A$  contributions. Each of the frames has the same ranges to simplify comparisons. While not fully shown, the quadrupole contributions are once again strongly enhanced near the north and south poles. In contrast, the contributions in the nanoshell-dipole region are of similar magnitudes

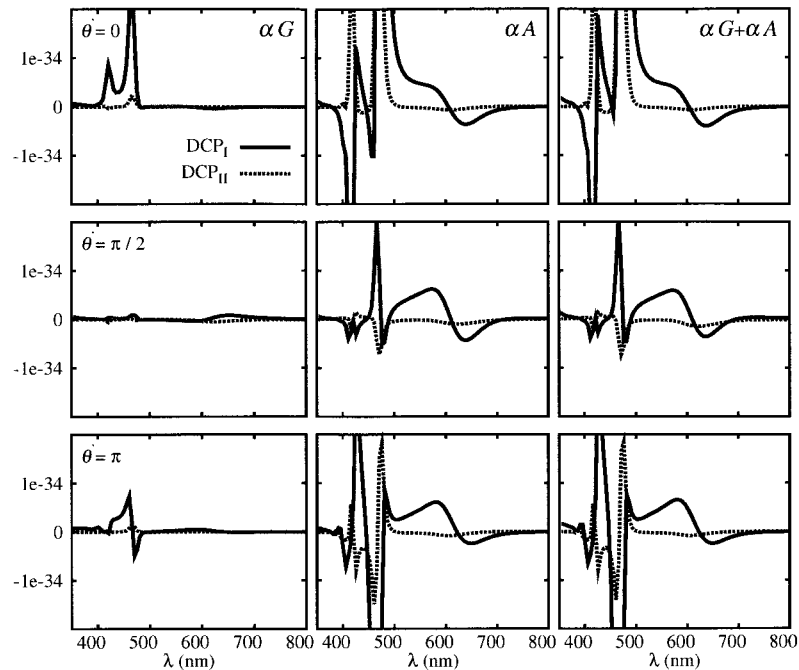


Figure 6.7: DCP  $\alpha G$  components  $|\mathbf{F}_R^R|^2$  and  $|\mathbf{F}_L^L|^2$  (column 1),  $\alpha A$  components  $|\mathbf{F}_R^R|^2$  and  $|\mathbf{F}_L^L|^2$  (column 2) and their sums (column 3) corresponding to the Ag nanoshell data of Fig. 6.6 at three different polar angles of the  $\text{H}_2\text{S}_2$  molecule. The magnitudes in the dipole plasmon spectral regions are relatively insensitive to polar angle, as opposed to Fig. 6.6. Units are  $V^2$ .

for the different values of  $\theta'$ . Similar to the situation shown for SCP before, each of the  $\alpha\alpha$ ,  $\alpha G$ , and  $\alpha A$  terms have their own excitation/enhancement curves. This is certainly true for the rapid variations seen in the  $l = 2$  and higher spectral regions to the short wavelength side, but is also evident in the  $l = 1$  nanoshell dipole region. In fact, it is even clear that, while  $\text{DCP}_I$  still exhibits stronger intensities as a general rule, the shapes of the  $\text{DCP}_I$  and  $\text{DCP}_{II}$  excitation curves show significant differences. In particular,  $\text{DCP}_I$  shows a strong tendency to change sign. That is, a particular vibrational feature in off-resonant SEROA may apparently exhibit an abrupt sign change as a function of excitation, unlike the situation for ordinary off-resonant ROA. A further conclusion that mirrors the findings from the SCP investigation is that the

$\alpha A$  terms strongly dominate the  $\alpha G$  terms. This is in opposition to ordinary ROA, where the latter tend to dominate [114] and is a reflection (in part) of the strong variations in local fields near the plasmonic nanoparticle. Here we are able to make this point quantitatively.

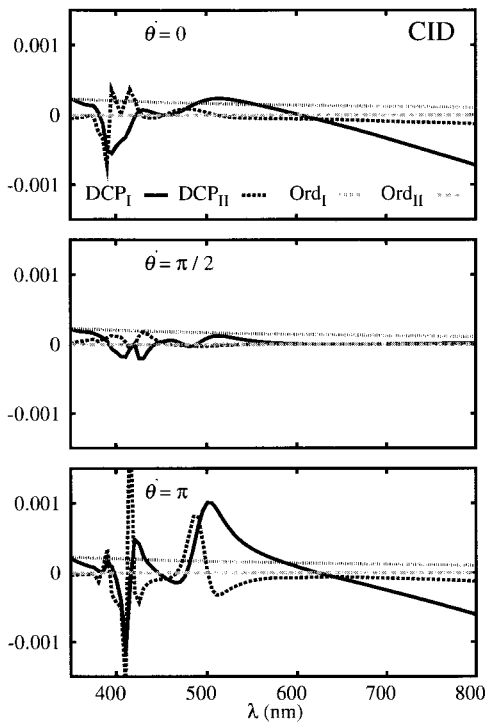


Figure 6.8: DCP CIDs  $\Delta_I$  and  $\Delta_{II}$  of Eqs. (6.50) and (6.51) corresponding to the Ag nanoshell intensity components in Figures 6.6 and 6.7. The CIDs for ordinary DCP<sub>I</sub> and DCP<sub>II</sub> ROA are shown for comparison in each frame, though they are independent of  $\theta'$ .

Figure 6.8 shows the normalized CIDs corresponding to Eqs. (6.50) and (6.51). Larger CIDs are preferable experimentally. It is seen for  $\theta' = \pi/2$  that the CIDs are strongly suppressed in the nanoshell dipole portion of the excitation profile. Based on scaling laws, Janesko and Scuseria [100] give an extended discussion of the fact that SEROA with a dipolar substrate can decrease the normalized CIDs relative to ROA and that quadrupolar substates may very well be preferable. The spherical

substrates used here have both types of modes, which may be selected by excitation frequency. The dipole plasmon spectral region does indeed give a small CID for equatorial molecules, as seen in the middle frame of Figure 6.8. The reason is that the  $\alpha G + \alpha A$  numerators shown in the last column of Figure 6.7 are of similar magnitudes for different  $\theta'$ , while the  $\alpha\alpha$  denominator terms displayed in Figure 6.6 are strongly peaked equatorially. The other observation is that the DCP<sub>I</sub> CIDs for molecules at the north and south poles grow in magnitude significantly as we leave this region and head to longer wavelengths where the dipole enhancement tails off. The combined conclusion is that the dipole plasmon peak resonance is definitely *not* the preferred excitation energy to use.

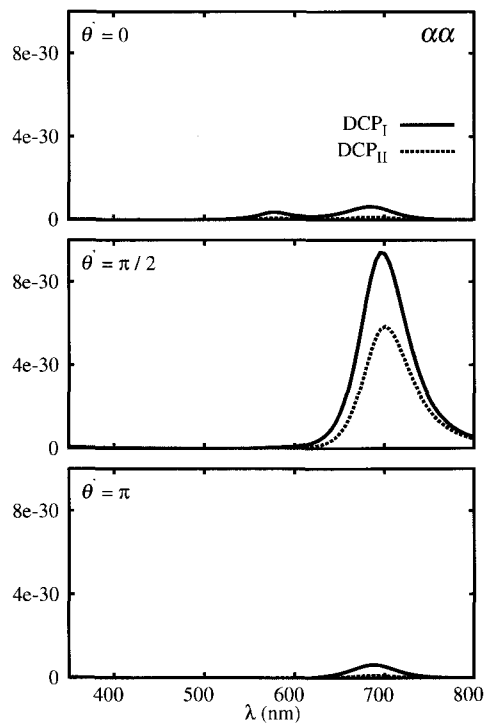


Figure 6.9: Calculation of the 40/50 Au nanoshell DCP  $\alpha\alpha$  total scattering intensity factors  $|\mathbf{F}_R^R|_{\alpha\alpha}^2$  and  $|\mathbf{F}_L^R|_{\alpha\alpha}^2$ , analogous to the Ag nanoshell calculations of Fig. 6.6.

The  $\alpha\alpha$  contributions for the Au nanoshell are shown in Figure 6.9. The nanoshell

quadrupole contributions are smaller and closer to the nanoshell dipole region, as can be seen (with effort) for  $\theta' = 0$ . Those for  $\theta' = \pi$  are not visible, whereas they were merely smaller for Ag in Figure 6.6. Once again the dipole contributions are significantly larger equatorially and DCP<sub>I</sub> signals are generally more intense than DCP<sub>II</sub> signals.

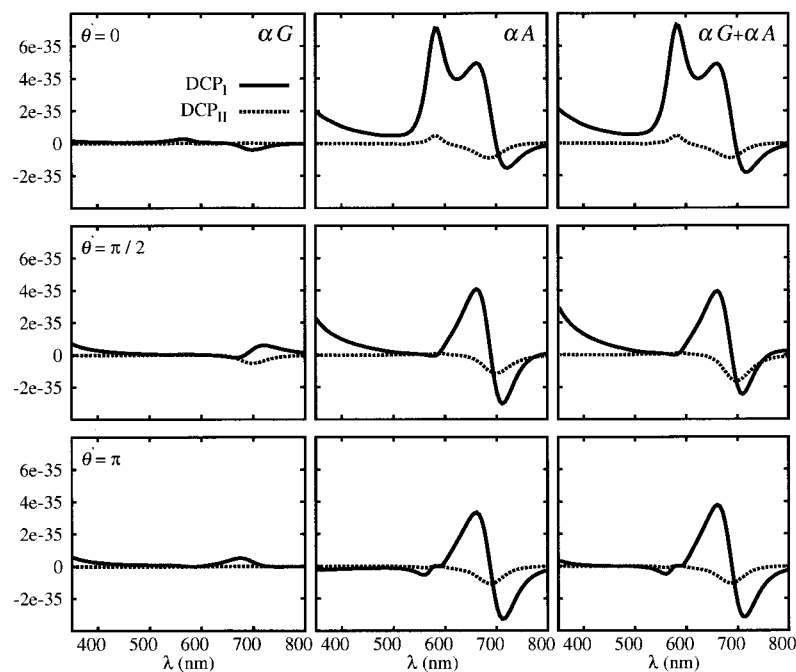


Figure 6.10: DCP  $\alpha G$ ,  $\alpha A$ , and  $\alpha G + \alpha A$  components for the Au nanoshell, analogous to the Ag nanoshell calculations of Fig. 6.7.

Figure 6.10 shows that the  $\alpha G$  terms are once again significantly smaller than  $\alpha A$  terms. The latter are of similar magnitude for most values of  $\theta'$ , except for the larger DCP<sub>I</sub> response in the quadrupole plasmon region  $\lambda < 600$  nm for  $\theta' \sim 0$ . Comparing Figs. 6.7 and 6.10, a common pattern emerges. Near the peak of the nanoshell-dipole scattering curve, the  $\alpha G + \alpha A$  cross-terms for DCP<sub>II</sub> are relatively small but roughly follow the shape of the  $\alpha\alpha$  curve (to within a sign). The DCP<sub>I</sub> cross-terms are generally much larger but go through a zero-crossing near the peak

of the  $\alpha\alpha$  dipole plasmon excitation curve.

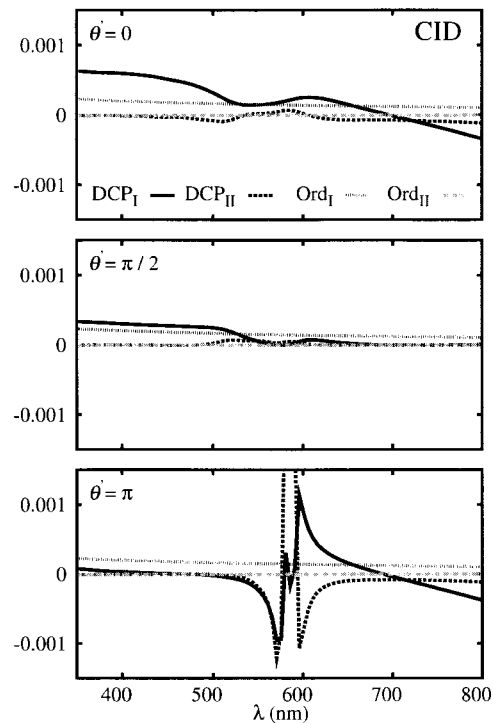


Figure 6.11: DCP CIDs  $\Delta_I$  and  $\Delta_{II}$  for the Au nanoshell intensity components in Figs. 6.9 and 6.10, analogous to the Ag nanoshell calculations of Fig. 6.8.

The normalized CIDs in the nanoshell-dipole region of Figure 6.11 also follow the same pattern as for Ag in Figure 6.8. They are noticeably suppressed for equatorial molecules where the  $\alpha\alpha$  peak is strong. For molecules at either the north or south pole, the  $\text{DCP}_{II}$  CID is relatively flat for the dipole plasmon region, while the  $\text{DCP}_I$  CID crosses through zero and continues to rise in magnitude for an extended region to longer wavelengths.

The experimental importance of the normalized CIDs is that they largely remove effects due to, for example, variations in detector efficiency and laser intensity. Furthermore, signal-to-noise ratios achieved in SEROA differential scattering will play a part in determining the smallest magnitudes of CIDs worth pursuing. Nevertheless,



surface plasmon enhancement has been shown here to complicate the interpretation of the CIDs compared to the benign situation for ROA. Each of the  $\alpha\alpha$ ,  $\alpha G$ , and  $\alpha A$  contributions to the Raman scattering exhibit their own enhancement curves. The CIDs therefore depend on the details of the enhancement curves in both the numerator and the denominator, and optimal dipole-peak enhancement in fact leads to sub-optimal CIDs. This is not the issue in the quadrupole plasmon excitation region, but there large swings of different terms and the resultant CIDs are exhibited. The undesirable consequence is that small changes in excitation frequency can easily lead to sign reversals for some vibrational features in SEROA (a problem also found for different binding geometries with adsorption by Janesko and Scuseria [138]).

On balance, the most promising recommendation for experimental investigations appears to be use of the DCP<sub>I</sub> configuration somewhat to the longer-wavelength side of the nanoshell-dipole peak. There is presumably a balance to be achieved between decreasing overall signals and increasing CIDs in these regions. While there are no ROA or SEROA instruments reported capable of tuneable excitation, it is possible to instead prepare a series of nanoshells with systematically-shifted surface plasmon resonance peaks [139].

## 6.7 Summary

A SEROA formalism for calculation of ROA enhancement in the case of (off-resonant) chiral molecules moving near spherical metal nanoshells has been constructed and investigated in detail. In these circumstances only electromagnetic

enhancement (enhanced plasmonic density of states) needs to be considered. Mie theory and EM Green Tensor techniques have been extended to include molecular magnetic dipole and electric quadrupole fields, marrying the SERS scattering model of Kerker, et al. [109], with the ROA treatment by Barron and Buckingham [92]. The molecule is assumed to be far from resonance with both the incident light and the surface plasmon absorption profile. Vector spherical harmonic expansions of incident and molecular multipole fields, as well as their enhancing counterparts scattered from the plasmonic nanoparticle, have been simplified by dimensional reduction of the summations involved.

Our SEROA formalism was applied to a simple chiral-molecule model (of  $\text{H}_2\text{S}_2$ ) providing “derived” molecular response tensors including excitation wavelength dependence. This was used as a tool to investigate whether SEROA CID measurements in even a special case could be interpreted strictly in terms of  $E1/M1$  and  $E1/E2$  cross-terms in the Raman scattering intensities as is the case for ROA.

A first backscatter SCP SEROA analysis with isolated silica-core Ag and Au nanoshells exhibited  $E1/E1$  ( $\alpha\alpha$ ) contributions to the differential intensities that depended on azimuthal position of the molecule around the nanoparticle. This was verified through analytical methods. It was determined for backscatter configurations that a combination of averaging over molecular rotations *and* molecular positions around the nanoshells ensures that  $\alpha\alpha$  contributions to SEROA vanish. Remaining nonzero contributions are strictly  $\alpha G$  and  $\alpha A$ , but even they vanish if the molecule is achiral (from rotational averaging alone). That is, a specific SEROA scenario has been theoretically confirmed to retain the chiral selectivity exhibited by normal

ROA. Corresponding SEROA excitation profiles were calculated and analyzed, showing quantifiably greater prominence of  $\alpha A$  contributions than in ROA.

Other experimental polarization SEROA schemes were investigated within our formalism. Symbolic algebra was used to determine that DCP versions of far-from-resonance backscatter SEROA are guaranteed to have vanishing  $\alpha\alpha$  differences regardless of molecular position, thus eliminating the need to ensemble-average positions around the nanoparticle in order to achieve the chiral selectivity present in ordinary ROA.

DCP<sub>I</sub> and DCP<sub>II</sub> backscatter SEROA intensities were then investigated numerically within the chiroptical model for H<sub>2</sub>S<sub>2</sub> near Ag and Au nanoshells. Excitation profiles throughout the nanoshell dipole and quadrupole plasmon regions were calculated for the separate components, i.e.,  $\alpha\alpha$  for total scattering,  $\alpha G$  and  $\alpha A$  for differential scattering. The enhancement curves depend on polar angle of the molecule around the nanoshell, though not on azimuthal angle. The nanoparticle dipole plasmon  $\alpha\alpha$  peaks were shown to be dominated by molecules near the equator, though the  $\alpha G$  and  $\alpha G$  curves were not, resulting in CID ratios becoming strongly reduced for equatorial molecules and resonant dipole plasmon excitation. Of the two DCP spectroscopies, DCP<sub>I</sub> is generally the more intense except for zero-crossings near the dipole resonance. The initial suggestions we derive for chirally-selective CID measurements are to use DCP<sub>II</sub> with excitation to the red side of the dipole resonance if tuneable excitation is possible, or to use metal nanoshells with the dipole resonance tuned to the blue side of the laser if not.

It is encouraging to find theoretical evidence that there are SEROA configura-

tions for which chiral selectivity can be guaranteed, especially without invoking the positional averaging arising in the earlier SCP analysis. Rotational averaging alone appears sufficient in DCP SEROA for our simple scenario of a spherical substrate and far-from-resonance excitation. This is a far cry from trying to explain all possible SEROA experiments. For example, non-spherical particles will require numerical (e.g., FDTD, FEM, wavelet-based, etc.) methods to evaluate the local fields. For another example, the different possible chemical effect influences in cases of adsorption [106, 138] represent a particularly challenging direction of theoretical research. Nevertheless, there are already facets in non-adsorbed SEROA, where the enhancement is safely regarded as dominantly electromagnetic in origin, that should be of broader interest. For instance, different excitation curves for different molecular multipole contributions will be presumably the rule under any circumstances. There are many questions going forward and a clear need for experiment and theory to work synergistically if SEROA is to become fully realized.

# Appendix A

## OMGC Scaling Wavelet Coefficients

OMGC scaling function coefficients are presented in the following five tables. Each example includes a label, length  $L$ , approximation order  $M$  (or number of vanishing wavelet moments  $\langle \psi | x^p \rangle = 0$  for  $0 \leq p < M$ ),  $N$  the number of power-law moment conditions satisfied ( $m_p = m_1^p$  for  $0 \leq p < N$ ), and the  $c_k$  (for  $0 \leq k < L$ , sum-normalized as  $\sum_{k=0}^{L-1} c_k = 2$ ).

Table A.1: OMGC scaling function coefficients for omgc6, omgc8a, omgc8b and omgc10.

omgc6	−0.1267071922513235	omgc8b	−0.0179972747154978
$L = 6$	0.4250386358717650	$L = 8$	−0.0410910493243252
$M = 2$	1.2004304844748366	$M = 3$	0.4404198422926519
$N = 4$	0.5969388282286596	$N = 5$	1.1403828931699334
	−0.0737232922235132		0.6845155936627885
	−0.0219774641004247		−0.1461291842652923
			−0.1069381612399426
			0.0468373404196841
omgc8a	−0.0790557024471886		
$L = 8$	0.2542062563350704		
$M = 3$	1.0646778132118806	omgc10	0.0314485265162963
$N = 5$	0.8800045022739341	$L = 10$	−0.1060796177056843
	−0.0119633882645343	$M = 3$	−0.0325587040649865
	−0.1424026427354184	$N = 6$	0.8211683456199017
	0.0263412774998423		1.1002235346037514
	0.0081918841264139		0.3004567690524328
			−0.1060740267348034
			−0.0176090677989084
			0.0069606696797422
			0.0020635708322582

Table A.2: OMGC scaling function coefficients for omgc12a, omgc12b, omgc14a and omgc14b.

omgc12a	0.0180436433850061	omgc14a	-0.0090209975165807
$L = 12$	-0.0613875795683868	$L = 14$	0.0349943676381062
$M = 4$	-0.0505205917410534	$M = 4$	0.0007325013914531
$N = 7$	0.6241186611593869	$N = 8$	-0.1892413775872553
	1.1475919052584931		0.2263966531021818
	0.5065051290105076		1.0585433907998221
	-0.1522037216393126		0.8774463152138786
	-0.0743289489636378		0.0979430516749883
	0.0397713411431901		-0.1069337413903037
	0.0058812277010004		-0.0038145186654976
	-0.0026825764063233		0.0123684945268530
	-0.0007884893388704		0.0018300928687717
			-0.0009892253274822
			-0.0002550067289354
omgc12b	0.0016661083363313	omgc14b	-0.0024596092289627
$L = 12$	0.0048271276547957	$L = 14$	0.0008340675388356
$M = 4$	-0.0194971439489805	$M = 4$	0.0368625417704713
$N = 7$	-0.0706084267301574	$N = 8$	-0.0600073818630544
	0.2521812935470935		-0.1387991605226137
	0.9930851251098970		0.4965973366325058
	0.9443466180730492		1.1453587414933879
	0.0505544891636166		0.6377013958344731
	-0.2178553581199926		-0.0604821523803781
	0.0356574395428477		-0.0809460049764011
	0.0391584821124991		0.0198276859717999
	-0.0135157547409996		0.0067289970809512
			-0.0003080471037046
			-0.0009084102473102

Table A.3: OMGC scaling function coefficients for omgc16a, omgc16b, omgc16c and omgc16d.

omgc16a	-0.0049093731556696	omgc16c	-0.0006048508291197
$L = 16$	0.0194494205362229	$L = 16$	-0.0002273688778362
$M = 5$	0.0059856841705450	$M = 5$	0.0059901297104815
$N = 9$	-0.1350982663245348	$N = 9$	0.0106515756805908
	0.1350207894001678		-0.0601688956253016
	0.9380425968517052		-0.0466027892168970
	1.0061838254719051		0.5215728854975018
	0.1934462308416475		1.1173293123411470
	-0.1775185758000848		0.6553275625555504
	-0.0150663907062538		-0.1336640919277970
	0.0395697990223420		-0.1443252240288719
	-0.0002225852191671		0.0681694822880671
	-0.0047074367117578		0.0226502311513585
	-0.0006457351196574		-0.0168315069287218
	0.0003752876025523		-0.0004418384315989
	0.0000947291400376		0.0011753866414472
omgc16b	-0.0013870786672766	omgc16d	0.0041203398947327
$L = 16$	0.0004980198348624	$L = 16$	-0.0145011578842371
$M = 5$	0.0227207905150119	$M = 5$	-0.0082407012577329
$N = 9$	-0.0349408265924134	$N = 9$	0.0866403779890248
	-0.1140018378378629		-0.0449647972134521
	0.3554231401608733		-0.2502810698605614
	1.0791696994328714		0.3198195966829908
	0.8154972507041668		1.0775553285354580
	-0.0109161539669051		0.8030321487579269
	-0.1645804550635392		0.1101349149717154
	0.0327363640804665		-0.0830708114962218
	0.0306260624340690		-0.0113803060906263
	-0.0084596779967788		0.0100230124045640
	-0.0029072533633644		0.0020361477499290
	0.0001378944404735		-0.0007187877728078
	0.0003840618853456		-0.0002042354107023

Table A.4: OMGC scaling function coefficients for omgc18a and omgc18b.

omgc18a	0.0027617480482175	omgc18b	0.0002504347240344
$L = 18$	-0.0123388815593429	$L = 18$	0.0003670032152987
$M = 5$	0.0030939750689916	$M = 5$	-0.0044109962751403
$N = 10$	0.0672866292339156	$N = 10$	-0.0027001112813621
	-0.0917776397413749		0.0383115887101317
	-0.1644205086528380		-0.0171555204082014
	0.5384046523784675		-0.1680950778701714
	1.1275055849772890		0.2308708082830127
	0.6242289607917478		1.0266328245371521
	-0.0283914494671951		0.9109391173316176
	-0.0889311295522289		0.1054563146289063
	0.0108090217966271		-0.1452803949135425
	0.0141261534305589		0.0048121256907447
	-0.0002568651396724		0.0246486042865274
	-0.0020652453028664		-0.0024274719594167
	-0.0002290129925151		-0.0020509906439804
	0.0001585248784869		-0.0005297421862410
	0.0000354818037315		0.0003614841306300



Table A.5: OMGC scaling function coefficients for omgc20a, omgc20b, omgc20c and omgc20d.

omgc20a	0.0014509175634548	omgc20c	0.0002203359787782
$L = 20$	-0.0066557137626640	$L = 20$	-0.0003013812961665
$M = 6$	0.0005178406154773	$M = 6$	-0.0017248655335432
$N = 11$	0.0443946481798473	$N = 11$	-0.0005268426443553
	-0.0566577998996883		0.0169829483402868
	-0.1410395183746280		0.0014010656052483
	0.4244450815186285		-0.1083250392487882
	1.1015778746824811		0.0672786864482410
	0.7474513786419231		0.7899171827820997
	-0.0169206780169819		1.0829206344022115
	-0.1437364728884338		0.3621038527800952
	0.0245043526118266		-0.2122339071586538
	0.0309397254025597		-0.0648802512813744
	-0.0061664408531104		0.0776427996868298
	-0.0051266197644233		0.0045214481377770
	0.0002388868302134		-0.0182198826528193
	0.0007743644289805		0.0013519215107991
	0.0000793230617718		0.0021613091659094
	-0.0000584156184784		-0.0001675334661302
	-0.0000127343587559		-0.0001224815564450
omgc20b	0.0001414660467921	omgc20d	-0.0012952610283717
$L = 20$	0.0002002186593607	$L = 20$	0.0053631665006403
$M = 6$	-0.0026643148427842	$M = 6$	0.0013643232351729
$N = 11$	-0.0016837877644878	$N = 11$	-0.0348463058856080
	0.0248656135909571		0.0290908797278427
	-0.0079073946587106		0.0998454593589672
	-0.1294073460375258		-0.1546637717806863
	0.1491855261981898		-0.1803360050348811
	0.9113980461340532		0.5896193143087433
	1.0166786841695044		1.1006048356472609
	0.2198425808768479		0.6048034550111961
	-0.2081355374723435		0.0081541298070290
	-0.0210553988024767		-0.0805129006892617
	0.0615900739471895		0.0006773581471509
	-0.0042694215666178		0.0131920094747653
	-0.0107983875846772		0.0007690847663866
	0.0009203608281837		-0.0017153463784864
	0.0010319920287042		-0.0002600520344494
	0.0002284137725706		0.0001172981190857
	-0.0001613875227294		0.0000283287275036

## Bibliography

- [1] I. Daubechies, “Orthonormal bases of compactly-supported wavelets,” *Commun. Pure Appl. Math.*, vol. 41, no. 7, pp. 909–996, 1988.
- [2] I. Daubechies, *Ten Lectures on Wavelets*. SIAM, 1992.
- [3] C. Burrus and R. A. Gopinath, *Introduction to Wavelets and Wavelet Transforms: A Primer*. Upper Saddle River, New Jersey: Prentice Hall, 1998.
- [4] S. G. Mallat, “A theory for multiresolution signal decomposition: The wavelet representation,” *IEEE Trans. Pat. Anal. Mach. Int.*, vol. 11, no. 7, pp. 674–693, 1989.
- [5] O. Rioul, “Simple regularity criteria for subdivision schemes,” *SIAM J. Math. Anal.*, vol. 23, no. 6, pp. 1544–1576, 1992.
- [6] I. Daubechies, “Orthonormal bases of compactly-supported wavelets II. Variations on a theme,” *SIAM J. Math. Anal.*, vol. 24, no. 2, pp. 499–519, 1993.
- [7] C. S. Burrus and J. E. Odegard, “Coiflet systems and zero moments,” *IEEE Trans. Sig. Process.*, vol. 46, no. 3, pp. 761–766, 1998.
- [8] R. A. Gopinath and C. S. Burrus, “On the moments of the scaling function  $\psi_0$ ,” *Proc. of the IEEE ISCAS*, vol. 2, pp. 963–966, May 1992.
- [9] G. Pan, M. V. Toupikov, and B. K. Gilbert, “On the use of coifman intervallic wavelets in the method of moments for fast construction of wavelet sparsified matrices,” *IEEE Trans. on Antennas and Prop.*, vol. 47, pp. 1189–1200, July 1999.
- [10] G. Pan, K. Wang, and B. K. Gilbert, “Coifman wavelets in 3d scattering from very rough surfaces,” *IEEE Trans. on Antennas and Prop. Society Int. Symposium*, vol. 3, pp. 400–403, June 2003.
- [11] Y. Tretiakov, G. Lei, G. Pan, and B. Gilbert, “Numerical study of random surface scattering using coifman wavelets,” *IEE Proc.-Microw. Antennas and Propag.*, vol. 151, pp. 331–337, Aug 2004.
- [12] G. Pan, J.-Y. Lin, and G. Cheng, “Wavelet based deconvolution algorithm for time-domain near-field isar imaging,” *IEEE Trans. on Antennas and Prop.*, vol. 55, pp. 2013–2021, July 2007.
- [13] B. R. Johnson, J. P. Modisette, P. J. Nordlander, and J. L. Kinsey, “Quadrature integration for orthogonal wavelet systems,” *J. Chem. Phys.*, vol. 110, no. 17, pp. 8309–8317, 1999.

- [14] R. Glowinski, W. M. Lawton, M. Ravachol, and E. Tenenbaum, "Wavelet solution of linear and nonlinear elliptic, parabolic and hyperbolic problems in one dimension," in *Proceedings of the Ninth International Conference on Computing Methods in Applied Sciences and Engineering*, (Philadelphia), pp. 55–120, SIAM, 1990.
- [15] W. Lawton, W. Morrell, E. Tenenbaum, and J. Weiss, "The wavelet-Galerkin method for partial differential equations," Tech. Rep. AD901220, Aware, Inc., 1990.
- [16] D. Wei and A. C. Bovik, "Sampling approximation of smooth functions via Generalized Coiflets," *IEEE Trans. Sig. Process.*, vol. 46, no. 4, pp. 1133–1138, 1998.
- [17] D. Wei and A. C. Bovik, "Generalized Coiflets with nonzero-centered vanishing moments," *IEEE Trans. Circ. Systems II*, vol. 45, no. 8, pp. 988–1001, 1998.
- [18] L. Monzón, G. Beylkin, and W. Hereman, "Compactly supported wavelets based on almost interpolating and nearly linear phase filters (Coiflets)," *Appl. Comp. Harm. Anal.*, vol. 7, no. 8, pp. 184–210, 1999.
- [19] T. A. Arias, "Multiresolution analysis of electronic structure: semicardinal and wavelet bases," *Rev. Mod. Phys.*, vol. 71, no. 1, pp. 267–311, 1999.
- [20] C. J. Tymczak. Private communication., 2006.
- [21] J. Tian, R. O. Wells Jr., J. E. Odegard, and C. S. Burrus, *Coifman Wavelet Systems: Approximation, Smoothness, and Computational Algorithms*, pp. 831–840. Wiley, 1997.
- [22] H. L. Resnikoff and R. O. Wells Jr., *Wavelet Analysis: The Scalable Structure of Information*. New York: Springer-Verlag, 1998.
- [23] A. I. Neelov and S. Goedecker, "An efficient numerical quadrature for the calculation of the potential energy of wavefunctions expressed in the Daubechies wavelet basis," *J. Comp. Phys.*, vol. 217, pp. 312–339, 2006.
- [24] G. Beylkin, "On the representation of operators in bases of compactly supported wavelets," *SIAM J. Num. Anal.*, vol. 6, no. 6, pp. 1716–1740, 1992.
- [25] L. Jameson, "On the wavelet based differentiation matrix," *SIAM J. Sci. Comput.*, vol. 8, no. 3, pp. 267–305, 1993.
- [26] L. Jameson, "The differentiation matrix for Daubechies-based wavelets on an interval," *SIAM J. Sci. Comput.*, vol. 17, no. 2, pp. 498–516, 1996.
- [27] G. Beylkin, "On the representation of operators in bases of compactly supported wavelets," *SIAM J. Numer. Anal.*, vol. 6, pp. 1716–1740, December 1992.

- [28] P. Maragakis, J. Soler, and E. Kaxiras, “Variational finite-difference representation of the kinetic energy operator,” *Phys. Rev. B*, vol. 64, no. 4, p. 193101, 2001.
- [29] C.-K. Skylaris, O. Diéguez, P. D. Haynes, and M. C. Payne, “Comparison of variational real-space representations of the kinetic energy operator,” *Phys. Rev. B*, vol. 66, no. 4, p. 073103, 2002.
- [30] C. Lanczos, “An iteration method for the solution of the eigenvalue problem of linear differential and integral operators,” *J. Res. Nat. Bur. Stds.*, vol. 45, no. 4, pp. 255–282, 1950.
- [31] J. K. Cullum and R. A. Willoughby, *Lanczos Algorithms for Large Symmetric Eigenvalue Computations*, vol. I: Theory. Boston: Birkhäuser, 1985.
- [32] N. Sato and S. Iwata, “Numerical methods for large eigenvalue problems,” *J. Chem. Phys.*, vol. 89, no. 5, pp. 2932–2937, 1988.
- [33] D. Calvetti, L. Reichel, and D. C. Sorensen, “An implicitly restarted Lanczos method for large symmetric eigenvalue problems,” *Elec. Trans. Num. Anal.*, vol. 2, pp. 1–21, 1994.
- [34] C. Lanczos, “An iteration method for the solution of the eigenvalue problem of linear differential and integral operators,” *J. Res. Natl. Bur. Stand.*, vol. 45, no. 4, pp. 255–282, 1950.
- [35] D. C. Sorensen, “Implicit application of polynomial filters in a k-step Arnoldi method,” *SIAM J. Mat. Anal. Appl.*, vol. 13, no. 1, pp. 357–385, 1992.
- [36] R. B. Lehoucq, D. C. Sorensen, and C. Yang, *ARPACK Users’ Guide: Solution of Large-Scale Eigenvalue Problems with Implicitly Restarted Arnoldi Methods.*, 1998.
- [37] D. C. Sorensen, “Numerical methods for large eigenvalue problems,” *Acta Numerica*, vol. 11, pp. 519–584, 2002.
- [38] A. Hosseini, A. Nieuwoudt, and Y. Massoud, “Efficient simulation of subwavelength plasmonic waveguides using implicitly restarted Arnoldi,” *Optics Express*, vol. 14, pp. 7291–7298, Aug 2006.
- [39] D. T. Colbert and W. H. Miller, “A novel discrete variable representation for quantum mechanical reactive scattering via the S-matrix Kohn method,” *J. Chem. Phys.*, vol. 96, pp. 1982–1991, February 1992.
- [40] G. W. Wei, S. C. Althorpe, D. J. Kouri, and D. K. Hoffman, “An application of distributed approximating functional-wavelets to reactive scattering,” *J. Chem. Phys.*, vol. 108, no. 17, pp. 7065–7069, 1998.

- [41] V. Szalay and S. C. Smith, "Application of contracted distributed approximating functions to solving vibrational eigenvalue problems," *J. Chem. Phys.*, vol. 110, no. 1, pp. 72–79, 1999.
- [42] D. Xu, J. Stare, and A. L. Cooksy, "Solving the vibrational Schrödinger equation on an arbitrary multidimensional potential energy surface by the finite element method," *Comput. Phys. Comm.*, vol. 180, pp. 2079–2094, 2009.
- [43] B. Chmura, Z. Lan, M. F. Rode, and A. L. Sobolewski, "Photochemistry of the water dimer: Time-dependent quantum wave-packet description of the dynamics at the  $S_1$ - $S_0$  conical intersection," *J. Chem. Phys.*, vol. 131, no. 13, p. 134307, 2009.
- [44] Z. Bačić and J. C. Light, "Highly-excited vibrational levels of "floppy" triatomic molecules: A discrete variable representation-distributed Gaussian basis approach," *J. Chem. Phys.*, vol. 85, no. 8, pp. 4594–4604, 1986.
- [45] G. C. Groenenboom and D. T. Colbert, "Combining the discrete variable representation with the S-matrix Kohn method for quantum reactive scattering," *J. Chem. Phys.*, vol. 99, no. 12, pp. 9681–9696, 1993.
- [46] D. Imre, J. L. Kinsey, A. Sinha, and J. Krenos, "Chemical dynamics studied by emission spectroscopy of dissociating molecules," *J. Phys. Chem.*, vol. 88, no. 18, pp. 3956–3964, 1984.
- [47] B. R. Johnson, C. Kittrell, P. B. Kelley, and J. L. Kinsey, "Resonance Raman spectroscopy of dissociative polyatomic molecules," *J. Phys. Chem.*, vol. 100, no. 19, pp. 7743–7764, 1996.
- [48] J. L. Mackey, B. R. Johnson, C. Kittrell, L. D. Le, and J. L. Kinsey, "Resonance Raman spectroscopy in the dissociative  $a$  band of nitrosyl chloride," *J. Chem. Phys.*, vol. 114, pp. 6631–6640, April 2001.
- [49] T. Yamashita and S. Kato, "Regularity in highly excited vibrational dynamics of NOCl ( $X_1A'$ ): Quantum mechanical calculations on a new potential energy surface," *J. Chem. Phys.*, vol. 119, p. 4251, 2003.
- [50] R. Acevedo, R. Lombardini, M. A. Turner, J. L. Kinsey, and B. R. Johnson, "Quantum and electromagnetic propagation with the conjugate symmetric Lanczos method," *J. Chem. Phys.*, vol. 128, p. 064103, 2008.
- [51] C. Leforestier, R. H. Bisseling, C. Cerjan, M. D. Feit, R. Friesner, A. Guldborg, A. Hammerich, G. Jolicard, W. Karrlein, H.-D. Meyer, N. Lipkin, O. Roncero, and R. Kosloff, "A comparison of different propagation schemes for the time dependent Schrödinger equation," *J. Comput. Phys.*, vol. 94, pp. 59–80, May 1991.
- [52] R. Kosloff, "Propagation methods for quantum molecular dynamics," *Annu. Rev. Phys. Chem.*, vol. 45, pp. 145–178, 1994.

- [53] S. K. Gray and J. M. Verosky, "Classical Hamiltonian structures in wave packet dynamics," *J. Chem. Phys.*, vol. 100, pp. 5011–5022, April 1994.
- [54] M. D. Feit, J. A. Fleck Jr., and A. Steiger, "Solution of the Schrödinger equation by a spectral method," *J. Comput. Phys.*, vol. 47, pp. 412–433, 1982.
- [55] T. J. Park and J. C. Light, "Unitary quantum time evolution by iterative Lanczos reduction," *J. Chem. Phys.*, vol. 85, pp. 5870–5876, November 1986.
- [56] H. Tal-Ezer, R. Kosloff, and C. Cerjan, "Low-order polynomial approximation of propagators for the time-dependent Schrödinger equation," *J. Comput. Phys.*, vol. 100, pp. 179–187, 1992.
- [57] G. Yao and R. E. Wyatt, "A Krylov-subspace Chebyshev method and its application to pulsed laser-molecule interaction," *Chem. Phys. Lett.*, vol. 239, pp. 207–216, March 1995.
- [58] H. Tal-Ezer and R. Kosloff, "An accurate and efficient scheme for propagating the time-dependent Schrödinger equation," *J. Chem. Phys.*, vol. 81, no. 9, pp. 3967–3971, 1984.
- [59] D. O. Harris, G. G. Engerholm, and W. D. Gwinn, "Calculation of matrix elements for one-dimensional quantum-mechanical problems and the application to anharmonic oscillators," *J. Chem. Phys.*, vol. 43, pp. 1515–1517, September 1965.
- [60] A. S. Dickinson and P. R. Certain, "Calculation of matrix elements for one-dimensional quantum-mechanical problems," *J. Chem. Phys.*, vol. 49, pp. 4209–4211, November 1968.
- [61] J. V. Lill, G. A. Parker, and J. C. Light, "Discrete variable representations and sudden models in quantum scattering theory," *Chem. Phys. Lett.*, vol. 89, no. 6, pp. 483–489, 1982.
- [62] J. C. Light and T. Carrington Jr., "Discrete-variable representations and their utilization," *Adv. Chem. Phys.*, vol. 114, pp. 263–310, 2000.
- [63] G. Strang and G. J. Fix, *An Analysis of the Finite Element Method*. Prentice-Hall, 1973.
- [64] H. Wang, R. Acevedo, H. Mollé, J. L. Mackey, J. L. Kinsey, and B. R. Johnson, "Multiscale quantum propagation using compact-support wavelets in space and time," *J. Chem. Phys.*, vol. 121, pp. 7647–7657, October 2004.
- [65] D. K. Sparks and B. R. Johnson, "Two-dimensional quantum propagation using wavelets in space and time," *J. Chem. Phys.*, vol. 125, p. 114104, 2006.
- [66] J. S. Kole, M. T. Figge, and H. De Raedt, "Unconditionally stable algorithms to solve the time-dependent Maxwell equations," *Phys. Rev. E*, vol. 64, November 2001.

- [67] H. De Raedt, K. Michielsen, J. S. Kole, and M. T. Figge, “One-step finite-difference time-domain algorithm to solve the Maxwell equations,” *Phys. Rev. E*, vol. 67, May 2003.
- [68] H. De Raedt, K. Michielsen, J. S. Kole, and M. T. Figge, “Solving the Maxwell equations by the Cheybshev method: A one-step finite-difference time-domain algorithm,” *IEEE Trans. on Antennas and Prop.*, vol. 51, pp. 3155–3160, November 2003.
- [69] A. G. Borisov and S. V. Shabanov, “Lanczos pseudospectral method for initial-value problems in electrodynamics and its applications to ionic crystal gratings,” *J. Comput. Phys.*, vol. 209, pp. 643–664, 2005.
- [70] A. G. Borisov and S. V. Shabanov, “Wave packet propagation by the faber polynomial approximation in electrodynamics of passive media,” *J. Comput. Phys.*, vol. 216, pp. 391–402, 2006.
- [71] A. Taflove and S. C. Hagness, *Computational Electrodynamics: The Finite-Difference Time-Domain Method*. Artech House, 3rd ed., 2005.
- [72] C. Oubre and P. Nordlander, “Finite-difference time-domain studies of the optical properties of nanoshell dimers,” *J. Phys. Chem. B*, vol. 109, pp. 10042–10051, 2005.
- [73] P. B. Johnson and R. W. Christy, “Optical constants of the noble metals,” *Phys. Rev. B*, vol. 6, pp. 4370–4379, 1972.
- [74] C. Cerjan and R. Kosloff, “Efficient variable time-stepping scheme for intense field-atom interactions,” *Phys. Rev. A*, vol. 47, pp. 1852–1860, March 1993.
- [75] N. Mohankumar and S. M. Auerbach, “On time-step bounds in unitary quantum evolution using the Lanczos method,” *Comput. Phys. Comm.*, vol. 175, pp. 473–481, 2006.
- [76] S. K. Gray and D. E. Manolopoulos, “Symplectic integrators tailored to the time-dependent Schrödinger equation,” *J. Chem. Phys.*, vol. 104, pp. 7099–7112, May 1996.
- [77] R. J. Hawkins, R. R. McLeod, J. S. Kallman, R. P. Ratowsky, M. D. Feit, and J. A. Fleck Jr., “New directions in photonics simulation: Lanczos recursion and finite-difference time-domain,” Tech. Rep. 221743, Lawrence Livermore National Laboratory, June 1992.
- [78] Y. Huang, D. J. Kouri, and D. K. Hoffman, “General, energy-separable faber polynomial representation of operator functions: Theory and application in quantum scattering,” *J. Chem. Phys.*, vol. 101, no. 12, pp. 10493–10506, 1994.

- [79] R. W. Freund, "The look-ahead Lanczos process for nonsymmetric matrices and its applications," in *Proceedings of the Cornelius Lanczos International Centenary Conference* (J. D. Brown, M. T. Chu, D. C. Ellison, and R. J. Plemmons, eds.), (Philadelphia), pp. 33–47, SIAM, 1994.
- [80] A. G. Borisov and S. V. Shabanov, "Applications of the wave packet method to resonant transmission and reflection gratings," *J. Comput. Phys.*, vol. 199, pp. 742–762, 2004.
- [81] M.-S. Min, T.-W. Lee, P. F. Fischer, and S. K. Gray, "Fourier spectral simulations and gegenbauer reconstructions for electromagnetic waves in the presence of a metal nanoparticle," *J. Comput. Phys.*, vol. 213, pp. 730–747, 2006.
- [82] M. Krumpholz and L. P. B. Katehi, "MRTD: New time domain schemes based on multiresolution analysis," *IEEE Trans. Microwave Theory Tech.*, vol. 44, pp. 555–571, April 1996.
- [83] M. Fujii and W. J. R. Hoefer, "Interpolating wavelet collocation method of time dependent maxwell's equations: characterization of electrically large optical waveguide discontinuities," *J. Comput. Phys.*, vol. 186, pp. 666–689, 2003.
- [84] R. Acevedo, R. Lombardini, N. J. Halas, and B. R. Johnson, "Plasmonic enhancement of Raman optical activity in molecules near metal nanoshells," *J. Phys. Chem. A*, vol. 113, no. 47, pp. 13173–13183, 2009.
- [85] R. Lombardini, R. Acevedo, N. J. Halas, and B. R. Johnson, "Plasmonic enhancement of Raman optical activity in molecules near metal nanoshells: Theoretical comparison of circular polarization methods," *J. Phys. Chem. C*, to appear, 2010.
- [86] M. Fleischmann, P. Hendra, and A. McMillan, "Raman spectra of pyridine adsorbed at a silver electrode," *Chem. Phys. Lett.*, vol. 26, pp. 163–166, 1974.
- [87] D. L. Jeanmarie and R. P. Van Duyne, "Surface Raman spectroelectrochemistry: Part I. heterocyclic, aromatic, and aliphatic amines adsorbed on the anodized silver electrode," *J. ElectroAnalytical Chem.*, vol. 84, pp. 1–20, 1977.
- [88] M. Moskovits, "Surface-enhanced spectroscopy," *Rev. Mod. Phys.*, vol. 57, no. 3, pp. 783–826, 1985.
- [89] A. Otto, I. Mrozek, H. Grabhorn, and W. Akemann, "Surface-enhanced Raman scattering," *J. Phys.*, vol. 4, pp. 1143–1212, 1992.
- [90] C. R. Yonzon, D. A. Stuart, X. Zhang, A. D. McFarland, C. L. Haynes, and R. P. Van Duyne, "Towards advanced chemical and biological nanosensors-An overview," *Talanta*, vol. 67, pp. 438–448, 2005.
- [91] S. Lal, S. Link, and N. J. Halas, "Nano-optics from sensing to waveguiding," *Nature Photonics*, vol. 1, no. 11, pp. 641–648, 2007.



- [92] L. D. Barron and A. D. Buckingham, "Rayleigh and Raman scattering from optically active molecules," *Mol. Phys.*, vol. 20, no. 6, pp. 1111–1119, 1971.
- [93] L. D. Barron, F. Zhu, L. Hecht, G. E. Tranter, and N. W. Isaacs, "Raman optical activity: An incisive probe of molecular chirality and biomolecular structure," *J. Mol. Struct.*, vol. 834–836, pp. 7–16, 2007.
- [94] S. Efrima, "The effect of large electric field gradients on the Raman optical activity of molecules adsorbed on metal surfaces," *Chem. Phys. Lett.*, vol. 102, no. 1, pp. 79–82, 1983.
- [95] S. Efrima, "Raman optical activity of molecules adsorbed on metal surfaces: Theory," *J. Chem. Phys.*, vol. 83, no. 3, pp. 1356–1362, 1985.
- [96] L. Hecht and L. D. Barron, "Rayleigh and Raman optical activity from chiral surfaces," *Chem. Phys. Lett.*, vol. 225, pp. 525–530, 1994.
- [97] L. Hecht and L. D. Barron, "Rayleigh and Raman optical activity from chiral surfaces and interfaces," *J. Mol. Struct.*, vol. 348, pp. 217–220, 1995.
- [98] H. Kneipp, J. Kneipp, and K. Kneipp, "Surface-enhanced Raman optical activity on adenine in silver colloidal solution," *Anal. Chem.*, vol. 78, no. 4, pp. 1363–1366, 2006.
- [99] S. Abdali, "Observation of SERS effect in Raman optical activity, a new tool for chiral vibrational spectroscopy," *J. Raman Spectrosc.*, vol. 37, pp. 1341–1345, 2006.
- [100] B. G. Janesko and G. E. Scuseria, "Surface enhanced Raman optical activity of molecules on orientationally averaged substrates: Theory of electromagnetic effects," *J. Chem. Phys.*, vol. 125, no. 12, p. 124704, 2006.
- [101] P. G. Etchegoin, C. Galloway, and E. C. Le Ru, "Polarization-dependent effects in surface-enhanced Raman scattering (SERS)," *Phys. Chem. Chem. Phys.*, vol. 8, pp. 2624–2628, 2006.
- [102] S. Abdali, C. Johannessen, J. Nygaard, and T. Nørbygaard, "Resonance surface enhanced Raman optical activity of myoglobin as a result of optimized resonance surface enhanced Raman scattering conditions," *J. Phys.: Condens. Matter*, vol. 19, p. 285205:1, 2007.
- [103] C. Johannessen and S. Abdali, "Surface-enhanced Raman optical activity as an ultra sensitive tool for ligand binding analysis," *Spectroscopy*, vol. 21, pp. 143–149, 2007.
- [104] P. Bouř, "Matrix formulation of the surface-enhanced Raman optical activity theory," *J. Chem. Phys.*, vol. 126, no. 13, p. 136101, 2007.

- [105] S. Abdali and E. W. Blanch, “Surface enhanced Raman optical activity (SEROA),” *Chem. Soc. Rev.*, vol. 37, pp. 980–992, 2008.
- [106] L. Jensen, “Surface-enhanced vibrational Raman optical activity: A time-dependent density functional theory approach,” *J. Phys. Chem. A*, vol. 113, pp. 4437–4444, 2010.
- [107] N. A. Brazhe, A. R. Brazhe, O. V. Sosnovtseva, and S. Abdali, “Novel chiroptical analysis of hemoglobin by surface enhanced resonance Raman optical activity spectroscopy,” *Chirality*, vol. 21, no. 1E, pp. E307–E312, 2010.
- [108] S. J. Oldenburg, R. D. Averitt, S. L. Westcott, and N. J. Halas, “Surface enhanced Raman scattering in the near infrared using metal nanoshell substrates,” *Chem. Phys. Lett.*, vol. 288, p. 247, 1998.
- [109] M. Kerker, D. Wang, and H. Chew, “Surface enhanced Raman scattering (SERS) by molecules absorbed at spherical particles,” *Appl. Optics*, vol. 19, pp. 4159–4174, 1980.
- [110] J. Trost and K. Hornberger, “The twisted arc model for chiral molecules,” *Chem. Phys.*, vol. 355, pp. 115–123, 2007.
- [111] L. D. Barron, *Molecular Light Scattering and Optical Activity*. New York?: Cambridge University Press, 2nd ed., 2004.
- [112] A. D. Buckingham, “Permanent and induced molecular moments and long range intermolecular forces,” *Adv. Chem. Phys.*, vol. 12, pp. 107–141, 1967.
- [113] J. D. Jackson, *Classical Electrodynamics*. Hoboken: John Wiley & Sons, 3rd ed., 1999.
- [114] S. Luber, C. Herrmann, and M. Reiher, “Relevance of the electric-dipole–electric-quadrupole contribution to Raman optical activity spectra,” *J. Phys. Chem. B*, vol. 112, no. 7, pp. 2218–2232, 2008.
- [115] D. Sarkar and N. J. Halas, “General vector basis function solution of Maxwell’s equations,” *Phys. Rev. E*, vol. 56, no. 1, pp. 1102–1112, 1997.
- [116] J. A. Stratton, *Electromagnetic Theory*. Hoboken: John Wiley & Sons, 2007.
- [117] H. C. van de Hulst, *Light scattering by small particles*. New York: Dover Publications, 1957.
- [118] G. Mie, “Beiträge zur Optik trüber Medien, speziell kolloidaler Matallösungen,” *Annal. der Physik*, vol. 25, pp. 377–445, 1908.
- [119] A. L. Aden and M. Kerker, “Scattering of electromagnetic waves from two concentric spheres,” *J. Appl. Phys.*, vol. 22, pp. 1242–1246, 1951.

- [120] A. Ben-Menahem, “Green’s tensors and associated potentials for electromagnetic waves in inhomogeneous material media,” *Proc. R. Soc. Lond. A*, vol. 426, pp. 79–106, 1989.
- [121] L. Novotny and B. Hecht, *Principles of Nano-Optics*. New York: Cambridge University Press, 2006.
- [122] L. D. Barron, L. Hecht, I. H. McColl, and E. W. Blanch, “Raman optical activity comes of age,” *Mol. Phys.*, vol. 20, no. 8, pp. 731–744, 2004.
- [123] L. D. Barron and J. R. Escribano, “Stokes-antistokes asymmetry in natural Raman optical activity,” *Chem. Phys.*, vol. 98, pp. 437–446, 1985.
- [124] L. Hecht and L. A. Nafie, “Theory of natural Raman optical activity part I. complete circular polarization formalism,” *Mol. Phys.*, vol. 72, no. 2, pp. 441–469, 1991.
- [125] G. Placzek, *Handbuch der Radiologie*, vol. 6, ch. Rayleigh-Streuung und Raman-Effekt, pp. 205–374. Leipzig: Akademische Verlagsgesellschaft, 1934.
- [126] L. A. Nafie and T. B. Freedman, “Dual circular polarization Raman optical activity,” *Chem. Phys. Lett.*, vol. 154, no. 3, pp. 260–266, 1989.
- [127] D. Che, L. Hecht, and L. A. Nafie, “Dual and incident circular polarization Raman optical activity backscattering of (–)-trans-pinane,” *Chem. Phys. Lett.*, vol. 180, no. 3, pp. 182–190, 1991.
- [128] L. Hecht and L. D. Barron, “An analysis of modulation experiments for Raman optical activity,” *Appl. Spectrosc.*, vol. 44, no. 3, pp. 483–491, 1990.
- [129] D. A. Long, *Raman Spectroscopy*. Maidenhead, G.B: McGraw-Hill, 1977.
- [130] M. Pecul and K. Ruud, “Ab initio calculation of vibrational Raman optical activity,” *Int. J. Quant. Chem.*, vol. 104, pp. 816–829, 2005.
- [131] G. Zuber, M. Goldsmith, D. N. Beratan, and P. Wipf, “Towards Raman optical activity calculations of large molecules,” *ChemPhysChem*, vol. 6, pp. 595–597, 2005.
- [132] L. Jensen, J. Autschbach, M. Krykunov, and G. C. Schatz, “Resonance vibrational Raman optical activity: A time-dependent density functional theory approach,” *J. Chem. Phys.*, vol. 127, p. 134101, 2007.
- [133] R. L. Redington, “The infrared spectrum and barriers hindering internal rotation in  $\text{H}_2\text{S}_2$ ,  $\text{CF}_3\text{SH}$ , and  $\text{CF}_3\text{SD}$ ,” *J. Mol. Spec.*, vol. 9, pp. 469–476, 1962.
- [134] C. J. Marsden and B. J. Smith, “Harmonic force fields, molecular structure, torsional potential, and possible isomerism of  $\text{H}_2\text{S}_2$ ,” *J. Phys. Chem.*, vol. 92, pp. 347–353, 1988.

- [135] P. B. Johnson and R. W. Christy, “Optical constants of the noble metals,” *Phys. Rev. B*, vol. 6, no. 12, pp. 4370–4379, 1972.
- [136] L. A. Nafie, “Theory of resonance Raman optical activity: the single electronic state limit,” *Chem. Phys.*, vol. 205, pp. 309–322, 1996.
- [137] L. A. Nafie, “Infrared and Raman vibrational optical activity: Theoretical and experimental aspects,” *Annu. Rev. Phys. Chem.*, vol. 48, pp. 357–386, 1997.
- [138] B. G. Janesko and G. E. Scuseria, “Molecule-surface orientational averaging in surface enhanced Raman optical activity spectroscopy,” *J. Phys. Chem. C*, vol. 113, pp. 9445–9449, 2009.
- [139] J. B. Jackson and N. J. Halas, “Surface-enhanced Raman scattering on tunable plasmonic nanoparticle substrates,” *Proc. Natl. Acad. Sci. (US)*, vol. 101, pp. 17930–17935, December 2004.